BRNO UNIVERSITY OF TECHNOLOGY
VYSOKÉ UČENÍ TECHNICKÉ V BRNĚ

CENTRAL EUROPEAN INSTITUTE OF TECHNOLOGY BUT
STŘEDOEVROPSKÝ TECHNOLOGICKÝ INSTITUT VUT

DEFORMATION AND STRESS FIELDS AT THE FRONT OF SHEAR CRACKS WITH COMPLICATED GEOMETRY
POLE NAPĚTÍ A DEFORMACE V OKOLÍ TRHLIN S KOMPLIKOVANOU GEOMETRIÍ ČELA ZATÍŽENÝCH VE SMYKOVÝCH ZÁTĚŽNÝCH MÓDECH

DOCTORAL THESIS
DIZERTAČNÍ PRÁCE

AUTHOR   Ing. Stanislav Žák
AUTOR PRÁCE

SUPERVISOR   doc. Ing. Jana Horníková, Ph.D.
ŠKOLITEL

BRNO 2018

Abstract

This thesis summarizes the extend of research on the shear-modes loaded cracks done in the period of four years of doctoral studies of Ing. Stanislav Žák (Central European Institute of Technology, Brno University of Technology). The actual research aims to improve the scientific view on advanced fracture mechanics, specifically for the shear loading of cracks combined with cases when the geometry of the crack flanks and front doesn't match with widely used and standardized models. This means proposal of new modelling approaches of geometrically complicated cracks and description of changes in the local stress intensity factors along such cracks.

Initial part of the text presents a review of current approaches in the fracture mechanics and numerical methods used in further research. This part emphasizes theoretical methods in general fracture mechanics and also specific shear modes loading, particularly use of the two types of specimens – a special specimen dedicated to mode II loading (compact-tension-shear specimen) with a possibility of mixed-mode I+II loading, and widely used cylindrical specimen with circumferential notch and crack which is able to comprehend mode II and III loading.

The second, more extensive part of this thesis concentrates on actual evaluation of conditions along the real-like (tortuous) crack fronts for two types of specimens under the remote shear mode loading. Theoretical solution of fracture parameters for both mentioned specimens is compared to the experimental results obtained in the frame of the follow-up projects.

The cylindrical specimen is reviewed from two points of view. The first one is solely about the numerical methods and the simplification of complex numerical models. In the second one, the influence of small asperities along the crack front on local k_2 inducement for specimens under the remote mode III loading is observed. The results are directly connected to the experimental measurement of mode III fatigue thresholds values for metallic materials where the local mode II advances of crack front are quantified. On fractures in compact-tension-shear specimen various configurations of crack front and flanks tortuosity are investigated. The global decrease of K_{II} with increasing crack tortuosity is observed and used for correction of mode II fatigue threshold values of metallic materials. Furthermore, the conditions along one particular asperity are investigated.

The results confirm that the shear loaded cracks (which were not described sufficiently so far) are affected by the crack front and flanks microstructure. Therefore, this work extends the knowledge on roughness-induced shielding of shear loaded cracks.

Keywords

compact-tension-shear specimen; crack tortuosity; cylindrical specimen; finite element modeling; linear-elastic fracture mechanics; shear mode loading; stress intensity factors

Abstrakt

Tato závěrečná práce je shrnutím výzkumu smykově zatěžovaných trhlin, který proběhl v průběhu čtyř let doktorského studia jejich autora Ing. Stanislava Žáka (Středoevropský technologický institut, Vysoké učení technické v Brně). Předložená práce je zaměřena na prohloubení znalostí v oblasti pokročilé lomové mechaniky, konkrétně pro smykové zatěžování trhlin kombinované s případy geometrických odchylek trhlin od běžně používaných modelů. To mimo jiné znamená návrh nových přístupů a modelů a popis součinitelů intenzity napětí pro geometricky komplikované trhliny.

První část práce je věnována shrnutí současných přístupů v lomové mechanice a dále i popisu numerických metod, použitých v dalších výpočtech. Kromě klasických přístupů se tato část textu zabývá i novějším výzkumem zaměřeným na smykové zatěžování trhlin, speciálně pro dva typy zkušebních těles – válcový vzorek s obvodovým vrubem a trhlinou zatížený prostým smykem nebo krutem a CTS těleso umožňující zatížení trhliny v módech I, II a také v jejich kombinaci I+II.

Další část textu je zaměřena na konkrétní výpočty lomových parametrů při použití nových modelů s komplikovaným čelem trhliny. Teoretické řešení lomových parametrů pro oba výše zmíněné modely je porovnáno s experimentálními výsledky, získanými v navazujících projektech.

U modelu válcového vzorku je popsána možnost zjednodušení budoucích modelů těles s podobným typem komplikované trhliny a současně je na něm popsán lokální vliv zubatosti čela trhliny na indukci lokálního zatížení v módu II při globálním zatížení v módu III. Tyto výsledky jsou přímo propojeny s experimentální kvantifikací únavového šíření lomu při zatížení v módu III. CTS těleso je použito k popisu vlivu drsnosti trhliny na součinitele intenzity napětí. Na tomto modelu je pozorován jak globální pokles hodnoty K_{II} při zvyšující se drsnosti trhliny, tak i lokální změny v namáhání trhliny podél jednotlivých nerovností.

Výsledky potvrzují, i pro dosud málo zkoumané smykové zatěžování, že mikrostruktura lomových ploch a čela trhliny má vliv na lomové parametry. Rozšiřují tak současné znalosti v oboru lomové mechaniky popisem geometrického stínění čela trhliny pro zátěžné módy II a III.

Klíčová slova

CTS vzorek; křivolakost trhliny; lineárně-elastická lomová mechanika; MKP modelování; smykové zátěžné módy; součinitele intenzity napětí; válcový vzorek

Bibliographic quotation

ŽÁK, S. *Deformation and Stress Fields at the Front of Shear Cracks with Complicated Geometry.* Brno: Brno University of Technology, Central European Institute of Technology BUT, 2018. 99 p., Supervisor of the dissertation thesis doc. Ing. Jana Horníková, Ph.D.

Bibliografická citace

ŽÁK, S. *Pole napětí a deformace v okolí trhlin s komplikovanou geometrií čela zatížených ve smykových zátěžných módech.* Brno: Vysoké učení technické v Brně, Středoevropský technologický institut VUT, 2018. 99 s. Vedoucí dizertační práce doc. Ing. Jana Horníková, Ph.D.

Statutory declaration

I hereby declare that submitted dissertation thesis is my original work which I have done on my own under the supervision of my supervisor doc. Ing. Jana Horníková, Ph.D. with use of quoted literature and information sources.

Čestné prohlášení

Prohlašuji, že tato disertace je mojí originální prací, kterou jsem samostatně zpracoval pod vedením mé vedoucí doc. Ing. Jany Horníkové, Ph.D. s použitím citované literatury a dalších zdrojů informací.

In Brno, 30. 7. 2018

_____

Ing. Stanislav Žák

Acknowledgement

Table of Contents

1 Introduction

In recent time mankind is using more modern and advanced mechanical instruments and gadgets each day in all kinds of industrial branches. Even the smallest devices used in day-to-day applications by ordinary people are becoming very complex and complicated. This leads (almost) to addiction on the modern technologies because no-one can imagine a day, even an hour without his mobile phone, computer, car, always accessible source of electrical energy, etc. But accidents happen and none of these devices are indestructible which means that time-to-time something disturb the luxury of human life...

To improve the situation two things can be done – either to simplify everything and go "back to roots" without use of any complicated technology or to work on refining the devices to increase their durability and prolong their operating life. The second resort seems to be more useful in our modern society and mankind is working on this approach for decades.

One particular direction in improvement of mechanisms is in term of strengthening the materials and improving the fatigue life of modern materials. Hand to hand with this approach goes the scientific branch of the fracture mechanics.
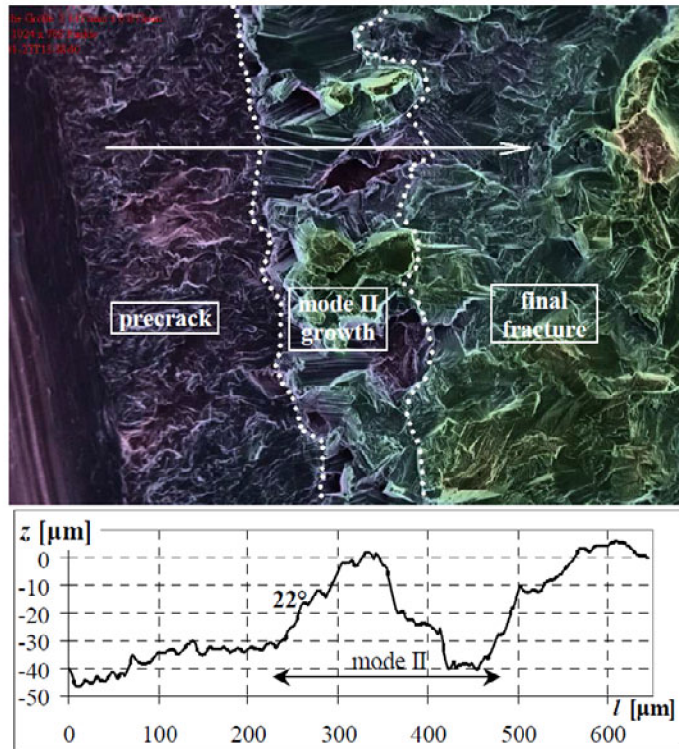

Fig. 1: Example of the rough crack surface (SEM image, Vojtek et al. [1])

As said before, work on improvement of materials reliability has been started a long time ago and the fracture mechanics scientific branch is no exception. Numerous theoretical approaches to describe fracture behavior, fatigue of materials and related

material properties were developed [2] starting with the work of Inglis and Griffith in early 20th century. Their work was broadened by other different approaches [3–5] (e.g. *J*-integral, stress intensity factors (SIFs), crack tip opening displacement (CTOD), etc.) to evaluate the fracture parameters. These approaches were used to create models representing at first some abstract bodies with cracks (2D infinite or semi-infinite planes with central crack) but they were adapted to more real-like specimens and geometries at a very fast pace. These models are now used as a tool to obtain some description of fracture by means of quantitative results for normalized experiments [6].

Produced models proved to be very useful when behavior of bulk materials under normalized conditions is investigated. For experimental testing of materials in terms of fracture and fatigue behavior several simplifications can be used with very small, almost insignificant impact on investigated results. However, in cases where the influence of microstructure of material has to be accounted for, the basic fracture mechanics models fail to produce satisfactory results or to describe experimentally observed phenomena.

In more in-depth research the crack front and faces geometry cannot be assumed with simple, planar geometry. It has been shown [1, 7, 8] that fractures (particularly under the remote shear loading) exhibit geometrical changes on the microstructure level of the crack front and flanks which leads to crack front and flanks roughness.

Some simple approaches to account for geometrical microstructure of cracks for basic loading were already created [9, 10]. Also, the crack front kinks after fracture advancements were introduced (e.g. by Bechtle et al. [11], Benedeti et al. [12] and Pant et al. [13], to account for some kind of material microstructure) but they represent only a simple approach in this field.

This work aims to investigate those cases of cracked specimens where planar simplifications of the crack shape are not usable and where it would lead to some discrepancies in results. Moreover, it is aimed at those cases where the planar model cannot sufficiently describe observed phenomena. Especially the shear mode loaded cracks (when there is no mode I crack opening) can be affected by real-like geometry of the crack (Fig. 1) which is in fact governed by the microstructure of used material (grain size etc.) and crack faces and front have a tortuous shape on a micro-scale level [1, 7, 8]. The micro-deviations of fracture geometry lead to the local mixed-mode loading and thus the results are different from standard models.

Some influence of the crack roughness has been already investigated but mainly for normal mode I loading [9, 10] and not for shear modes II and III and their combination II+III. Recent development shows that shear modes are becoming more significant thus this research can improve the knowledge in the field of modern fracture mechanics.

2 Theory - linear fracture mechanics

Standard approach to obtain stress and strain fields around the crack front divides loading according to deformation of the crack into three basic types – mode I (normal mode), mode II (in-plane shear mode) and mode III (out-of-plane shear mode).
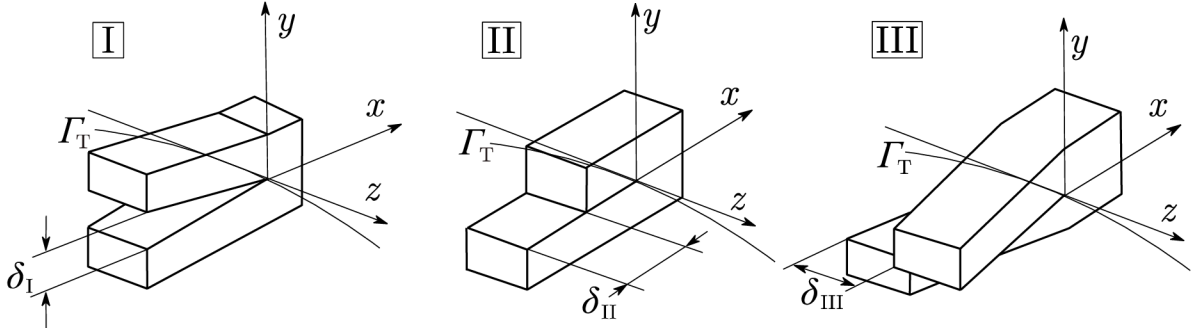
Fig. 2: Loading modes

If the crack front is curved (described by the path Γ_T in Fig. 2), the three-dimensional character must be taken into account. The stress state varies along the crack front and, in general, it is composed of the fields corresponding to the three crack opening modes. The real-like crack can be solved by superposition of these three modes (Fig. 2). Mode I represents pure normal loading of the crack (with the opening δ_I) and modes II and III are related to pure shear loading (with the crack faces displacements δ_{II} and δ_{III}). It was proved that fractures in objects propagate mainly in mode I and even if the crack is originally loaded by pure shear mode the propagation tends to divert to normal mode I loading [14]. This means that historically the mode I crack behavior and the mode I propagation is well known [6] while the shear modes II and III are subjected to less research.

2.1 K-conception

The stress fields ahead of a crack tip in an isotropic linear elastic material can be written [15, 16] as:

$$\sigma_{ij}\left(K,r,\varphi\right) = \frac{K}{\sqrt{2\pi r}} \cdot f_{ij}\left(\varphi\right), \tag{1}$$

where σ_{ij} represents the stress tensor components, r is the distance from the crack tip, function f_{ij} stands for dependence of the stress field on the geometry and loading type and it is formulated with use of angular coordinate φ around the crack tip and K is the stress intensity factor. The stress intensity factor determines a stress singularity at the crack tip and can be expressed in separate form for each loading mode [15] and in these forms it is commonly used for calculations in the field of linear-elastic fracture mechanics:

$$K_i\left(\sigma,a,L_i\right) = \sigma\sqrt{\pi a} \cdot k_{cal}\left(a,L_i\right) \quad \text{where} \quad i = \text{I, II, III.} \tag{2}$$

Described stress intensity factor is defined by the stress σ in the body with fracture, by the length of crack a and by the calibration function k_{cal} which is related to length of crack a and to the characteristic geometrical dimension L_i of cracked body.

2.2 Energetic approach

The second commonly used method in the fracture mechanics is an energetic approach developed by Irwin [3, 4]. This approach is based on the energy balance of the system consisting of fractured body and external forces described by the elastic energy of fractured body W_e and the potential energy or work of external forces W_p. Their combination forms energy of the entire system W_c. With these energies in mind Irwin established a crack driving force G as a change of the energy of system W_c in dependence on the change of crack length a [17]:

$$G = \frac{\mathrm{d}W_c}{\mathrm{d}a}. \tag{3}$$
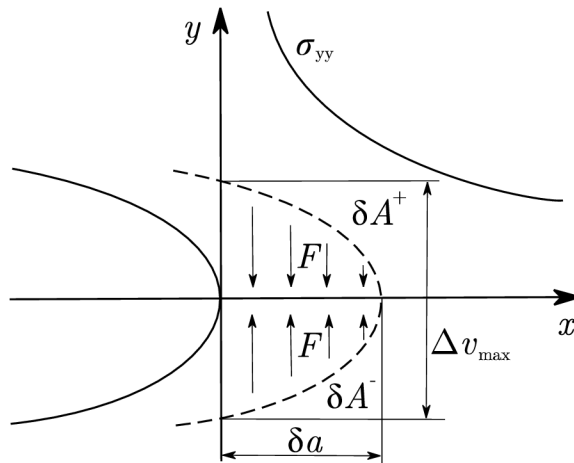
Fig. 3: Scheme of the crack tip opening displacement for energetic approach

The crack driving force G can be also considered as an energy which is released upon the extension of crack. While the crack is extended by the length δa (Fig. 3), the energy W_c (the sum of δA^+ and δA^-) is absorbed by external forces F which act as a counterpart to the crack opening. Their energy W_p is in this case (Fig. 3) described by the stress component σ_{yy} and by the crack tip opening displacement Δv [14] (which is related to the previously described stress intensity factor and the material characteristics – Young's modulus E and Poisson's ration μ):

$$\delta W_p = \frac{1}{2} \int_0^{\delta a} \sigma_{yy}(x,0)\Delta v \mathrm{d}x, \tag{4}$$

$$\Delta v = \frac{K}{\sqrt{2\pi}} \cdot \frac{8 \cdot (1-\mu^2)}{E} \cdot \sqrt{\delta a - x}. \tag{5}$$

With the use of energy balance and the above mentioned equations (4) and (5) the relation between energetic approach and the K-conception can be given by (this relation is valid only for the linear-elastic fracture mechanic conditions) [17]:

$$G = \frac{K_{\mathrm{I}}^2}{E'} + \frac{K_{\mathrm{II}}^2}{E'} + \frac{K_{\mathrm{III}}^2}{2E_{\mathrm{shear}}},$$ (6)

where E' equals Young's modulus E for plane stress conditions and $E' = E/(1\text{-}\mu^2)$ for plane strain conditions (μ stands for Poisson's ratio) and E_{shear} is the shear modulus.

2.3 J-integral conception

The third commonly used conception in the field of fracture mechanics is the J-integral conception. It is widely used for modeling and calculations under both linear-elastic and elastic-plastic conditions which can occur when materials with low value of yield strength are used [14]. For example, the K-conception cannot be used under such conditions.
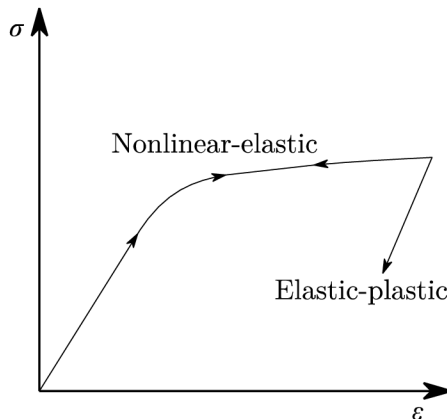
Fig. 4: Nonlinear assumption of material behavior

Rice [5] utilized the simplification of the elastic-plastic material properties – the original stress strain curve can be substituted by the nonlinear-elastic material behavior (Fig. 4). By this assumption Rice [5] could extend the standard fracture mechanics beyond the linear-elastic limitations. The reason was the fact that for the loading phase the stress-strain curve of nonlinear-elastic material behavior is identical to an elastic-plastic material response (Fig. 4) thus the theory of plasticity is in this area of interest similar to the nonlinear elasticity [17].

With this idealization (Fig. 4) in mind the J-integral could be formulated [5] as an energy release rate in a cracked body:

$$J = -\frac{\mathrm{d}\Pi}{\mathrm{d}A},$$ (7)

$$\Pi = U - P\Delta = -U^*,$$ (8)

$$U^* = \int_0^P \Delta \mathrm{d}P.$$ (9)

5
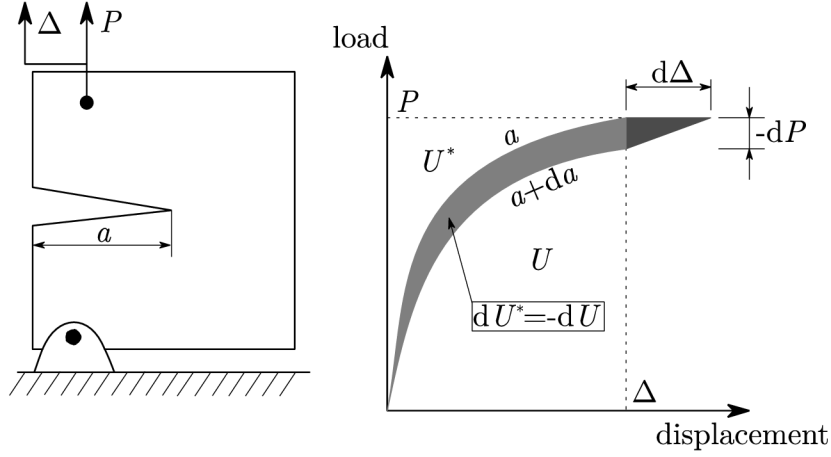
Fig. 5: Load-displacement curve for object with the fracture (example)

In equation (7) the A stands for the surface of crack and the Π is the potential energy of a cracked body, derived from the strain energy U, deformation of the body Δ and work of the external forces P (8). The energy Π can be also obtained [17] in an integral form (9). Used parameters are described in the picture above (Fig. 5).
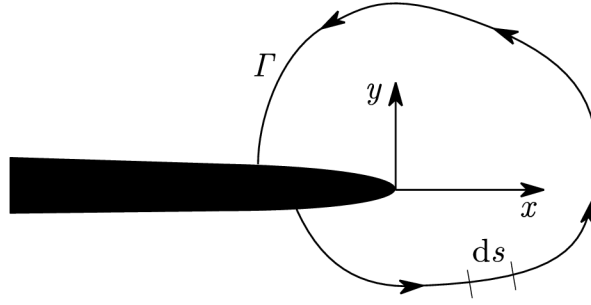
Fig. 6: The crack integration path (2D example)

With use of equation (9) and for simplified 2D geometry (Fig. 6) the J-integral can be expressed as [14]:

$$J = \int_{\Gamma} \left(w_{e} \mathrm{d}y - T_{i} \frac{\partial u_{i}}{\partial x} \mathrm{d}s \right), \tag{10}$$

$$w_{e} = \int_{0}^{\varepsilon_{ij}} \sigma_{ij} \mathrm{d}\varepsilon_{ij}, \tag{11}$$

where T_{i} are components of the vector of surface forces in perpendicular direction to the integration path Γ, u_{i} are the components of a vector of relative displacements, s stands for the length of integration path and w_{e} is the strain energy density (σ_{ij} and ε_{ij} are the stress and strain tensor components).

Furthermore Rice [5] proved that the J-integral itself is independent on the integration path (as long as it starts at one side of the crack and ends on the other, see Fig. 6) [9, 10].

6

If the linear-elastic fracture mechanics conditions are met then the J-integral can be also decomposed to the stress intensity factors K_i (i = I, II, III) for plane strain conditions:

$$J = \frac{1+\mu}{E}\left[\left(1-\mu\right)\left(K_I^2 + K_{II}^2\right) + K_{III}^2\right], \tag{12}$$

or for plane stress conditions:

$$J = \frac{1}{E}\left[K_I^2 + K_{II}^2 + \left(1+\mu\right)K_{III}^2\right], \tag{13}$$

where μ and E stand for the Poisson's ratio and Young's modulus respectively.

2.4 Evaluation of fracture parameters using Ansys code

Calculations of fracture parameters described in chapters 2.1 - 2.3 are useful only in conjunction with the simplified models of fractures or they have to be adjusted to work with some irregularities and then these approaches are too complicated for routine use. Therefore, a different approach was devised – use of finite element method (FEM), for example Ansys code.

The accuracy of evaluated results by FEM is directly connected to appropriate construction of the finite element mesh. The mesh can be either very fine or it can exploit known qualitative properties of expected stress and strain fields in the model. The first approach leads to huge models with very long evaluation times, so it is not suitable unless a very fast and advanced workstation is available. On the other hand, for modeling of cracks the second approach can be used very easily. The stress (strain) around the crack tip decreases radially from singularity at the crack tip to nominal values far away from the crack (as shown in formula (1)). This radial distribution can be matched with radially created finite elements mesh.
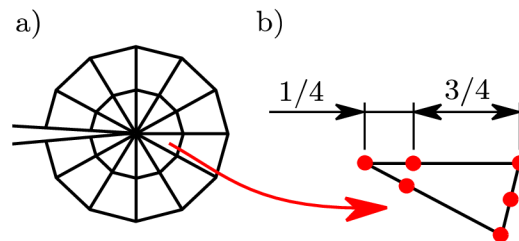
Fig. 7: a) Example of the finite element mesh around the crack tip, b) schema of shifted mid-side nodes (red dots represent nodes)

Final mesh consists of one row of wedge elements around the crack tip and radially enlarging standard elements (see Fig. 7 – a)).

To enhance this type of mesh one "numerical trick" can be used. The quadratic elements (with quadratic base functions, see [18]) have evaluation node in each corner and also one in the middle of each side, so-called mid-side node. If this node is closer to one side of the element it creates numerically introduced artificial singularity and

if the mid-side node is exactly in ¼ of the side of element (see Fig. 7 – b)) the artificial singularity corresponds to the square-root singularity of the strain and stress field near the crack tip [19–21]. With a well resolved FE mesh the fracture parameters can be evaluated using several Ansys build-in features.

2.4.1 Contour integration method

With use of the CINT sub-routine [18] both J-integral and K-factors (and several other parameters [18]) can be evaluated. At first a local coordinate system with the x-axis in the direction of the crack and the y-axis in the direction perpendicular to the crack faces must be created and appointed to specific node at the crack tip. Then by numerical contour integration through the elements around the crack tip, the J-integral can be calculated directly [18] by formula:

$$J = \sum_{ie=1}^{ne} \left[\sigma_{ij} \frac{\partial u_j}{\partial x_l} - w\delta_{li} \right] \frac{\partial q}{\partial x_i} w_{e,ie} A_{ie}, \tag{14}$$

where ne is the number of elements to be integrated, σ_{ij} is the stress tensor, u_j is the displacement vector, w_e is the strain energy density, δ_{ij} is the Kronecker delta, x_i is the coordinate axis, q is referred to as the crack-extension vector, w_{iw} is the weight function, and A_{ie} is the area of the element represented by ie. Equation (14) was derived from standard approach by Shih [22].

Evaluation of the stress intensity factors is not so simple. They are derived from so-called interaction integral I which is expressed by following formula [18]:

$$I = -\int_V q_{ij} \left(\sigma_{kl} \varepsilon_{kl}^{aux} \delta_{ij} - \sigma_{kj}^{aux} u_{ki} - \sigma_{kj} u_{ki}^{aux} \right) dV / \int_s \delta q_n ds, \tag{15}$$

where σ_{ij}, ε_{ij} and u_i are the stress, strain tensors and the displacement vector, σ_{ij}^{aux}, ε_{ij}^{aux} and u_i^{aux} are the stress, strain and the displacement of the auxiliary field and q is the crack-extension vector. Classical integration from formula (15) is transformed to numerical integration for purposes of FEM. Evaluated I-integral is then associated with the stress intensity factors by relation [18]:

$$I = \frac{2}{E'} \left(K_I K_I^{aux} + K_{II} K_{II}^{aux} \right) + \frac{1}{E_{shear}} K_{III} K_{III}^{aux}, \tag{16}$$

where K_i (i = I, II, III) are mode I, II and III stress intensity factors, K_i^{aux} (i = I, II, III) are auxiliary mode I, II and III stress intensity factors, E' equals to E for plane stress and $E/(1-\mu^2)$ for plane stress (E stands for Young's modulus), μ is Poisson's ratio and E_{shear} is shear modulus. From relations (15) and (16) Ansys software can obtain values of the stress intensity factors via its internal procedures [18].
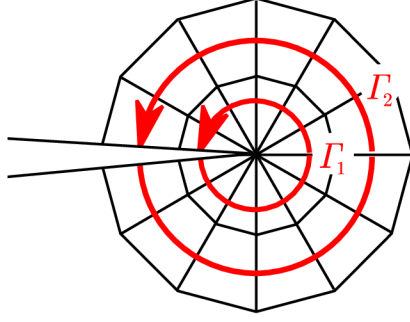
Fig. 8: Example of two integration contours Γ_1 and Γ_2

Both procedures (calculation of the *J*-integral and the *K*-factors) uses numerical integration along contours Γ. Number of contours is adjustable, and they are always constructed through the closest row of the elements around the crack tip (example of two integration paths is in Fig. 8).

The contour integration method is quite easy to implement in parametric simulations and it yields accurate results. Nevertheless, it can be used to evaluate both the SIFs and the *J*-integral, while the second mentioned fracture parameter can be evaluated even when the isotropic plasticity is used for material model in simulation (the SIFs can be evaluated only with assumption of linear-elasticity). For these reasons in calculations presented in this thesis only the contour integration method was used.

2.4.2 Displacement extrapolation method

The second (and original) method for evaluation of SIFs at the crack tip is the displacement extrapolation method [18]. This method uses analytically predicted deformation around the crack after loading and it finds the SIFs values according to the best fit of these functions through 3 or 5 points along the crack flanks. The interpolation functions are based on simple relations of displacements u_x, u_y and u_z [17] evaluated from all three loading modes:

$$u_x^{\mathrm{I}} = \frac{K_{\mathrm{I}}}{2E_{\mathrm{shear}}}\sqrt{\frac{r}{2\pi}}\cos\left(\frac{\varphi}{2}\right)\left[\kappa - 1 + 2\sin^2\left(\frac{\varphi}{2}\right)\right],$$

$$u_x^{\mathrm{II}} = \frac{K_{\mathrm{II}}}{2E_{\mathrm{shear}}}\sqrt{\frac{r}{2\pi}}\sin\left(\frac{\varphi}{2}\right)\left[\kappa + 1 + 2\cos^2\left(\frac{\varphi}{2}\right)\right],$$

$$u_y^{\mathrm{I}} = \frac{K_{\mathrm{I}}}{2E_{\mathrm{shear}}}\sqrt{\frac{r}{2\pi}}\sin\left(\frac{\varphi}{2}\right)\left[\kappa + 1 - 2\cos^2\left(\frac{\varphi}{2}\right)\right], \tag{17}$$

$$u_y^{\mathrm{II}} = -\frac{K_{\mathrm{II}}}{2E_{\mathrm{shear}}}\sqrt{\frac{r}{2\pi}}\cos\left(\frac{\varphi}{2}\right)\left[\kappa - 1 - 2\sin^2\left(\frac{\varphi}{2}\right)\right],$$

$$u_z^{\mathrm{III}} = \frac{2K_{\mathrm{III}}}{E_{\mathrm{shear}}}\sqrt{\frac{r}{2\pi}}\sin\left(\frac{\varphi}{2}\right),$$

where E_{shear} is the shear modulus, φ and r are the polar coordinates around the crack tip and $\kappa = 3 - 4\mu$ (plane strain) or $\kappa = (3 - \mu)/(1 + \mu)$ (plane stress) where μ is the Poisson's ratio.

To properly evaluate the coefficients K_{I}, K_{II} and K_{III} the local coordinate system for the crack tip must be created. The origin of the new system is at the crack tip, the x-axis must be parallel to crack faces and y-axis must be perpendicular to the crack faces.
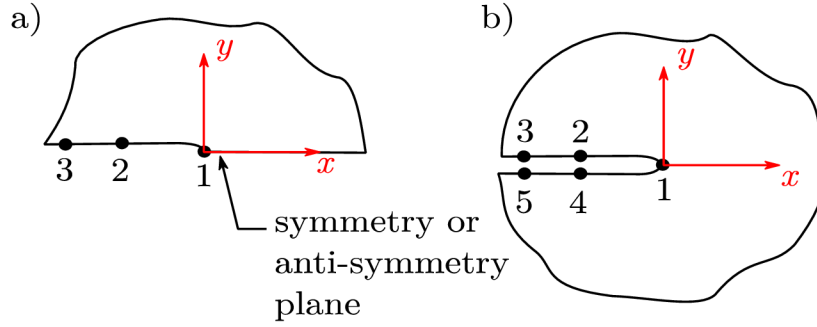
Fig. 9: Scheme of the coordinate system and evaluation nodes placement for KCALC subroutine for a) symmetrical (or anti-symmetrical) and b) fully modelled crack

After the definition of correct coordinate system (Fig. 9), the new path has to be created using the Ansys PATH command. It should contain 3 (for the symmetrical or anti-symmetrical crack) or 5 (for full crack model) nodes on the specific locations along the crack flanks (see numbered points in Fig. 9).

After the characterization of evaluation nodes and coordinate system, the plane strain or plane stress conditions and the crack symmetry (if present) must be specified via KCALC subroutine [18] and in the postprocessor unit the resulting SIFs can be evaluated from deformation fields around the crack tip.

This method is simple to use, and it does not need any additional extensive computational time but on the other hand our comparison with contour integration method revealed that this type of SIFs evaluation is strongly dependent on exact locations of evaluation nodes (which is not exactly defined or described in Ansys support materials [18]). Also, this method provides only the SIFs as a result and is useable only for linear-elastic, homogenous material behavior.

2.4.3 Energy-release rate calculation

This approach for evaluation of the energy-release rate is based on virtual crack-closure technique (VCCT). The VCCT method assumes that the energy needed to separate a surface (crack advancement) is the same as the energy needed to close the same surface. In Ansys finite element (FE) software, the basic VCCT method is modified and assumes further that the stress state around the crack tip does not change significantly for crack growth by a small amount [18].
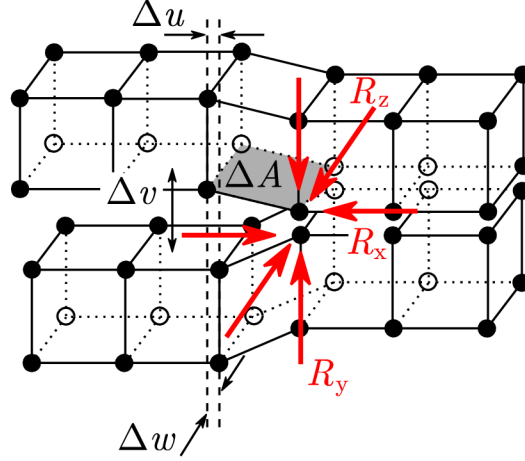
Fig. 10: Schematic of the 3D crack geometry with parameters for VCCT method

The energy-release rate G_i for the 3D crack geometry for VCCT method is defined as [18, 23, 24]:

$$G_I = -\frac{1}{2\Delta A} R_y \Delta v,$$

$$G_{II} = -\frac{1}{2\Delta A} R_x \Delta u, \tag{18}$$

$$G_{III} = -\frac{1}{2\Delta A} R_z \Delta w,$$

where G_I, G_{II} and G_{III} represent the energy-release rate for modes I, II and III respectively, Δu, Δv and Δw are the relative displacement between top and bottom nodes of the crack face in the local coordinates x, y and z respectively, R_x, R_y and R_z are the components of reaction forces at the crack tip node and ΔA is the crack-extension area (all mentioned characterizations are visible in Fig. 10).

Actual evaluation of the energy-release rate is performed with use of CINT function (already mentioned in the chapter 2.4.1), for the VCCT method the crack tip node component and the crack-extension direction must be specified similarly to evaluation of the J-integral described in the chapter 2.4.1. For the crack-extension direction the VCCT method requires that the FE mesh nodes are present at their exact direction whereas the J-integral calculation does not.

The VCCT method allows to obtain G_I, G_II and G_III for models with linear-isotropic, orthotropic or anisotropic elasticity used for material model. Under these assumptions the energy-release rate can be assumed as equal to the J-integral.

2.5 Shear modes

Despite the initial importance and extensive research of the fractures loaded by normal mode I, the research on shear cracks started slowly with early works [25–27] on I+II and I+III mixed mode loading. Pure mode II and III loading and also combination of shear modes II+III were under more complex investigation later [28–30]. For the purpose of investigation of shear modes several specimens and loading setups were used.
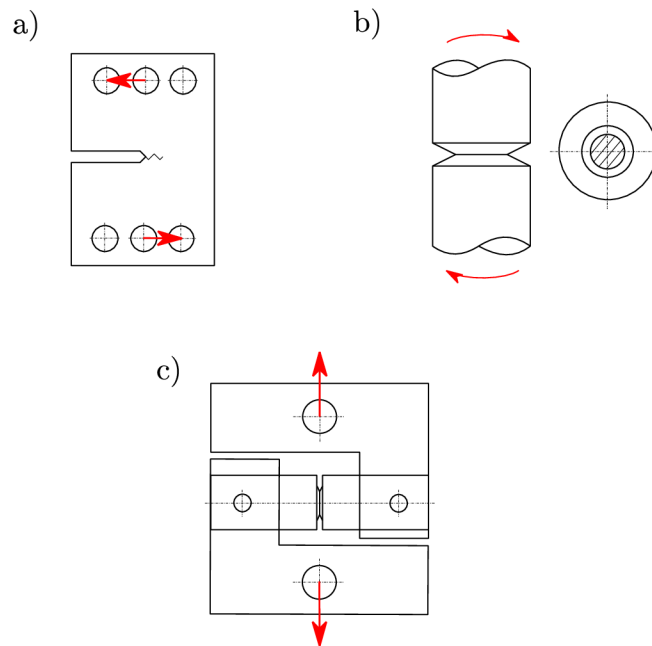
Fig. 11: Example of the three experimental setups for shear mode loading

Two widely used specimen geometries and the experimental setups for shear mode loading are the Compact-Tension-Shear (CTS) specimen (Fig. 11 – a)) for pure mode II loading and circumferentially cracked cylindrical specimen which can be loaded by torsion for pure mode III loading (Fig. 11 – b)) or by shear to investigate pure modes II and III and mixed-mode loading II+III on one specimen simultaneously (Fig. 11 – c)).

The CTS specimen, originally developed by Richard [31, 32], is a plate with crack with geometry very similar to the Compact-Tension (CT) specimen. For pure mode II loading it has to be loaded in the direction of crack (Fig. 11 – a)). With the special gripping device this specimen can be used also for mixed mode I+II loading [33, 34].

The cylindrical specimen loaded by torsion (Fig. 11 – b)) allows to easily obtain results for pure mode III loading along the whole circumferential crack. The specimen itself is a cylinder with circumferential notch in the middle and from its tip a crack starts to propagate. The loading by torque moment does not introduce any other type of loading thus from the global view no mode combination (or mixity) is present.

The last specimen depicted in Fig. 11 – c) was introduced and is used in a special experimental setup to investigate mixed-mode II+III loading (for example [7, 35, 36]). It uses the same cylindrical specimen as in the torsion setup (mentioned above). The griping device was developed to bend the specimen as a whole. But in place, where the crack is, the bending momentum equals zero and the only acting force is the shear force. Testing and modeling of this experimental setup proved that around the circumference of the specimen there is only mode II, III and II+III loading [7, 36–40].

2.5.1 CTS specimen

As was mentioned in the chapter above, the CTS specimen was developed for investigation of the cracks loaded by pure mode II and mixed-mode I+II loading. The specimen was created with several requirements in mind [32]: the specimen has simple and compact shape, pure shear mode loading is distributed over large area of the specimen, the crack tip is loaded only by pure shear mode and the stress conditions are little affected by global geometric alterations.

$a = 0.55 - 0.65w$

$c = 1.2w$

$f = 0.2w$

$h = 1.7w$

$r_g = 0.075w$
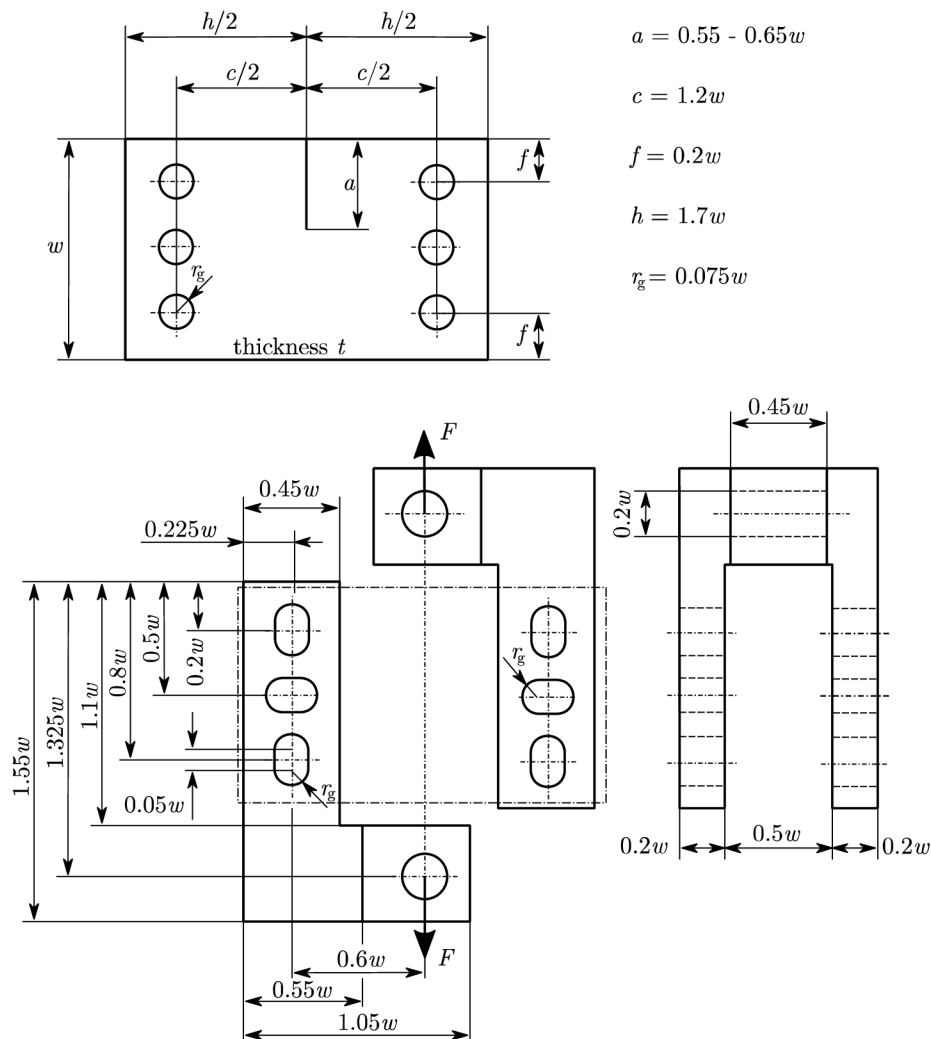
Fig. 12: Original CTS specimen specifications [32]

Above mentioned specifications clearly show that the CTS specimen (Fig. 12) represents a good testing setup for pure mode II shear loading.

Richard used the equation for analytical calculation of the stress intensity factor K_{II} for original CTS specimen with relative dimensions [32] (which was later rearranged by Plank and Kuhn [41]) from where the K_{II} can be derived:

$$K_{II} = \frac{F}{t}\sqrt{\pi a} \cdot (w-a)^{-1} \left[\frac{-0.23 + 1.4 \cdot \dfrac{a}{w-a}}{1 - 0.67\dfrac{a}{w-a} + 2.08\left(\dfrac{a}{w-a}\right)^2} \right]^{\frac{1}{2}}, \qquad (19)$$

where F is the applied force, t is the thickness of the specimen and a and w are the characteristic dimensions of the specimen (see Fig. 12).

Richard and Benitz later improved and furthermore investigated this type of specimen [31] and they also adjusted the loading device for mixed-mode I+II loading [31].

In more recent works Li et al. investigated fracture behavior of the CTS specimen under pure mode II and mixed mode I+II loading [33, 34]. They used numerical fracture analysis and modeled the CTS specimen as a 3D geometry thus they obtained the stress intensity factors values along the whole crack front. The results for pure mode II loading were in good accordance with the original Richard's work [33, 34].
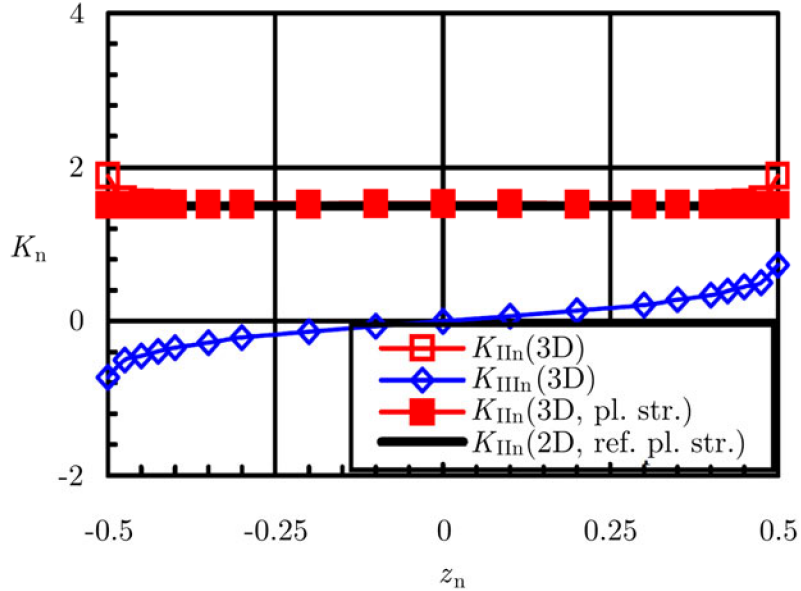
Fig. 13: Example of results obtained by Li et al. [33]

The results which are depicted in chart above (Fig. 13) are normalized stress intensity factor values (in accordance with the original Richard's idea [32]):

$$K_{i,n} = \frac{K_i}{\dfrac{F}{wb} \cdot \sqrt{\pi a}} \qquad \text{where} \quad i = \text{I, II, III,} \qquad (20)$$

as a function of normalized thickness coordinate z_n which is 0 for the middle of the specimen and ± 0.5 for free surfaces of the specimen [33, 34].

In these works the mixed mode I+II loading and the inclined crack path were also investigated [34]. Among other things the results showed that the CTS specimen is suitable for such research of the shear mode fractures and also that on both sides of the specimen there is some amount of induced mode III loading (caused by Poisson's ration influence on the free surface of specimen [6], see Fig. 13) and also mode I loading for the inclined cracks [34]. Both phenomena were observed even when pure remote mode II loading was applied [33, 34].

2.5.2 Cylindrical specimen

As described in the chapter 2.5, the cylindrical specimen can be used for the two types of experimental setups – torsion and shear loading. For both setups the same geometry of specimen can be used – a cylindrical bar with circumferential notch. The crack itself propagates from the tip of the notch.
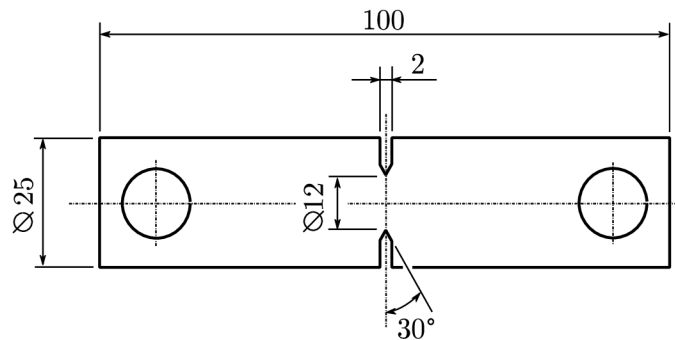
Fig. 14: Schema of the cylindrical specimen (example dimensions)

2.5.2.1 Torsion loading

For pure remote mode III loading a torsion loading of cylindrical specimen is ideal. For pure torsion loading the specimen (Fig. 14) was clamped in a special device (Fig. 15) which transforms push-pull loading into torsion momentum [42].
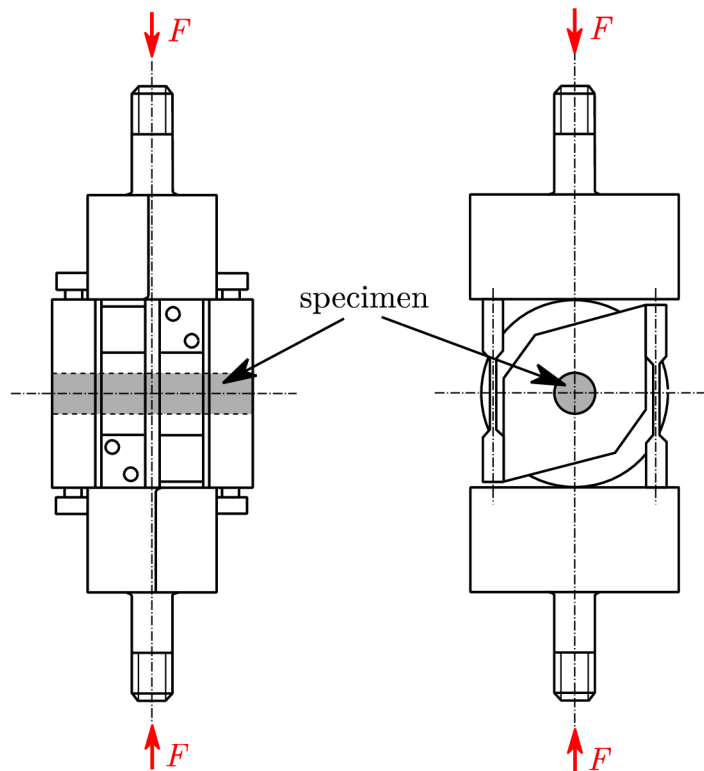
Fig. 15: Schema of the torsion loading device [42]

For analytical evaluation of corresponding mode III SIF the following formula can be used [42]:

$$K_{III} = \frac{16T}{\pi D^3}\sqrt{\pi a} \cdot Y_{III}, \tag{21}$$

where T is the loading torque, D is the outer diameter of specimen, a is the total crack length and Y_{III} is a geometry factor depending on overall geometry of the specimen. Factor Y_{III} can be derived from asymptotic relations introduced by Benthem and Koiter [43]. After appropriate adaptation the function Y_{III} can be written as [42]:

$$Y_{III} = \xi^{-\frac{5}{2}}\left(1 + \frac{1}{2}\xi + \frac{3}{8}\xi^2 + \frac{5}{16}\xi^3 + \frac{35}{128}\xi^4 + 0.208\xi^5\right). \tag{22}$$

Factor Y_{III} in (22) depends only on ratio $\xi = d/D$ of the inner diameter of specimen d (the un-cracked portion of specimen $d = D - 2a$) and the outer diameter of the specimen D and it can be used with the formula (21) with better than 99% accuracy [44].

2.5.2.2 Shear loading

To test pure remote mode II and III and also mixed-mode II+III loading on one specimen simultaneously a special testing device had to be utilized [35, 36].
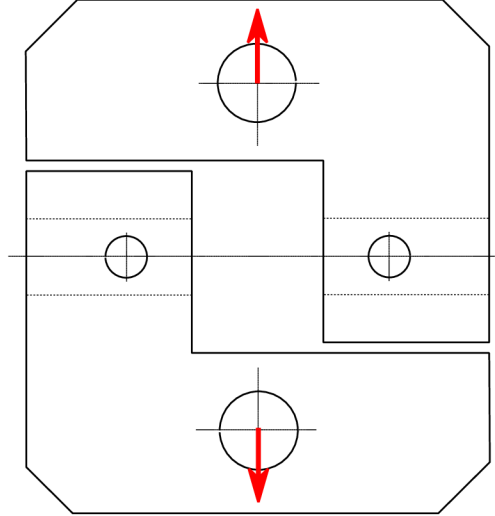
Fig. 16: Schema of the testing device for shear loading of the cylindrical specimen

The gripping device (Fig. 16) can be easily mounted in a push-pull device to transform the tensile forces to simple shear loading. The specimen itself is clamped in the central location of the device which assures that at the central point (where the notch with crack is present) the bending momentum is exactly zero, therefore no superimposed mode I is present.

Actual distribution of modes II and III loading at the crack front around the specimen changes from pure mode II loading to pure mode III loading.
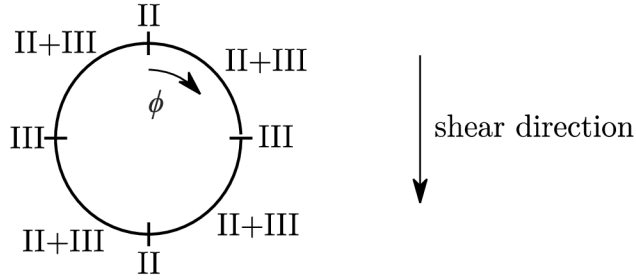
Fig. 17: The specimen cross-section with the corresponding loading modes

At the top and bottom of the specimen a pure mode II loading is present, at sides of the specimen a pure mode III loading is present and between these special points a mixed-mode II+III loading is present (Fig. 17). Loading components are functions of polar coordinate ϕ. Our previous research showed that for coordinate system with $\phi = 0°$ at the top of the specimen the mode II and III SIFs follow functions $\cos(\phi)$ and $\sin(\phi)$ respectively [37].

The maximal values of K_{II} (at $\phi = 0°$ and $180°$) and K_{III} (at $\phi = 90°$ and $270°$) can be expressed as [42]:

$$K_i = \frac{4F}{\pi D^2}\sqrt{\pi a}\cdot Y_i; \quad i = II, III,$$ (23)

where F is the loading force, D is the specimen outer diameter, a is the total crack length and Y_i are the geometrical correction factors. The actual functions of Y_i in equation (23) were derived from FEM results by Horníková et al. [37] and for dimensions of the specimen used in this research are expressed as [42]:

$$Y_{II} = 27.7861\cdot\left(\frac{a}{2}\right)^{0.388981}$$ (24)

and:

$$Y_{III} = 8.15575\cdot\left(\frac{a}{2}\right)^{0.173354}.$$ (25)

Expressions of Y_{II} and Y_{III} in equations (24) and (25) are shown only as a functions of the crack length a. Actual correction factors should be functions also of the specimen dimensions but for this experimental setup a valid K-calibration was done only for one size of the specimen (same as in **Fig. 14**) and thus the relation between geometrical factors and the specimen dimensions is unknown.

2.6 Influence of the crack front and flanks microstructure on the SIFs

Material characteristics related to the fracture mechanics are derived from experimental results, but the data evaluation is based on elementary theory for homogenous body with straight planar crack. This theory generally does not account for microstructural patterns of the crack front and flanks. However, changes of shape of the crack front due to microstructural heterogeneities in material belong to toughening mechanisms [45, 46]. Moreover, even if the specimen is loaded by the pure remote mode loading the tortuous shape of crack front leads to decrease of the crack driving force caused by localized mixed-mode I+II+III loading [47, 48].

Influence of the crack roughness on changes of the crack driving force is called roughness induced shielding (RIS) [10] and it can be seen from various points of view. During the last decades, there have been some works submitting and solving 2D models of RIS [9, 49–52] but these models were far from explaining the real implications of RIS on the fracture behavior even for simple normal loading.

The RIS can be observed from three points of view. The first one was the most investigated in past years and it is related to the crack faces interaction. When remote mode III loading is present, the crack faces slide on each other. If no remote mode I is present and crack faces are assumed to be planar, there should be no crack faces interaction. However, real-like cracks are rough and some mode I loading is almost always present in the real applications.
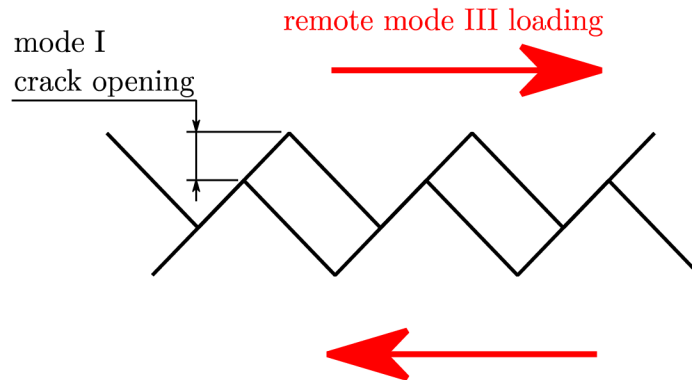
Fig. 18: Example of zig-zag shaped crack under remote mode III loading

When just a simple zig-zag shape of crack faces and pure remote mode III loading is assumed (see Fig. 18), crack faces start to interact, and the effect of this interaction is inducement of mode I loading and crack opening. These phenomena were investigated by several authors, for example Gross and Mendelsohn [53], Vaziri and Nayeb-Hashemi [54] or Gates and Fatemi [55].

The second one is related to the linear crack front roughness where a zig-zag crack front shape (either simplified or not) is assumed, but the crack front geometrically stays in plane of fracture.
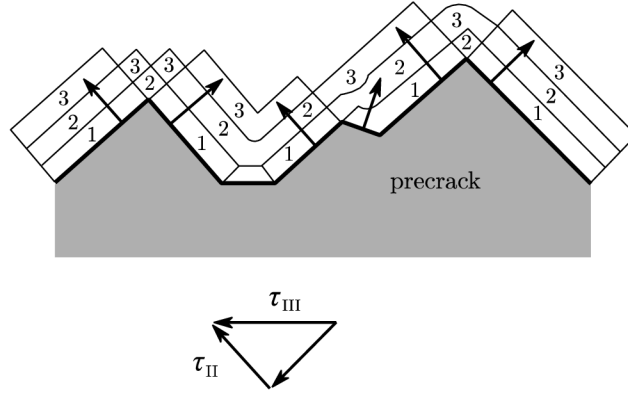
Fig. 19: Local mode II advances of the crack under remote mode III loading [56],
$\boldsymbol{\tau}_{II}$ *and* $\boldsymbol{\tau}_{III}$ *stand for mode II and III shear stress components*

It was proved that for serrated cracks under remote mode III loading (Fig. 19) there are present local mode II advances of the crack front [56] and thus the crack front geometry has significant impact on the crack propagation.

In the third approach a full 3D crack model has to be employed. In this case a small portions of crack are assumed to be kinked in a 3-dimensional space.
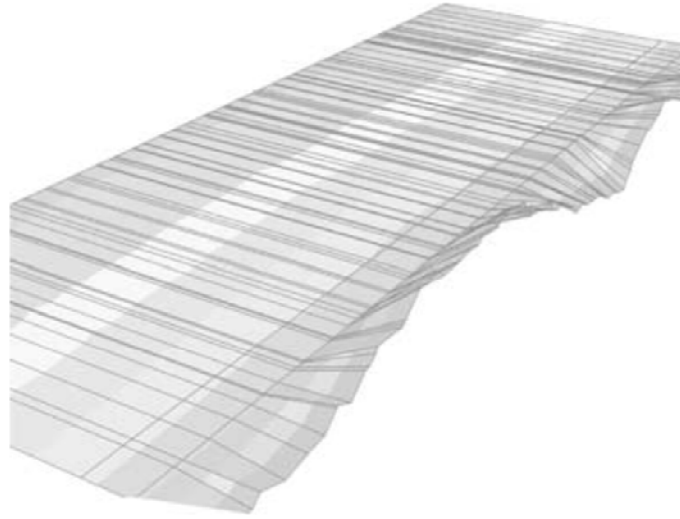
Fig. 20: Intergranular crack front ("pyramidal model" used by Pokluda et al. [10])

However, the crack kink angle is not uniform along the whole width of crack, it is changing instead (Fig. 20). In the year 2003 a statistical approach to this type of crack was introduced [10] for remote mode I loading. This approach accounted for statistical appearance of the fracture roughness and employed a method for quantitative interpretation of some phenomena related to RIS in metallic materials with use of "pyramidal model" of intergranular crack front solved analytically and numerically.

3 Aims of the thesis

As was described in review in chapter 2.6 there is some research accounting for the crack front and flanks microstructure, but the knowledge aimed on the fracture mechanics specialized on effects caused by small structural deviances from ideal shape is poor, especially in the field of remote shear mode loading. Even if some simplifications are taken into consideration, the most of existing studies are aimed only on the basic configurations and normal mode I loading [10]. Research from present perspective shows that knowledge aimed only at normal mode loading is not sufficient in order to fully understand all intricacies of the fracture mechanics. Therefore, this work aims to contribute to present research on shear loaded fractures affected by deviances from standardized and long used models. Tracked and investigated deviances are mainly the geometrical abnormalities of the fracture geometry from generally used planar models of the crack.

a)   b)
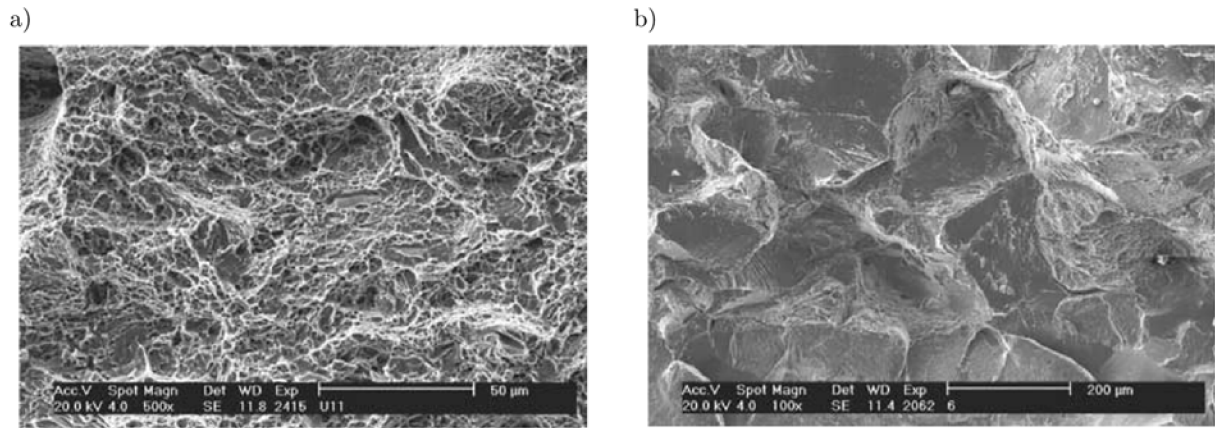
Fig. 21: The fracture surface morphology (two different fracture mechanisms:
a) - transgranular, b) - intergranular) [10]

These variances of the fracture surfaces exhibit in different forms for almost all fracture mechanisms. They are mainly governed by the grain structure and microstructural composition of real materials, such as polycrystalline metallic materials (e.g. iron, niobium, etc.). As was mentioned above, these geometrical nuances are mostly deemed as insignificant and their influence is not evaluated. However, if the complex crack shape should be modeled more realistically, the microstructure could be viewed from several different angles.
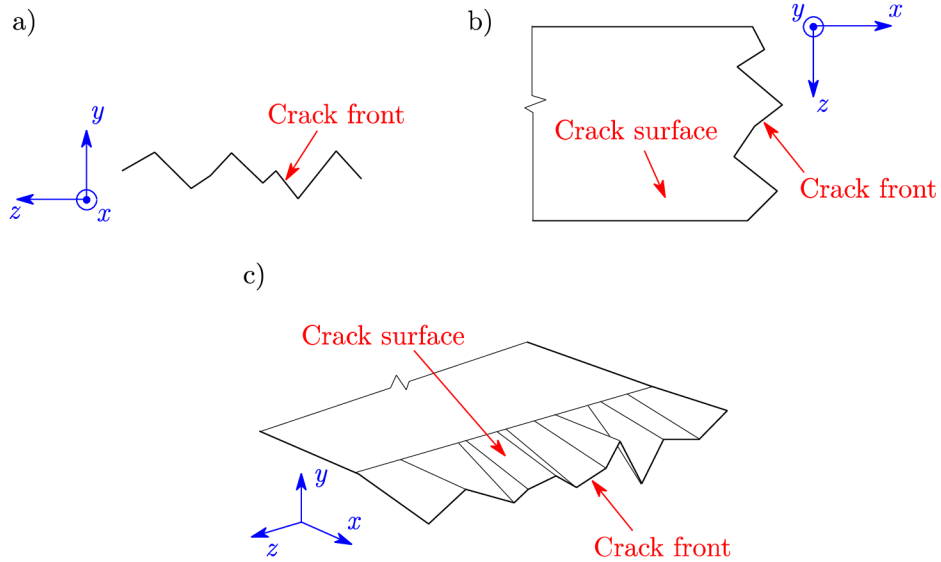
Fig. 22: Schematic examples of the crack microstructure with: a) out-of-plane tortuosity, b) in-plane tortuosity, c) partial tortuosity with twist and kink of the crack

Some examples of the crack micro-geometries are shown in Fig. 22 where all three examples are cracks where the x-axis denotes the general crack propagation direction and the x-z plane is the general crack plane. Schema a) shows the crack with only out-of-plane tortuosity where the crack plane is rough along its whole length, but the crack front lies still in one plane parallel to the y-z plane, schema b) shows in-plane tortuosity where the crack flanks are ideally planar and only the crack front shows tortuosity, but still in the plane x-z, schematic c) then shows partially rough crack with both kink and twist of the crack. In case c) the crack front can lie in one plane the same as in schema a), but it can also introduce some crack front tortuosity like in the schema b). Of course, the combination of cases a) and b) can be modeled too and it is closer to reality than the separate cases a) and b).

The crack geometries described in paragraph above can lead to local induction of all loading modes I, II and III and their combination I+II+III along the crack front which affects resulting crack behavior and if this phenomenon occurs for example during some fracture toughness measurement, actual measured value obtained by standard methods can be affected by significant error, because present models and methods do not take into account these phenomena.

Research in this thesis deals with investigation of influence of the fracture microstructure on SIFs for cracks subjected to shear mode loading. The aim is to find the relation between the crack front or the crack flanks roughness and fracture parameters. This relation should be investigated for remote mode II and III loading. Pure mode II loading can be investigated using standardized CTS specimen (Fig. 11 – a)). For the pure mode III loading a cylindrical torsion specimen (Fig. 11 – b)) can be used. Investigation of these specimens on which is this thesis aimed should bring some insight to shear modes behavior therefore this thesis will contribute to broadening of the fracture mechanics theory.

Alongside the investigation of influence of the crack front micro-geometry on the fracture parameters some innovative approaches of evaluation of SIFs along geometrically complex fractures should be created. With use of both analytical and numerical (FEM) approaches, new (more universal) mathematical models should be created if possible. This means both pure mode II and III loading and also mixed-mode II+III loading.

Some correlation between presented models and experimental results is also expected. The findings obtained from numerical and analytical modelling should be used to correct the experimental data in terms of accounting for the crack micro-geometry. Moreover, the results should be compared to the research done by different authors.

4 Models and results

In this work two types of mentioned specimens were investigated in detail – the cylindrical specimen and the CTS specimen (see chapter 2.5).

At first, the influence of the crack front zig-zag shape in plane of fracture is discussed and some model simplifications are suggested. For this purpose, the cylindrical specimen was modeled, and some results were used in conjunction with the experimental work of Vojtek et al. [8], done with the same specimen.

The second part of this work aims at decrease of the SIFs due to the crack front and flanks roughness for remote mode II loading. The CTS specimen is suitable to model this type of the crack roughness (for mode II shear loading). The crack geometry was modeled to resemble the crack surfaces observed on real fractures (either with use of in-plane and out-of-plane roughness or with crack front kink and twist, see Fig. 22). Decrease of calculated SIFs was used for correction of the experimental threshold values which were than compared to the theoretical ones predicted by multiscale models.

Part which was done within the frame of this thesis is aimed at numerical modeling of mentioned specimens and actual evaluation of results. While these calculations were compared, verified and used in direct conjunction with the experimental data, the experimental work was only adopted from other authors.

4.1 Cylindrical specimen

The first type of investigated model was the cylindrical specimen. It allowed to look on things of interest for both modes II and III simultaneously, either via torsional loading (see chapter 2.5.2.1) or via shear loading (see chapter 2.5.2.2). Also, the cylindrical symmetry of specimen could be exploited since investigated crack serrations stayed in the plane of crack. Moreover, these models were used in conjunction with the real experiments on fatigue thresholds for mode II and III loading done by Vojtek et al. (e.g. [8, 36, 56]). Partially for that purpose, two material models were used for the cylindrical specimen to simulate the experiments executed on the specimens made out of pure ARMCO iron and niobium.

4.1.1 Numerical model

To obtain actual values of the SIFs along the crack front a numerical model had to be created. All used models were created solely in the Ansys software, all types of simulations were static-structural type with only linear properties taken into account.

Several simplifications of used models had to be considered to obtain sufficiently precise stress and strain fields around the crack front. Also, some special techniques to speed-up the calculations and to obtain more precise results were used. Simplifications were related mainly to the geometry of the crack front (but the crack front asperities were evaluated in the end) and the main special technique which was used is called submodelling.

The submodelling procedure consists of (usually) two-stage modelling where the first model (called global model) represents the whole geometry of the specimen but it lacks some small features which can be neglected from the point of view of the global deformation of the whole model. This means that one can get the stress and strain fields on the global level but not any fine results from small regions (for example notches or in this case the crack front microstructure). For the purpose of evaluation of these small regions of interest a particular area of the global model is subsequently modeled again with much finer FE mesh and all needed geometrical details (this new, smaller model is called the submodel). As boundary conditions a displacement field from results of the global model is interpolated on boundary nodes of the submodel.
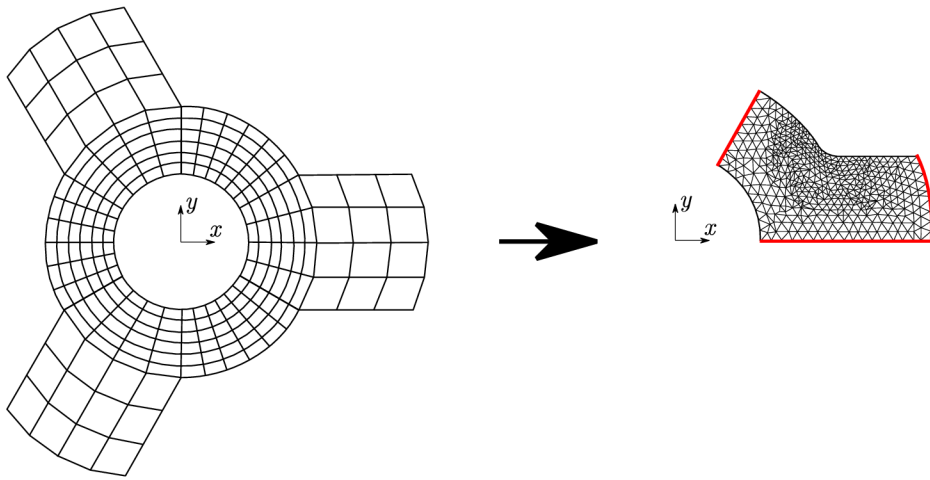
Fig. 23: Example of submodelling (the global model on the left and the submodel on the right side, red line represents the submodel boundaries) [18]

Suitable submodel must follow several rules. At first the submodel boundaries must be in a sufficient distance from modeled detail to avoid any impact of geometry changes on the stress-strain fields on the boundaries [18] (for example the submodel boundaries should never cross any geometrical difference between global model and submodel). Then the modeled area (volume) of submodel must coincide with the same area (volume) in the global model in relative position to used global coordinate

system [18]. These two geometrical conditions can be seen in Fig. 23 where an example of fillet submodel is shown. Also, all additional boundary conditions (except on the submodel boundaries) must be the same on both models.
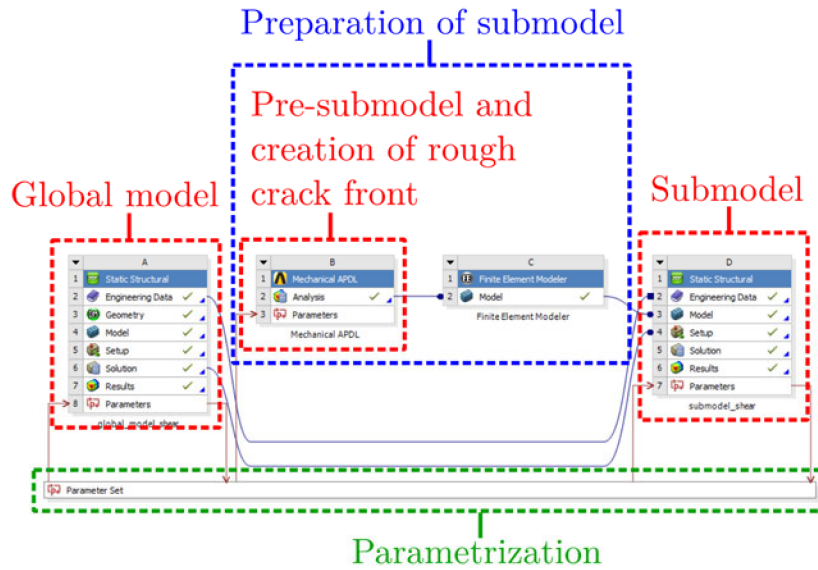
Fig. 24: Workflow of simulations of cylindrical specimen

In all models of cylindrical specimen, the submodelling process was done using the Ansys Workbench inner submodelling procedure. A special model workflow had to be created (Fig. 24). It consisted of both the global model and the submodel and also one intermediate step – the preparation of the submodel where actual geometry of rough crack front was created. All steps were connected via parametrization block, so the basic geometrical changes of the crack asperities could be realized by changing specific values and sub-sequential reruns of the whole simulation.

4.1.1.1 Global model

As was briefly described in chapter 4.1.1, the global model should encompass the whole specimen with all global boundary conditions. In this case the whole cylindrical specimen was modeled with the same dimension as was specified in Fig. 14 (chapter 2.5.2). Actual crack in this model was emanating from the tip of the notch.
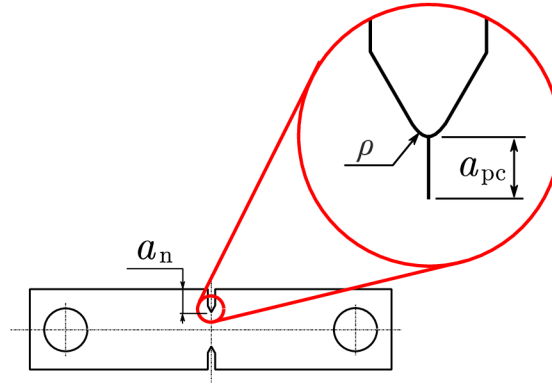
Fig. 25: Detail of the notch root with crack (scheme, cylindrical specimen)

Geometrically the actual crack itself in the model had a length denoted a_{pc} which was the distance between the crack tip and the notch root. It represented real pre-crack in experiments. The total considered crack length consisted of length of the pre-crack a_{pc} and also the depth of used notch a_n so it was $a = a_{pc} + a_n$ (see Fig. 25). In used models of cylindrical specimen, the average precrack length was considered to be 175 μm and the depth of notch was 6.5 mm. The last used dimension (not described in Fig. 14) was the notch root radius ρ which was 150 μm. All these dimension were consistent with the real specimen and the scanning-electron-microscope (SEM) measurements of the crack microstructure [8].
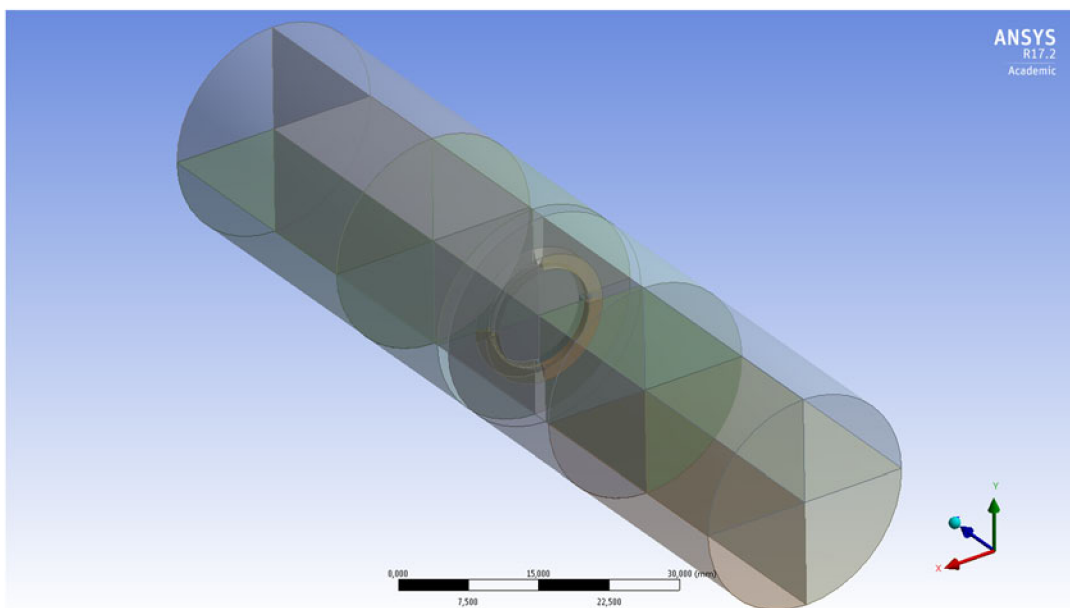
Fig. 26: Modeled geometry of cylindrical specimen

The geometrical model of global model was created exactly according to the dimensions in Fig. 14 and Fig. 25 (with the description of the total crack length) and for better FE meshing of the whole volume it was divided into several subsections (see Fig. 26). The crack itself was modeled as a circumferential planar discontinuity in bulk of the model. No crack front asperities were included in this stage of modelling since on this scale they could not be modeled efficiently.

The geometry was meshed with a rough FE mesh which was sufficient enough to describe deformation of the specimen as a whole, but still it was fine enough to describe displacements of whole specimen. The preciseness of the FE mesh was even more improved by use of the Ansys quadratic 20-nodes mesh element (SOLID186) which uses quadratic base functions to approximate the displacement along its edges [18].
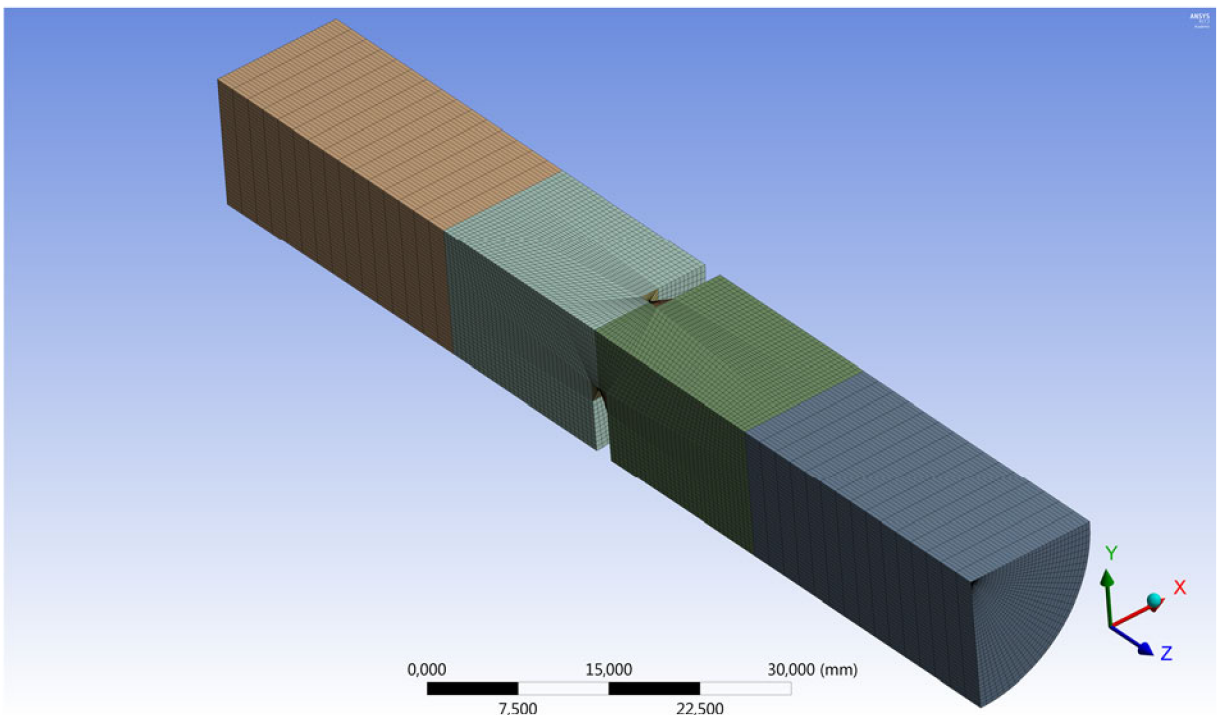
Fig. 27: FE mesh of global model (one quarter of the whole model)

Used FE mesh was shaped on purpose to create uniform distribution of elements throughout the model (Fig. 27). Rougher finite elements were allowed on sides of the specimen where almost rigid movement of clamped sides of the specimen was expected. On the other hand, even that no exact solution around the crack was either expected nor needed, in this stage of modeling the FE mesh was a bit finer in the region of the notch root and the crack to ensure that no error is introduced due to poor mesh quality (even on this modelling stage).

Loading of the model was introduced to mimic the real one. For cylindrical specimen two types of loading schemes were used – torsional loading and pure shear loading.
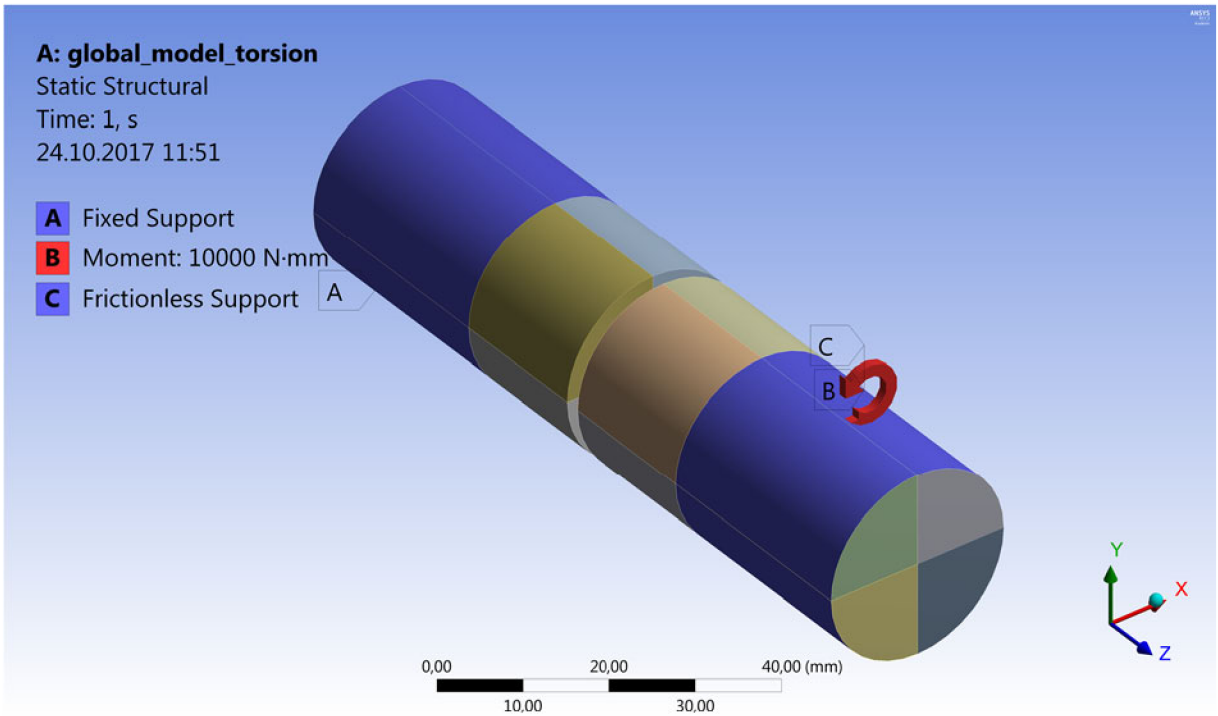
Fig. 28: Torsional loading of global model
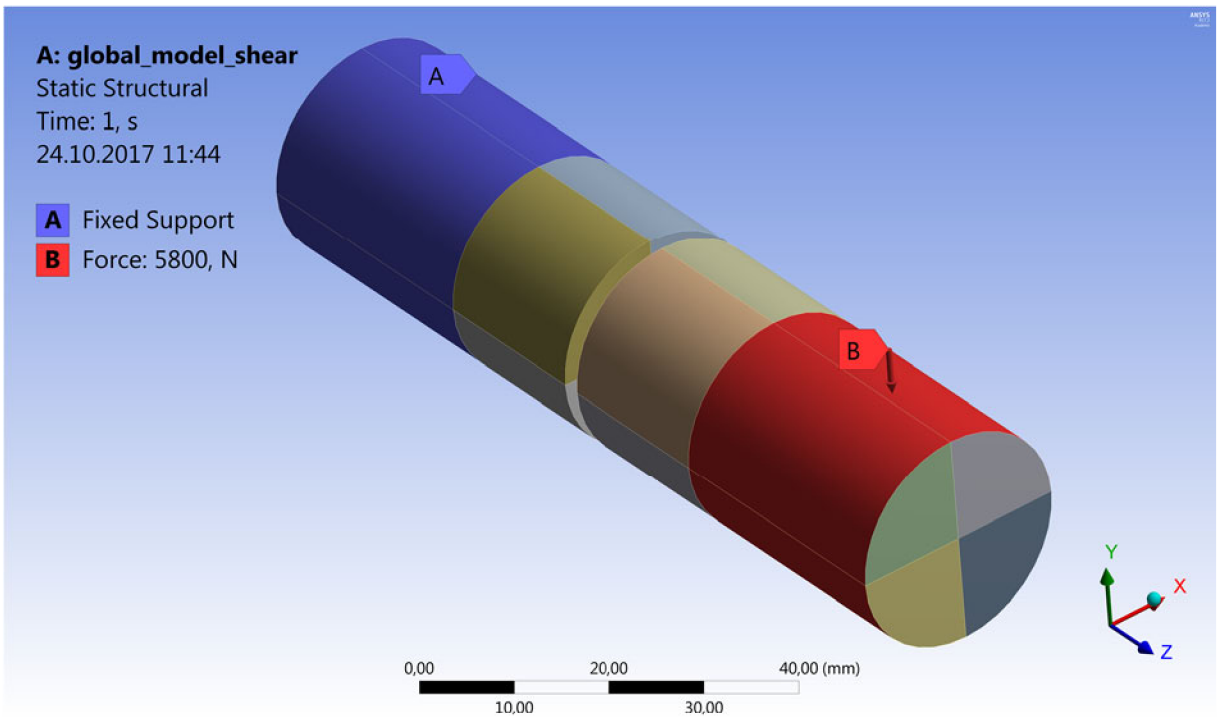
Fig. 29: Pure shear loading of global model

For both loading types one side of specimen was fixed by the "Fixed Support" which restricts movement (displacements) in all direction of affected nodes (surface areas denoted A for both loadings in Fig. 28 and Fig. 29). Fixed area was exactly the same as griped part of the specimen during real experiments and it simulated the real rigid grip. The other side of the specimen was different for each loading type. For torsional

loading a torque moment was introduced (surface area marked B on Fig. 28) with the magnitude of 10 Nm for model with niobium as used material and 16 Nm for model with pure iron as used material model. For shear loading a force was applied (marked B in Fig. 29) in the direction opposite to the y-axis and with magnitude of 3600 N for model with niobium as used material model and 5800 N for model with pure iron as used material model. Actual magnitudes of the loading force and moment are insignificant since linear elastic simulations were used (observed SIFs are linearly dependent on loading and results were always normalized to loading, see following chapters) but they were chosen to copy the conditions during the experiments for measurement of the threshold values of SIFs and other related research done by Vojtek et al. (e.g. [8, 36, 56]) for used materials.

Except the loading momentum or force, the second side of specimen was also treated with one additional boundary condition. For torsional loading the "Frictionless Support" was applied to the whole circumference of gripped part of the specimen. This meant that any displacement in radial direction of the cylinder was suspended and thus the gripped part of the specimen only rotated (from global point of view). For the shear loading the same area with force loading was needed to move as a rigid body in the direction of force loading (to simulate rigid behavior of the clamping device). This was achieved by applying coupling constraint [18] to all gripped nodes. By applying the CP function all selected nodes were coupled to have the same absolute displacement in selected direction. This constraint denied the model to bend along the grip and thus no unwanted loading (e.g. mode I loading along the crack front) was present.

The last input for this stage of simulation was the material model. Only linear elastic, isotropic behavior of the model was considered, and the linear constants were used in conjunction with the experiments done by Vojtek et al. (e.g. [8, 36, 56], as mentioned before) which were done on niobium and pure ARMCO iron. For niobium the Young's modulus $E = 105$ GPa and shear modulus $E_{\text{shear}} = 38$ GPa and for pure iron the moduli were $E = 211$ GPa and $E_{\text{shear}} = 82$ GPa. Because only isotropic elasticity was considered, the other material elastic constants were only dependent on E and E_{shear} and can be easily calculated from them (for these basic relations see e.g. [57–59]).

When all inputs were introduced, whole simulation of the global model could be solved. Since there were no micro-changes in crack geometry, this model was calculated only once per loading regime and material model and the results from these four models were used as an input for subsequent submodelling.
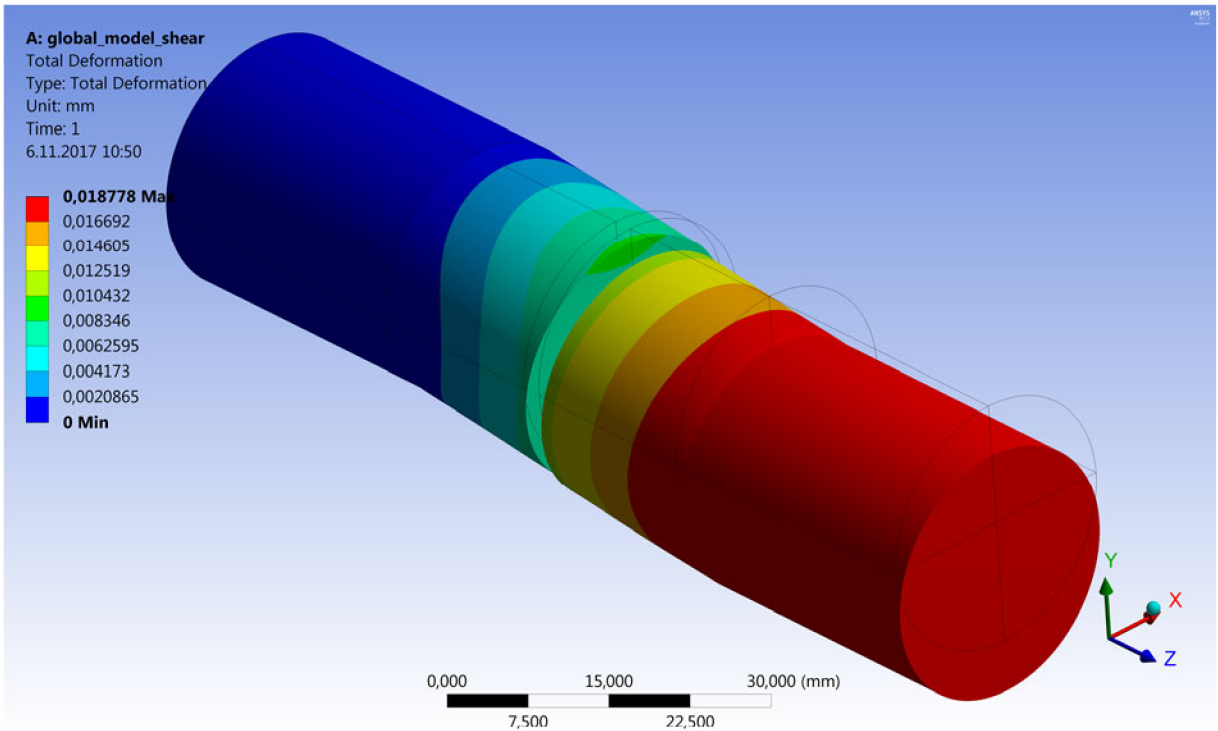
Fig. 30: Total deformation of global model (pure shear loading, F = 5800 N, ARMCO iron), depicted deformation is exaggerated to show the difference between deformed model and undeformed wireframe

Although the global model was not fine enough to describe the stress-strain fields around the crack tip, it was good enough to solve overall deformation of the specimen (example of deformation of pure shear specimen is in Fig. 30). The specimen deformation was in all cases consensual with expectations (pure shear or torsional loading).

4.1.1.2 Preparation of submodel

In general, the submodel consists in many cases only from a small part of the global model which is modeled with much finer FE mesh. In other cases, there are some minor alterations in overall geometry or composition of the model in submodelling part (for example chamfers or fillet-like geometry e.g. [60, 61] or added small structures [62]). In this simulation of complicated crack geometry, the submodel introduces better FE mesh and also a tortuosity of the crack front which is different from simple circumferential line used as the crack front in the global model.
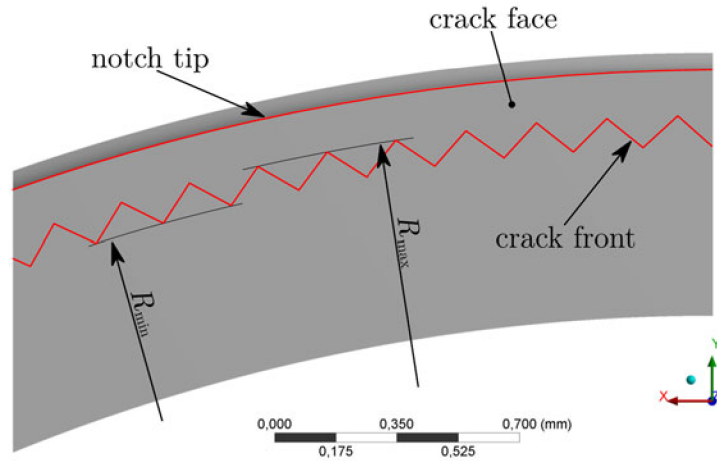
Fig. 31: Schematic of crack front fine shape

For all simulations made on the cylindrical specimen the crack front tortuosity was modeled according to Fig. 31. Crack front was shaped as a uniform zig-zag line alteration and thus it formed teeth-like formation. The crack front was still in one plane and no 3-dimensionality of crack front or flanks was allowed.

Using Ansys APDL code [18] "teeth tips" were created as keypoints at angular distance corresponding to 200 µm between upper tips (thus 100 µm between alternating keypoints) and in radial distance from the center of specimen cylinder alternating between R_{min} and R_{max} (see Fig. 31). The minimal and maximal radiuses were dimensioned to form desired height of teeth (difference between R_{max} and R_{min}) and the mean value of used radiuses (crack tip mid-line) was always the same as overall crack length used in global model (see chapter 4.1.1.1 and Fig. 25). By connecting these points by lines, a crack front was formed geometrically. This jagged line was used to set bounds of crack faces in a toroidal cutout from the global model. Created toroidal model was actually formed from two parts divided by the crack plane where the crack faces were created as two unique faces for both sides at the same location, thus creating the crack flanks.

This procedure created geometrical model of submodel with jagged crack front. The parametrization block (see Fig. 24) provided input parameters in form of teeth height and distance between teeth tips.

4.1.1.3 Submodel

Geometrical model with zig-zag shaped crack front created using APDL commands
(see chapter 4.1.1.2) was used as a template for actual submodel.
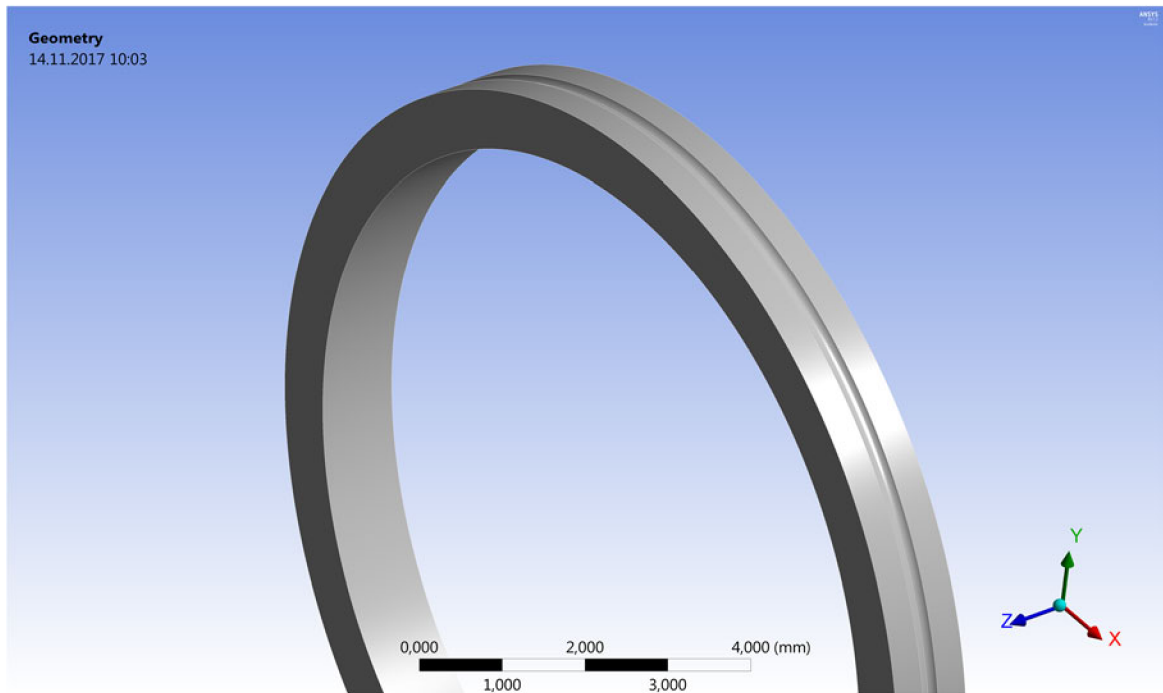
Fig. 32: Geometry of submodel

Geometrically the submodel was a simple toroidal ring (see Fig. 32) encompassing
an area of the notch root and the crack with serrated tip. This model allowed to minimize
the meshed volume but still with enough space around the crack to fulfill the
submodelling conditions [18].

The geometrical model was meshed with quadratic SOLID186 Ansys mesh
elements [18].
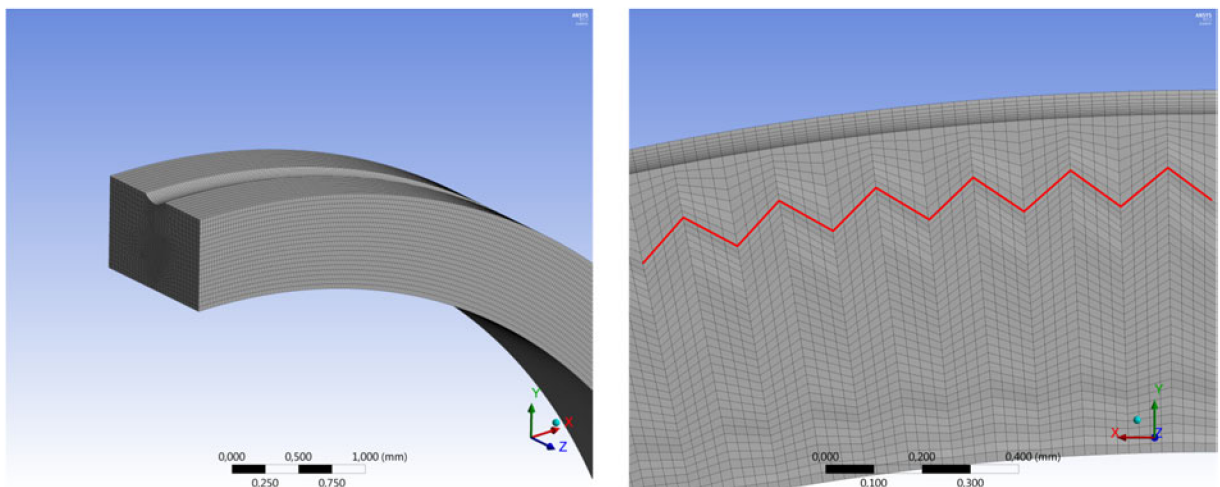
*Fig. 33: FE mesh of submodel (left, submodel ring with showed cross-section) and detail
of mesh spacing along the crack front (right, red line represents crack front)*

The submodel was meshed with fine FE mesh which was refined in area close to the crack front (see Fig. 33 (left)). Number of used elements was optimized to yield sufficiently precise results but at a low cost of calculation time and hardware consumption. Even with this in mind, used 3D model resulted in almost 2 million of mesh elements (approximately 7 millions of evaluation nodes) which was on the edge of computational capabilities of used workstation.

This mesh was also built for good evaluation of the SIFs. Along each tooth serration four mesh elements were used (see Fig. 33 (right)). Because the quadratic elements with mid-side nodes were employed, nine evaluation points along each tooth side were available for numerical calculation of the SIFs (according to method described in chapter 2.4).
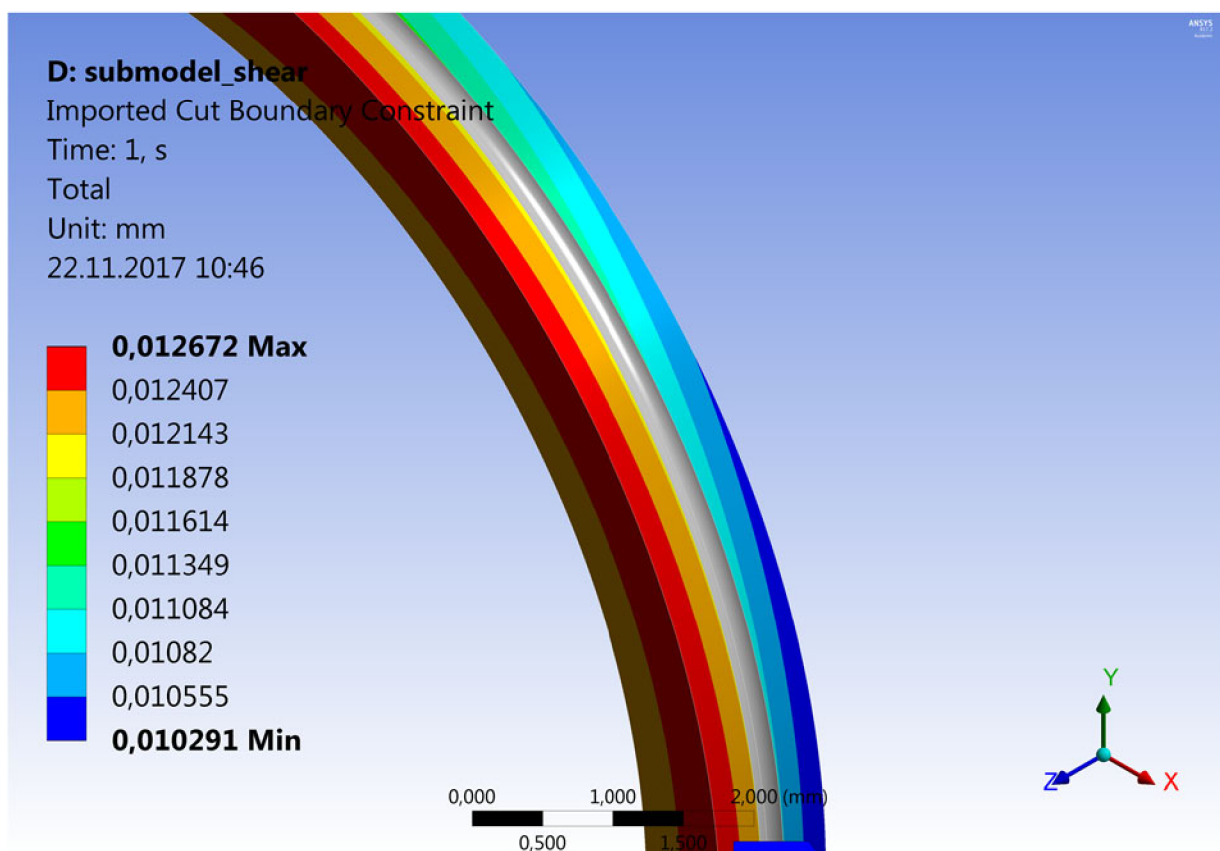
Fig. 34: Example of imported boundary constraints (shear specimen)

The submodel boundary conditions were applied according to the Ansys submodelling procedure guidelines [18]. All faces of the submodel which were used as cut boundaries (in the cylindrical specimen model all outer faces except notch root radius were used) were appointed for submodelling in the Ansys Workbench Mechanical window. When the submodel was connected with results from the global model in simulation project overview (Fig. 24), the preprocessor in the submodel simulation loaded results from the global model and it automatically made interpolation of displacements from the global model to nodes at the cut boundaries on the submodel (Fig. 34).

D: submodel_shear
Equivalent Stress 2
Type: Equivalent (von-Mises) Stress
Unit: MPa
Time: 1
22.11.2017 10:34

469,25 Max
417,9
366,56
315,22
263,88
212,54
161,19
109,85
58,509
7,1669 Min
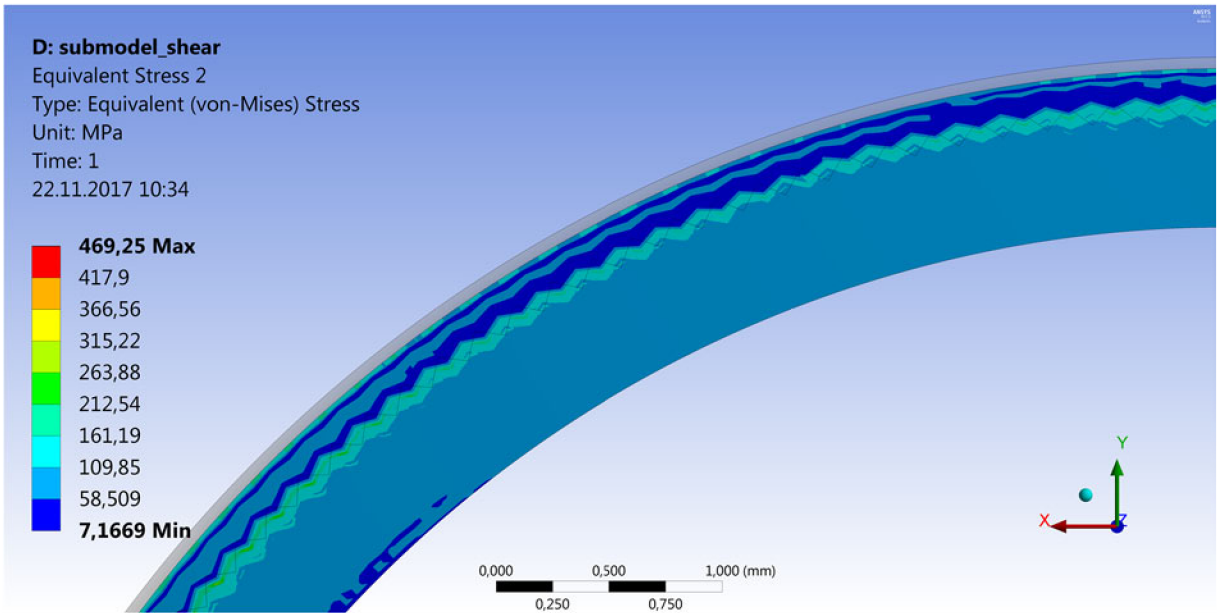
Fig. 35: Example of resulting equivalent (von-Mises) stress in submodel (shear specimen, place of mixed-mode II+III loading)

Results obtained from the submodel simulations of the cylindrical specimen fulfilled the expectations. The stress-strain singularity at the crack tip seemed to be described sufficiently with used FE mesh and resulting stresses for alternating crack front geometry (Fig. 35) showed changes along each serration. The maximum equivalent (von-Mises) stress was for shear specimen in place where pure mode III loading was present which was in good agreement with previous researches (for example [40, 63, 64]). Moreover, results of the model with torsional loading showed ideal rotational symmetry as was expected because of the same symmetry of geometry and loading.

Besides the stress-strain fields SIFs were also calculated for all variants of models. These variants included mentioned two types of loading (torsion and shear) and two material models (ARMCO iron and niobium, according to Vojtek et al., e.g. [8, 36, 56]) with respect to the absolute values of loading momentum and force which were different for both material models (as mentioned in the chapter 4.1.1.1). Despite the fact that the different linear elastic material properties of two used materials should not change the absolute values of SIFs (they are independent on the Young's modulus and the Poisson's ratio), due to different values of loading momentums and forces the differences between SIFs for ARMCO iron and niobium were expected.

In general, the resulting fracture parameters were obtained for models with various roughnesses of crack front and also for models with straight crack front for verification of used models and methods and also for further results processing.
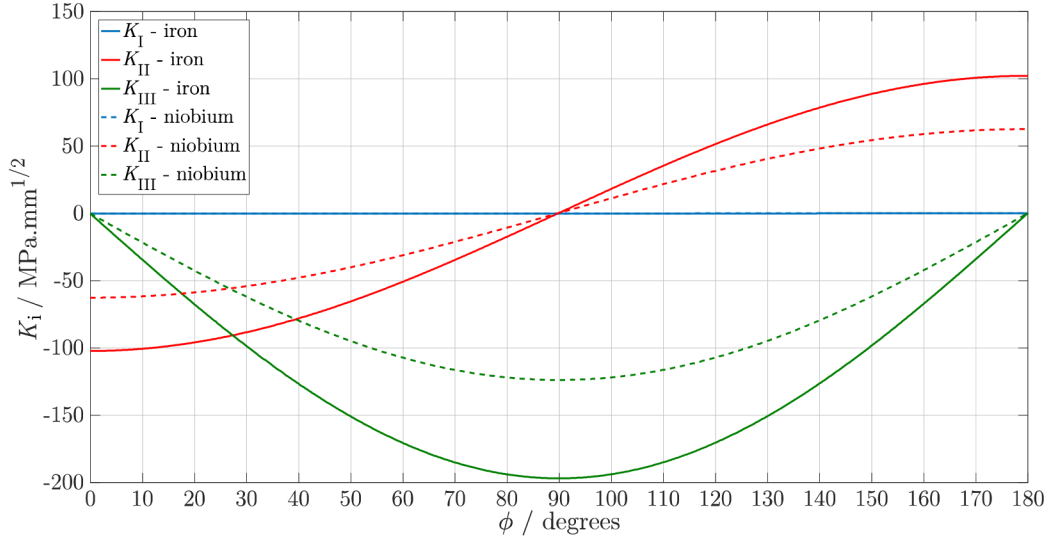
Fig. 36: Resulting SIFs (raw data) for cylindrical specimen with straight crack front loaded by pure shear
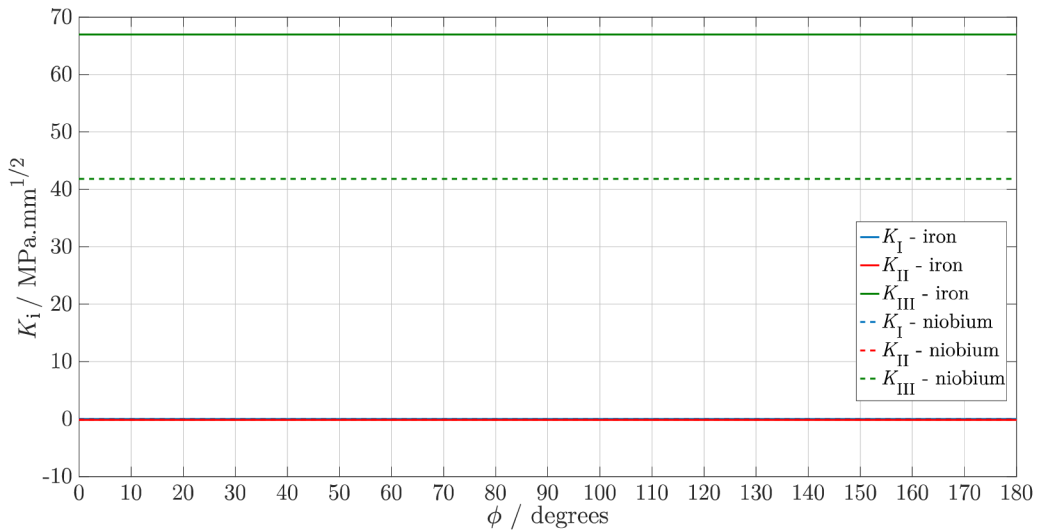
Fig. 37: Resulting SIFs (raw data) for cylindrical specimen with straight crack front loaded by torsion

Resulting SIFs for models with the straight crack front loaded by pure shear (Fig. 36) and loaded by torsion (Fig. 37) are depicted as a function of angle coordinate ϕ (the same as depicted in Fig. 17 - left) where 0° and 180° is for the top and the bottom of the specimen respectively and 90° is for the side of the specimen. Depicted results are only for half of the specimen (for ϕ from 0° to 180°).

It is clearly visible that for both specimens the resulting SIFs from simulations with ARMCO iron as a material model are higher values than the ones where niobium was set as the material model. This is not due to mismatch between materials, but it is caused by different amplitudes of loading used for different material models

(SIFs are only functions of the geometry and loading, see chapter 2.1) and this phenomenon was expected.

Results for the shear specimen (Fig. 36) show strong dependence of K_{II} and K_{III} on the angular position ϕ around the specimen and that mode I SIF is literally zero along the whole crack front due to pure shear loading. At the top and bottom of the specimen there is a spot where pure mode II loading is present and on the sides of the specimen there is a place with pure mode III loading. All other parts of the crack front are under mixed mode loading which was expected (see chapter 2.5.2.2). This is also in very good agreement with our previous research [40, 64], where it was proved that for the cylindrical specimen under remote shear loading the K_{II} is a cosine function of angular position ϕ and K_{III} is a sinus function of ϕ:

$$K_{II}\left(\phi\right) = K_{II}\left(\phi = 0°\right) \cdot \cos\left(\phi\right),$$

$$K_{III}\left(\phi\right) = K_{II}\left(\phi = 90°\right) \cdot \sin\left(\phi\right). \tag{26}$$

Present results for shear specimen (Fig. 36) follow these functions (26) very well.

Results of the specimen loaded by torsion show, again in good agreement with expectations, that for this type of specimen and loading only pure mode III loading is present along the whole crack front and modes I and II diminished.

Results obtained from calculations with the rough crack front differ for each crack front configuration and they are discussed in following chapters.

4.1.2 Researched variants (cylindrical specimen)

As was mentioned above, the crack front tortuosity in models of cylindrical specimen was considered to be only in-plane, no out-of-plane roughness or kinking of the crack front was allowed. Aside this constriction, it was decided that only uniform crack front asperities will be included in these models.

Within the frame of these constrictions two types of models were investigated. The first one aimed at description of simplification possibilities of these models and the second one was more closely connected to the research aimed at shear mode fatigue crack propagation and the influence of the crack front microstructure on crack propagation.

4.1.2.1 Possible model simplification

Finite element models of specimens with cracks with complicated crack front geometry require finer mesh discretization due to constantly changing crack front and therefore, numerous unpredictable changes in stress-strain field around crack front. The use of this complicated FE mesh and the fact that such simulations must be almost always modeled as 3D models makes simulations of fractures (which are complicated on their own) even more hardware- and time-consuming. This fact makes any valid simplification of such model a very valuable step in simulations of such cracks. Research on this problem was published by the author of this thesis in [65] and some of the presented results were already shown in that paper.

Besides standard steps for efficient modelling (for example submodelling, efficient FE mesh sizing etc.) a geometry simplification was considered while modelling the cylindrical specimen. Since overall crack front geometry was even, and crack front asperities oscillated around one mean crack length, the simplification in terms of modelling only one particular part of the crack front (area of interest) with geometrical asperities and the rest simplified was one option to decrease calculation time and hardware severity. So, the basic premise of this type of model simplification was to model only a small area of interest with representative crack front asperities and the rest of the crack front could be simplified and thus meshed with coarse FE mesh.

To get quantitative description of usability of neglecting the crack front microstructure in some parts of model the FEM simulation of cylindrical specimen with shear loading was used (chapters 4.1.1.1 - 4.1.1.3). The main idea was to compare the resulting SIFs in areas of interest obtained from model where full crack front was modelled with zig-zag asperities with model which had only some number of crack front teeth around the area of interest.
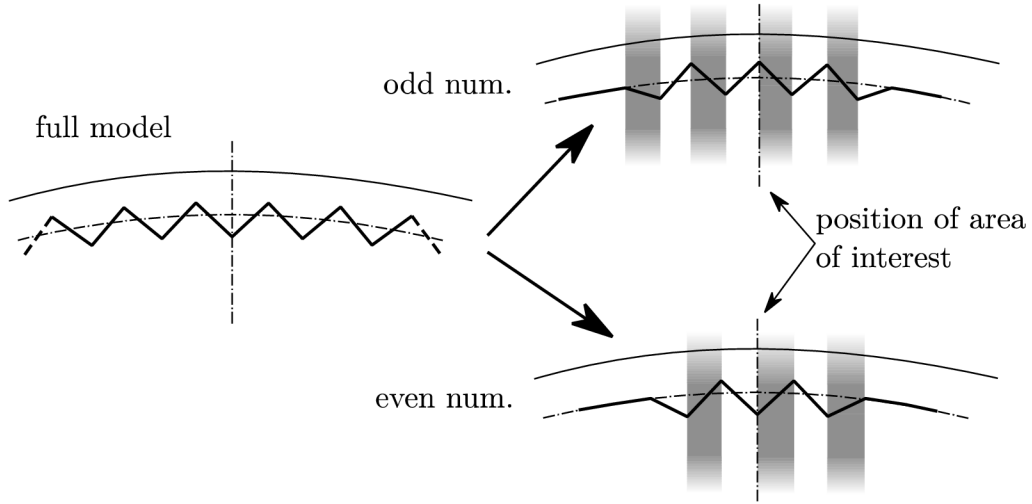
Fig. 38: Scheme of full and simplified models (two variants)

The difference between full and simplified models can be seen in Fig. 38 where two types of simplified models are shown. Since the number of modeled teeth around the area of interest was one variable for modelling and the symmetry of the model was needed to be preserved the simplified model had to be divided into two groups – one with odd number of teeth and the second with even number of teeth. Each simplified model was compared with corresponding full model with the same characteristic dimensions of teeth.

Observed results were the local SIFs values along the crack front. Because both model types in this study contained crack front asperities it was obvious that the SIFs values should differ from ones obtained for smooth crack front (see Fig. 36).
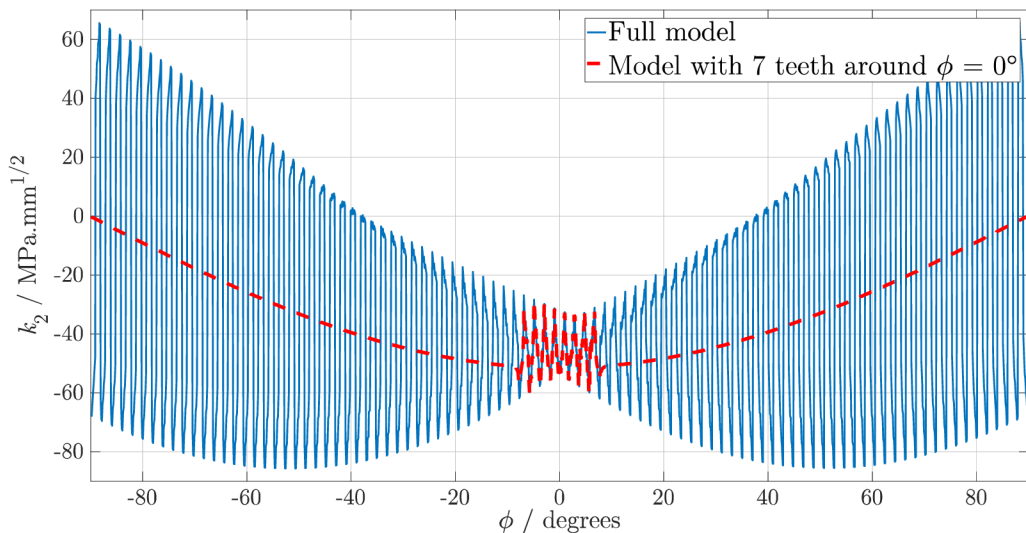
Fig. 39: Oscillation of local mode II SIF along the crack fronts of full and simplified models (example)
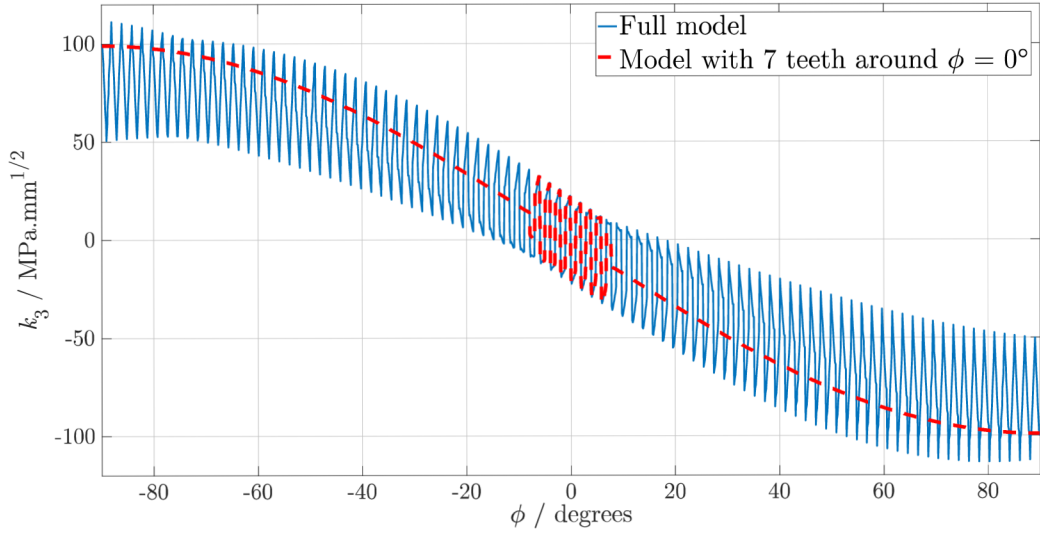
Fig. 40: Oscillation of local mode III SIF along the crack fronts of full and simplified models (example)

Because of negligibility of mode I SIF only local k_2 and k_3 values were observed (examples of results are on Fig. 39 and Fig. 40 respectively). Local values of k_2 and k_3 show similar mean progressions as global ones (Fig. 36) but the results for rough crack oscillates a bit due to zig-zag geometry of crack front. This also means that even in places where there were pure modes II or III on the specimen with straight crack front (see Fig. 36) for the specimen with rough crack local induced modes creates local modes mixity. These oscillation patterns are quite similar for both model types in area of interest, but they obviously differ in areas where is the simplified crack front (in the model with less teeth).

To quantitatively describe the difference between full and simplified model the relative difference δk_i was calculated as follows:

$$\delta k_i = \frac{\left| k_{i,\,full}\left(\phi\right) - k_{i,\,simple}\left(\phi\right)\right|}{k_{i,\,full}\left(\phi\right)} \cdot 100\%, \tag{27}$$

where $k_{i,\,full}(\phi)$ and $k_{i,\,simple}(\phi)$ are the respective values of local SIFs in modes i = 2 or 3. The difference was calculated for both modes with use of several numbers of teeth in simplified model ($n = 1 \div 7$; each simulations had beside the n number of teeth one half-tooth on each side to create a transition to smooth crack front – see **Fig. 38** right side) and for location of global pure mode II loading ($\phi = 0°$) and pure mode III loading ($\phi = 90°$).

40
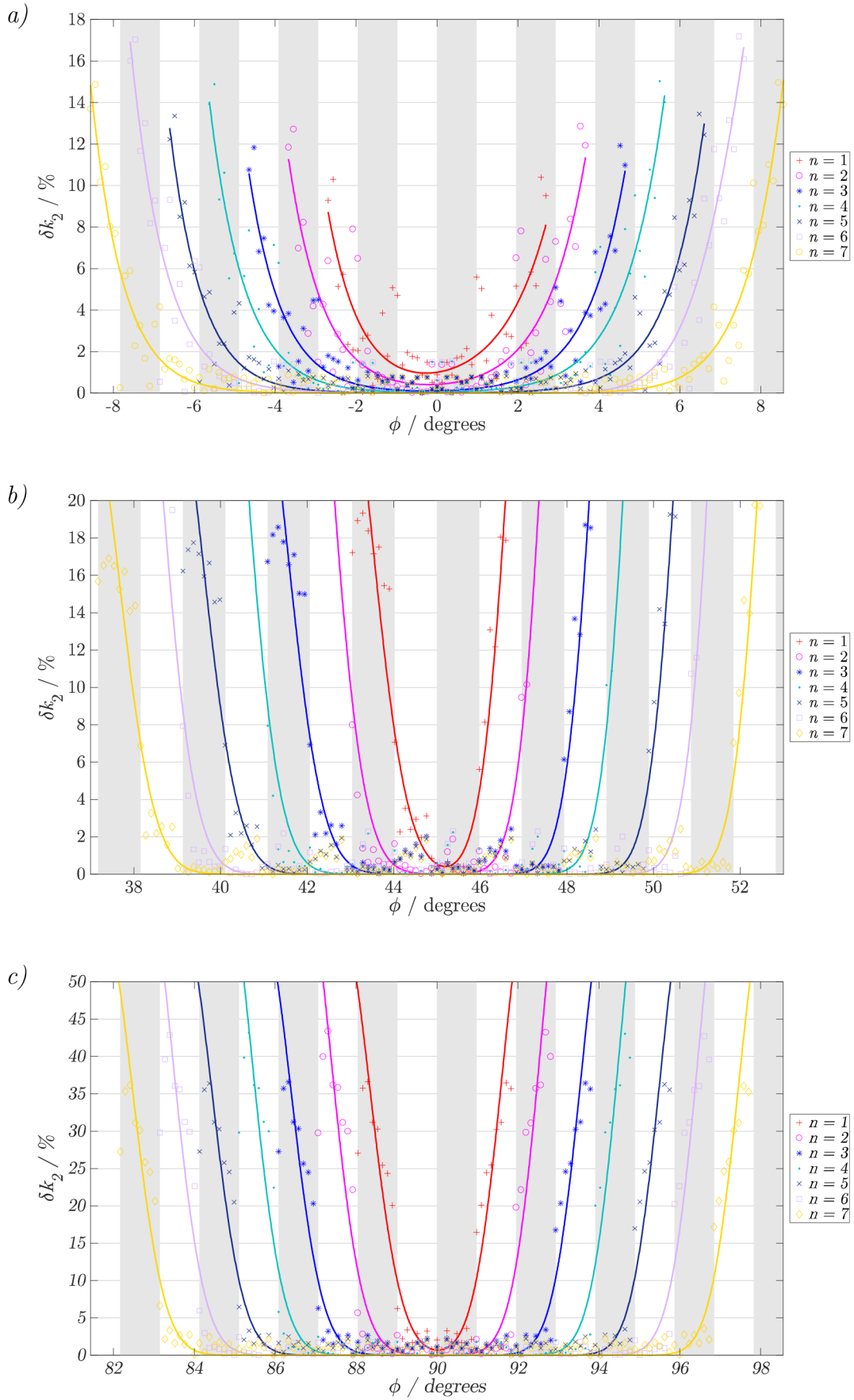
Fig. 41: Resulting δk₂ for area of interest in: a) 0˚, b) 45˚ and c) 90˚
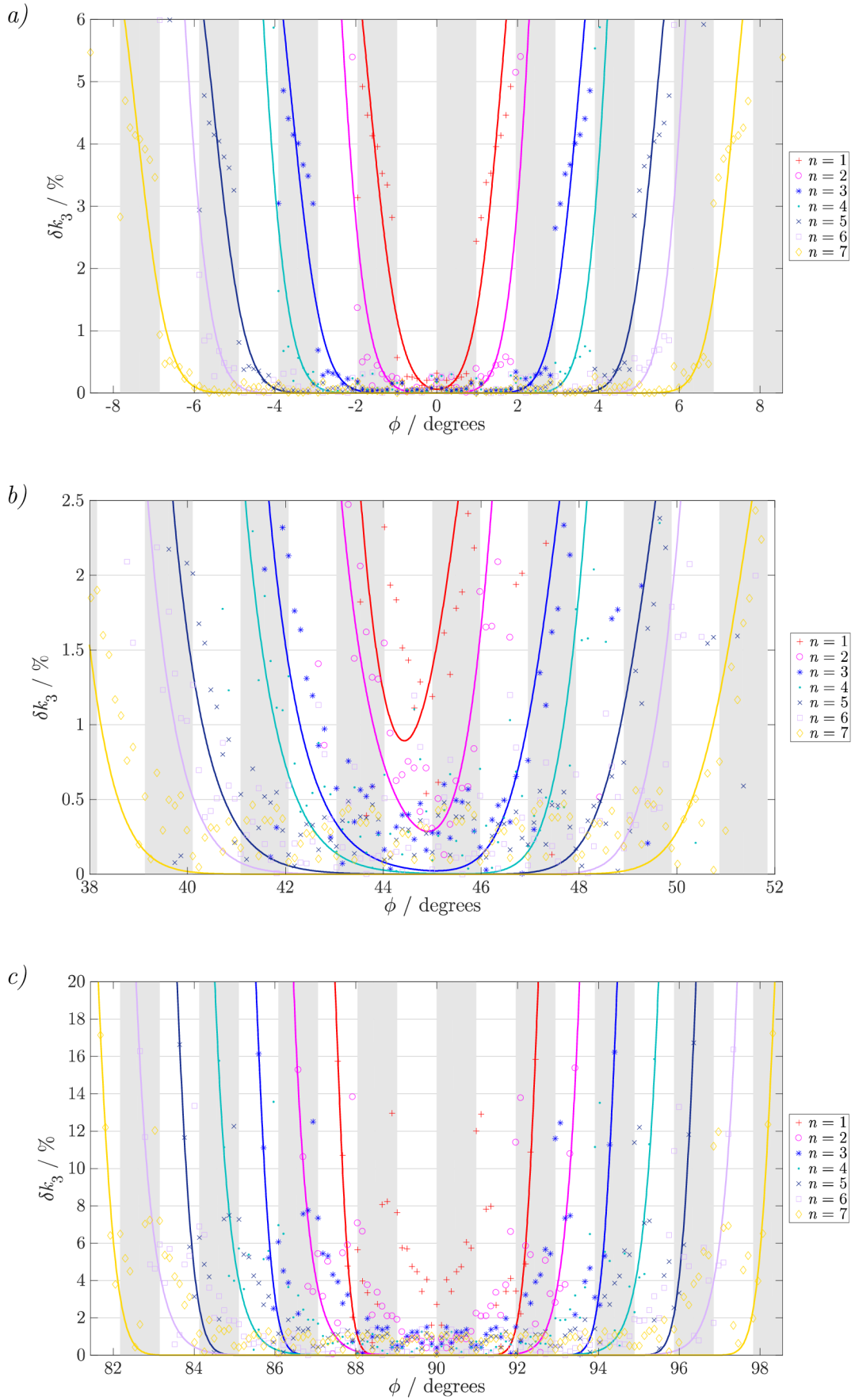
Fig. 42: Resulting δk₃ for area of interest in: a) 0°, b) 45° and c) 90°

Resulting relative differences for local mode II (Fig. 41) and mode III (Fig. 42) SIFs are depicted with zebra-like gray pattern. Each gray or white strip corresponds to one facet on the crack front (one half of tooth, one gray and one white strip combination forms one tooth, the zebra-like pattern corresponds to one depicted in Fig. 38).

It is obvious that for both k_2 and k_3 results and for all investigated areas of interests the simplified model with $n = 1$ gives unacceptable difference between full and simplified models even for modeled tooth. Results from models with larger n show more acceptable difference lower than 1%.

Closer look on results for $n > 2$ suggests that core teeth (for example for $n = 4$ core teeth are the second and the third ones etc.) give very accurate, almost identical results as full model and the side teeth facets and the transition facets show difference increasing with the distance from center of area of interest.

The sum of presented results confirms that, for the investigated types of serrated crack fronts and loading, the local SIFs are influenced only by the close surroundings of investigated area. To get results identical with those obtained for the continuously serrated crack front, only a small portion of the serrated crack front (in the area of interest) is needed to be modeled and the rest can be simplified (replaced by smooth, averaged crack front). The lowest undisrupted area corresponds to that in between the two regular teeth framed on sides by the transition asperities, excluding these two side teeth – the lowest n should be 3 for case where only one tooth is investigated. This means that the fine mesh in the FE modeler can be assigned only to such a small region at the serrated crack front and the rest of the specimen can be meshed in a much coarser manner. This simplification leads to faster calculation times and less hardware-demanding simulations.

4.1.2.2 Zig-zag crack front - mode III crack propagation

Description of micro-mechanisms of crack propagation under remote mode III loading is rather difficult. There have been some attempts to describe this type of crack propagation qualitatively (by observation of fractographical patterns) but more quantitative approach was used only in recent years by Vojtek et al. [66] with use of numerical simulations. These simulations in [66] were created by the author of this thesis and they are presented in this chapter.
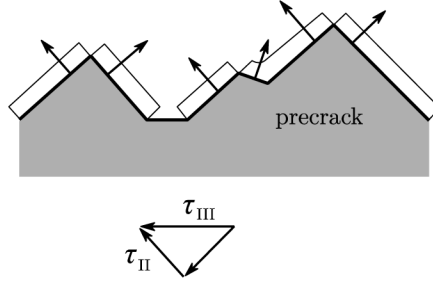
Fig. 43: Local mode II crack advances for remote mode III loading

From fractographical studies it was deduced that serrated crack front under remote mode III loading exhibits local mode II crack propagation (Fig. 43) due to geometrically induced local mode II loading. This was observable especially for materials with coplanar shear mode crack growth (BCC metals). This type of microstructural geometry of crack front was modeled with use of FE model described in the chapter 4.1.1 where local mode II loading was compared with global mode III loading of the cylindrical specimen.
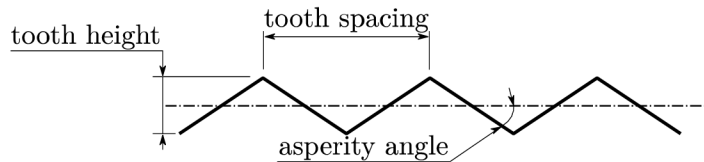
Fig. 44: Schema of crack front asperities

The FE model was in this case adapted to simulate different crack teeth (asperities) angles. The spacing between crack front teeth was set fixed at 200 μm and the tooth height was changing from 5 μm to 65 μm. These values were adjusted by scripted function to ensure that the number of teeth is a whole number around the circumference of specimen. The results were then parsed by the asperity angles which were calculated from actual teeth dimensions and ranged from 3.35° to 41.65°.

Resulting SIFs were evaluated at 9 points along each tooth serration where the last one evaluation node of one tooth face was also the first one of the next tooth face. To describe the influence of local mode II inducement for remote mode III loading a ratio of local k_2 to remote K_{III} was investigated on both torsional and pure shear loaded specimens (for shear specimen a place with global mode III loading around $\phi = 90°$ was investigated) and for both material models – ARMCO iron and niobium.
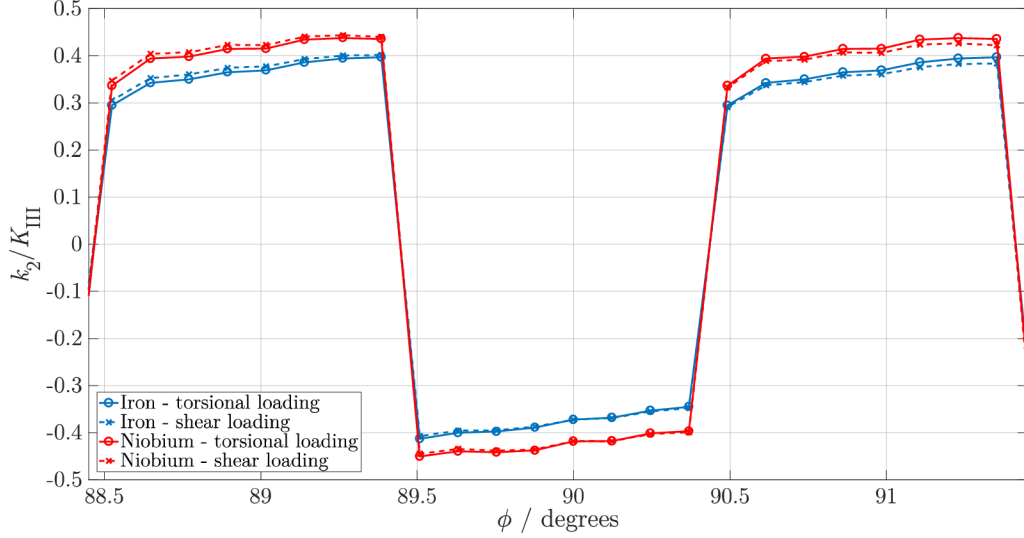
Fig. 45: Example of resulting ratio k_2/K_{III} for serrations with asperity angle 17.19°

Resulting ratio k_2/K_{III} (Fig. 45) is very consistent for both loading types if one take into account that pure mode III loading on the shear specimen is present only very close to $\phi = 90°$. Both material models give qualitatively the same results of locally induced mode II SIF but there is a very small difference between them. Since SIFs does not depend on the Young's modulus of used material model (see chapter 2.1), there should be no difference. However, closer look to calculations, paper [6] and our previous work [64] showed that actual local mode II inducement is dependent on Poisson's ratio of used material model. From Young's and shear moduli (E and E_{shear} respectively) for linear elastic, isotropic type of material model actual Poisson's ratio μ can be obtained:

$$\mu = \frac{E}{2E_{\text{shear}}} - 1. \tag{28}$$

Since the Young's and shear moduli of material models used in presented simulation were known (see chapter 4.1.1.1), the Poisson's ratio for niobium is 0.38 and for ARMCO iron it is 0.29 (according to formula (28)). This difference influences the lateral contraction of material and therefore local inducement of mode II SIF is slightly different for both models. This difference increases with larger crack front asperities and it vanishes for a straight crack. Since both model types were treated separately, there will be no other comparison between them.

Actual observed results were at location of remote mode III loading at one crack front tooth facet. As was mentioned before, on one facet there were 9 evaluation nodes to obtain local SIFs.

45
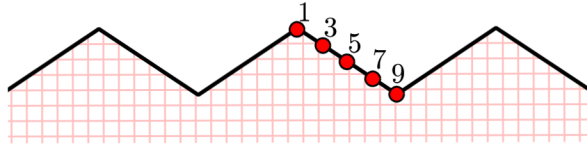
Fig. 46: Positions and numbering of evaluation nodes along the crack front serration (only odd numbers are shown)

Evaluation points were distributed evenly between the tooth peak and valley where node No. 1 is situated in a place with smallest overall crack length (tooth peak) and node No. 9 is in the place with largest crack length (tooth valley) – see Fig. 46, area with red lines pattern represents un-cracked material and area above zig-zag line represents the crack faces.
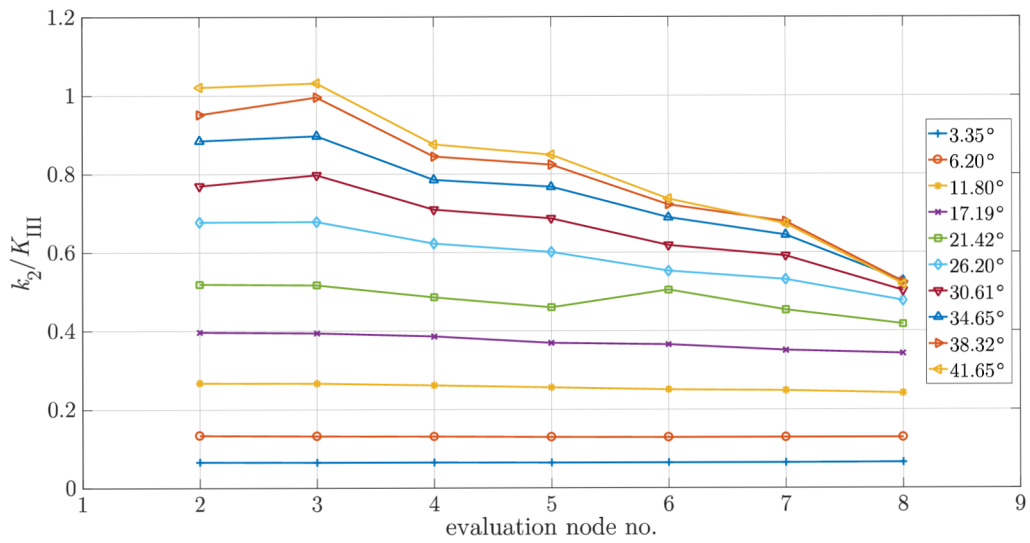
Fig. 47: Resulting k₂/KIII for one tooth facet - iron material model
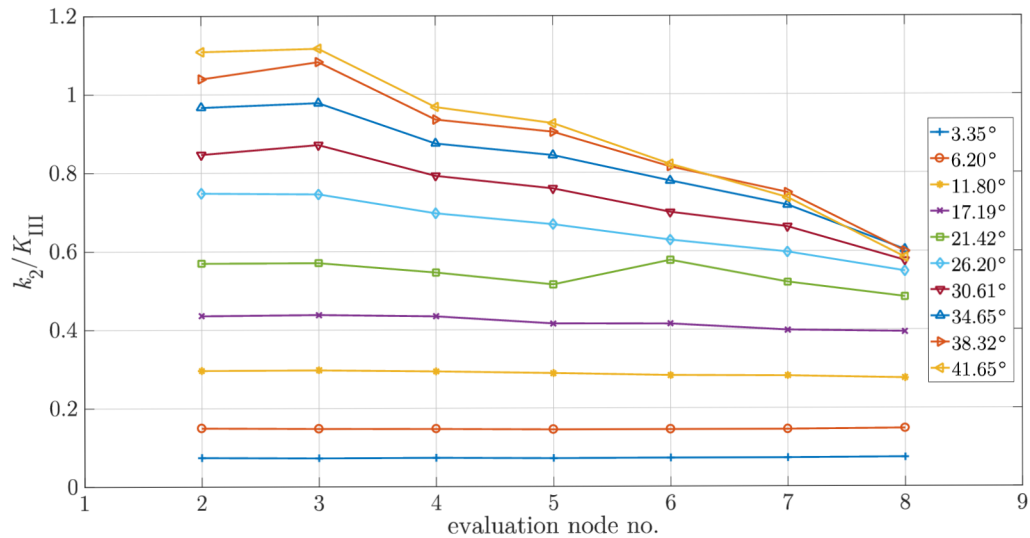
Fig. 48: Resulting k₂/KIII for one tooth facet - niobium material model

Evaluated ratios of k_2/K_{III} along one tooth facet in charts above (Fig. 47 for ARMCO iron and Fig. 48 for niobium) are depicted as functions of numbering evaluation nodes along one tooth facet (see Fig. 46) for all different asperity angles. Nodes number 1 and 9 are excluded since they are on the edge of the asperity and during the computation of SIFs exact direction of the crack could not been deduced for proper numerical evaluation of the local values of SIFs (see chapter 2.4).

A slight shift between two material models is obvious if both charts are compared and it complements the difference found in Fig. 45. This difference is increasing with larger asperity angles and it vanishes when only straight crack is assumed. As was mentioned above this difference points towards the explanation that different Poisson's ratio and thus different lateral contraction of material changes the mode II inducement if the crack is under remote mode III loading.

The second thing visible in charts above is that for small asperities (from used datasets with teeth angles 3.35°, 6.20° and 11.80°) the local component of induced mode II loading is constant along the whole tooth facet. But for larger asperity angles the k_2 component tends to increase in area of the tooth peak (evaluation node No. 1, place with the smallest total crack length). It seems that the stress concentration at this spot and the loading of tooth peak is higher than in other areas of the crack front and thus the crack propagation should start there instead of different place along the crack front asperity.

The last but most obvious and expectable qualitative result is that with higher asperity angle the local mode II SIF increases.

For comparison of experimentally measured threshold values of mode II and III SIFs with numerical results a maximal value of ratio k_2/K_{III} was evaluated for both materials and all used asperity angles. Moreover, to demonstrate the overall state of the mode II inducement an averaged value (through one facet) was calculated too.
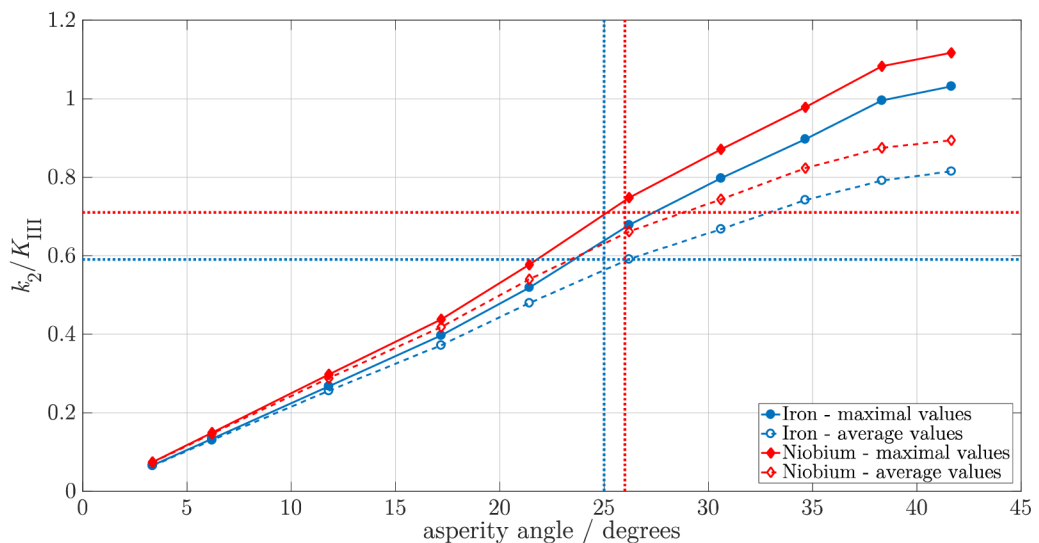
Fig. 49: Maximal and averaged values of ratio k_2/K_{III}

Resulting maximal and averaged values of the ratio k_2/K_{III} (Fig. 49) are complemented by the dotted lines which represent experimentally measured threshold ratios $\Delta k_{2,\text{ eff th}}/\Delta K_{\text{III, eff th}}$ and mean asperity angles for used materials obtained from fractography images (blue dotted lines for ARMCO iron and red dotted lines for niobium). Measured ratios of effective mode II and mode III thresholds and mean asperity angles are 0.59 and 25° respectively for ARMCO iron and 0.71 and 26° respectively for niobium [56, 67, 68]. Point in which each of the two types of dotted lines cross represents experimental equivalent to numerically modeled results.

Comparison of experimentally measured angles and effective threshold ratios with numerical models show a very good agreement. It showed that even with relatively small asperity angles at the in-plane pre-crack front the local induced mode II loading (and hence mode II crack propagation mechanisms) can contribute to propagation of crack under remote mode III loading. Therefore, this numerical model helped with quantitative description of mode III crack propagation assisted by mode II mechanism.

4.2 CTS specimen

As a second template for numerical modeling the CTS specimen was used. Actual model was created in accordance with work of Li et al. [33, 34] (as described in chapter 2.5.1).

The CTS specimen was chosen because it is widely used in experiments related to the remote mode II loading and obtained results can be easily compared with research conducted by other authors. Also, the use of its relatively simple geometry is suitable for this type of research. At last when the CTS specimen is used, it can be easily adjusted for mixed mode I+II loading [31–34].

4.2.1 Numerical model

To create a numerical model of experiment the Ansys software was used (the same as for cylindrical specimen, see chapter 4.1 and its subchapters). The general idea was to create a numerical model which can evaluate SIFs functions along the crack front for both standard model of fractured specimen and also for specimen with tortuous crack front and flanks. To achieve this, whole modeling process (and Ansys project hierarchy) had to be divided into several sub-steps, each one containing the critical part of the solution process.
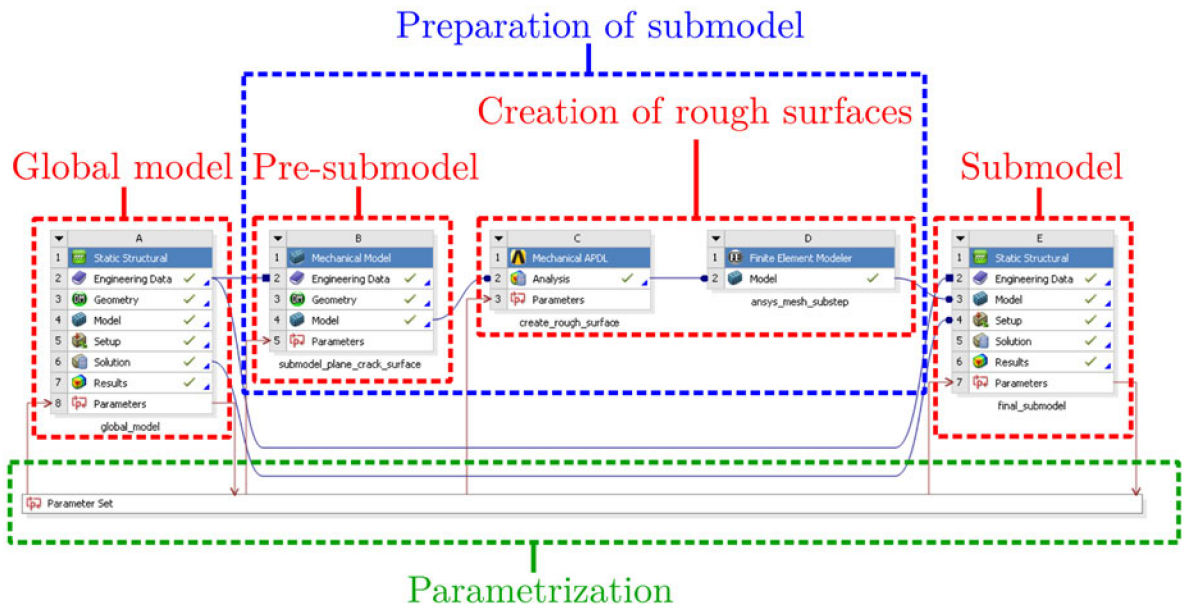
Fig. 50: Workflow of simulations of CTS specimen

It is obvious that for the CTS specimen a much more complex simulation structure (Fig. 50) than for cylindrical specimen (Fig. 24) was used. Both methods – submodelling and APDL programing with full parametrization – were used in this type of model. The basic idea of these procedures is the same as for cylindrical specimen – see chapter 4.1.

The control part of the whole simulation is the parametrization block. This is the part where all input data should be inserted into the evaluation process. Through the parametrization block user can specify the dimensions of the CTS specimen,

the magnitude of loading force and parameters related to creation of the rough crack front and flanks.

This part of numerical simulation makes it usable for several geometrical and loading configurations. It also connects all parts of the simulation and ensures to keep whole model consistent.

4.2.1.1 Global model

The global model of CTS specimen represented the whole body of specimen with no simplifications – a full 3D model had to be used because of planned crack front and flanks complications.
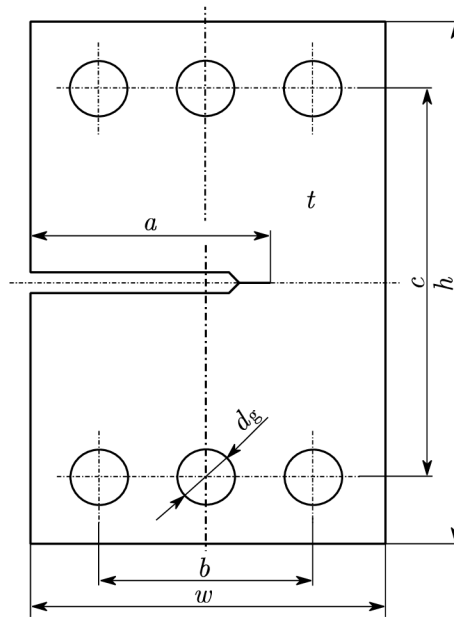
Fig. 51: Scheme of geometry of CTS specimen used for simulations

The overall geometry of the specimen (Fig. 51) is almost the same as original CTS specimen (presented by Richard [31]). Actual dimensions were used according to work by Li et al. [33, 34] (large specimen) and experimental setup which was used in conjunction of these simulations [69] (small specimen).

Table 1: Dimensions of CTS specimen models (in millimeters)

	Small specimen	Large specimen
a	22	60
b	25.2	54
c	51.2	108
d_{g}	8	15
h	68	145
t	4	10
w	42	90

Dimensions a, t and w (beside the others) written in Table 1 are the main (governing) dimensions – the analytical solution of SIFs is dependent on them.

The global model of numerical simulation was geometrically created the same for both small and large specimens, but obviously with different dimensions.
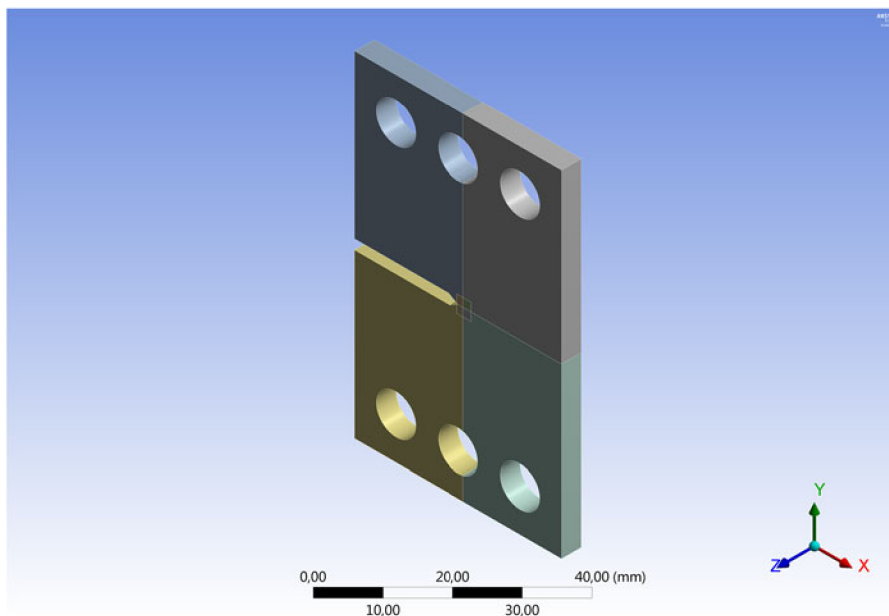
Fig. 52: Geometry of model of CTS specimen (small)

The whole geometry of model of the CTS specimen is shown in Fig. 52. Because of the overall 3-dimensionality of simulation, no simplification could be used in this model. Several lines dividing the model are also visible in Fig. 52. The whole geometry was divided into (roughly) quarters whereas the "center-point" of these quarters lies on the crack front. This is one way how to model a crack – the whole model was divided in this way and then it was reconnected in the FE mesh along all coincident planes except the two of them which formed the crack flanks. The other division of the geometry model which is visible in Fig. 52 is a small rectangle surrounding the crack tip. This rectangle encompasses the area with finer FE mesh to capture stress-strain singularity around the crack front as good as possible on the level of the global model.
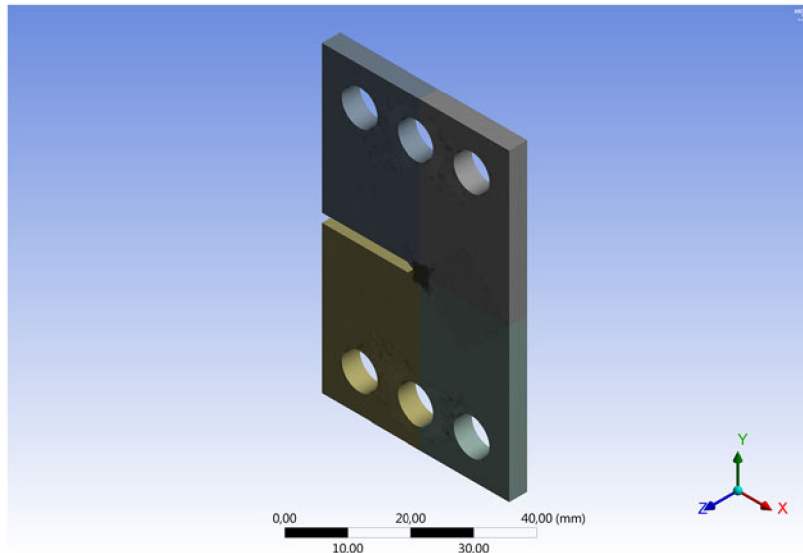
Fig. 53: FE mesh on global model

FE mesh used for the global model of the CTS specimen met the conditions usual for this type of modelling. The mesh consisted of quadratic SOLID186 3D mesh elements for better description of larger stress and strain gradients [18] which were expected in this type of model (mainly in the notch and crack area). The FE mesh density was good enough to describe the deformation of the whole specimen. The area where larger strain gradients were expected was meshed with much finer FE mesh (see darker area around notch tip in Fig. 53). Nevertheless, even such a fine mesh is not enough for the crack modelling purposes. A higher level of refinement of FE mesh would lead to accurate model but on the other hand the hardware demands of such model and the computational time would be much larger (presented model was created to fully use hardware capacity of employed computer). This problem was solved via usage of the submodelling (see next two chapters).
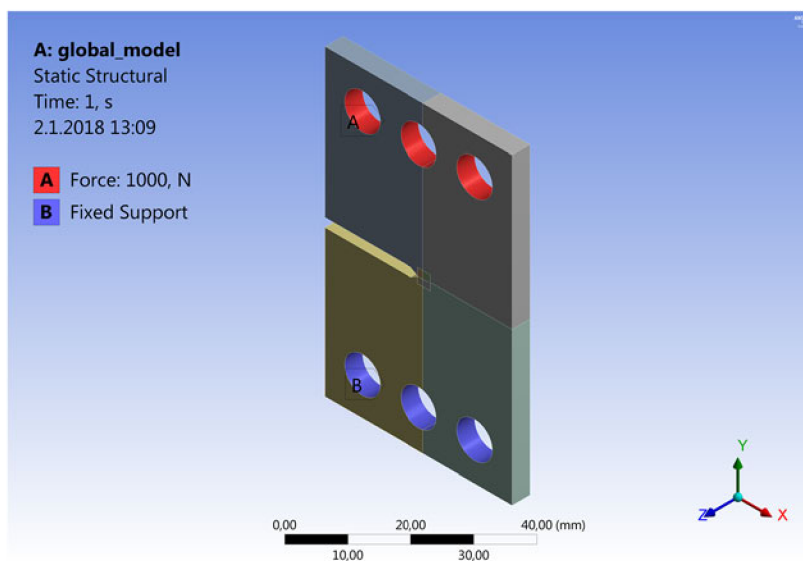
Fig. 54: Shear loading of global model of CTS specimen

52

The loading of the global model was consistent with original experimental CTS specimen setup (see chapter 2.5.1). Only the case of pure remote mode II loading was used and no mixed-mode I+II loading was evaluated (even that it is possible with this type of specimen to create remote I+II loading [31]). The remote mode II loading was achieved by fixing the bottom row of clamping holes (Fig. 54 – boundary condition B marked by blue color) and by force-loading of upper row of clamping holes in x-axis direction (Fig. 54 – boundary condition A marked by red color). To avoid unwanted twisting of the specimen (which can occur if this type of force-loading is used) an Ansys APDL command CP was used to couple the deformation of all nodes subjected to applied force. This command fixed all mentioned nodes together in such a way that the upper clamping holes moved together the same way as they were clamped in a rigid mount. The magnitude of the loading force was set for both small and large models to 1000 N. Since SIFs are linearly dependent on loading force, observed results were in all cases normalized to loading so the magnitude of force had no impact on results at all.

The material models used in this case were different for small and large models. Only linear elasticity of material models was considered, and it was described by the Young's modulus $E = 105$ GPa for small model and $E = 210$ GPa for large model and the shear modulus $E_{\text{shear}} = 38$ GPa for small model and Poisson's ratio $\mu = 0.3$ for large model. The material model for smaller specimen is the same as material model of Niobium used for cylindrical specimen (see chapter 4.1) and the material model for larger specimen represents standard structural steel (material properties obtained from Ansys material database). For the large model one additional modification of material properties was used – an artificial material model was created with the same elasticity modulus as structural steel but with Poisson's ratio set to 0. This artificial model was created to see the influence of lateral contraction of the model on observed SIFs for cracks under the remote mode II loading. Since SIFs are generally not dependent on the material properties the difference between small and large model should be negligible. However, the calculations for cylindrical specimen showed some differences due to lateral contraction for remote mode III loading (see chapter 4.1) hence for further research in that direction more types of material models should be used.

Results obtained from the global model of the CTS specimen were not accurate enough to determine exact values of SIFs. However, they should be good enough to determine if it represents the remote mode II loading well and if there is no gross error in input parameters and conditions.
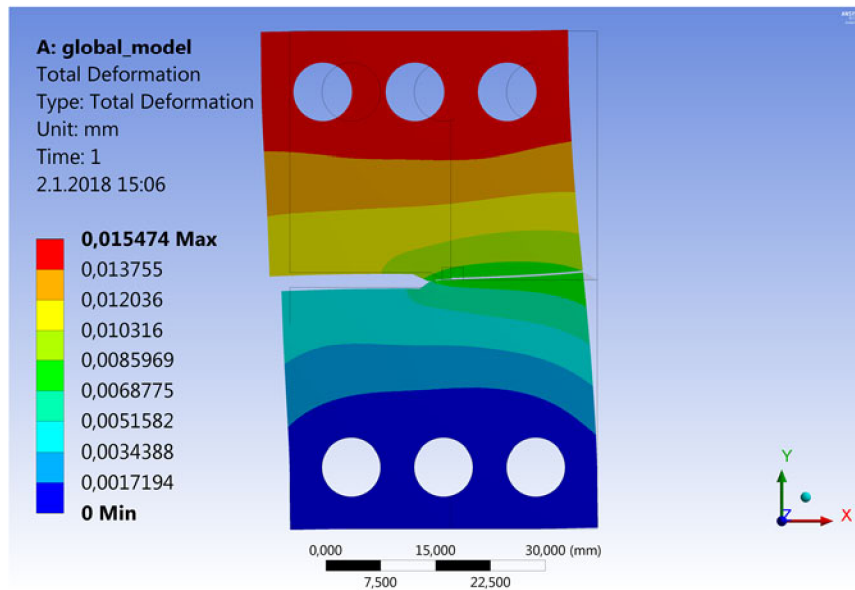
Fig. 55: Contour plot of total deformation of small CTS specimen (with undeformed wireframe, visible deformation is exaggerated 260-times)

The total deformation of modeled specimen (Fig. 55) follows used boundary conditions. The bottom of the specimen stays fixed in place and the upper part slides to the side, but all the gripping holes moves together as they were fixed in a rigid clamp. This causes the specimen to shear exactly as was needed to produce the remote mode II loading.
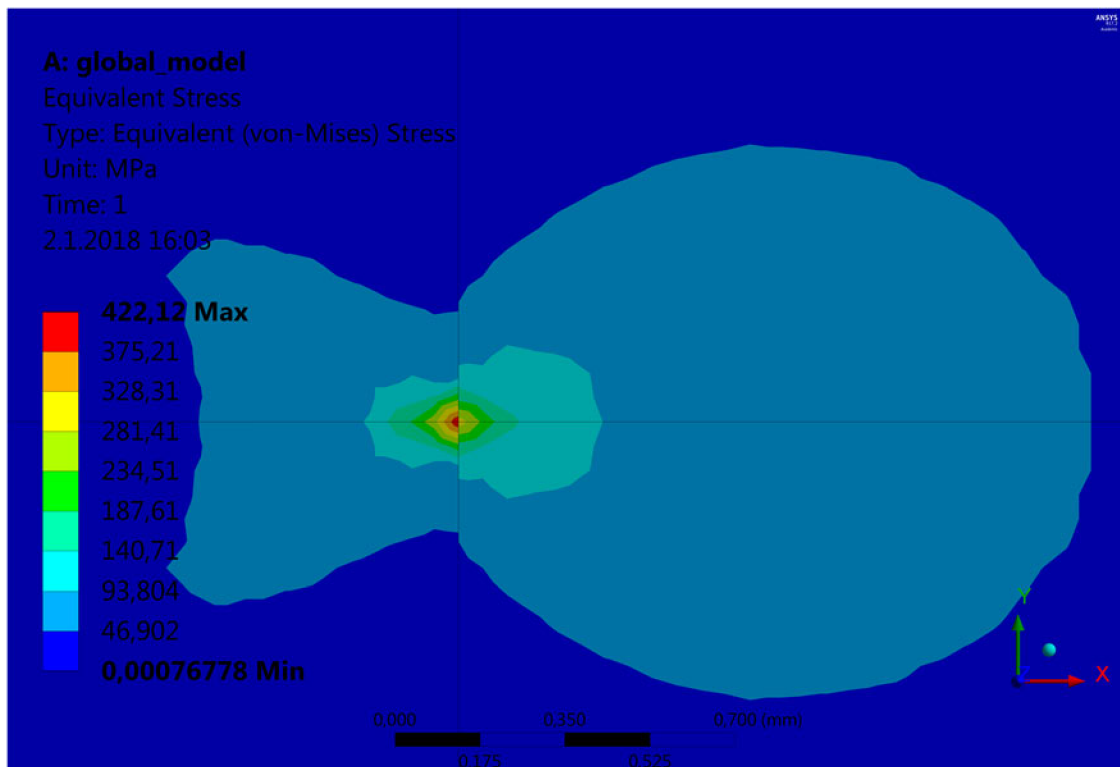
Fig. 56: Equivalent (von-Mises) stress around the crack front, side view
(the cross-section point of black lines denotes the crack tip)

The stress field around the crack front (Fig. 56) with its singularity point at the crack tip confirms that the crack itself is under the mode II loading. The shape of stress contours looks like an infinity sign wrapped around the crack tip which is consistent with linear-elastic fracture mechanics (LEFM) theory [17]. The only exception is the light-blue contour in the left of the picture which is close to the notch tip and it seems that this one was influenced by the notch root effect.
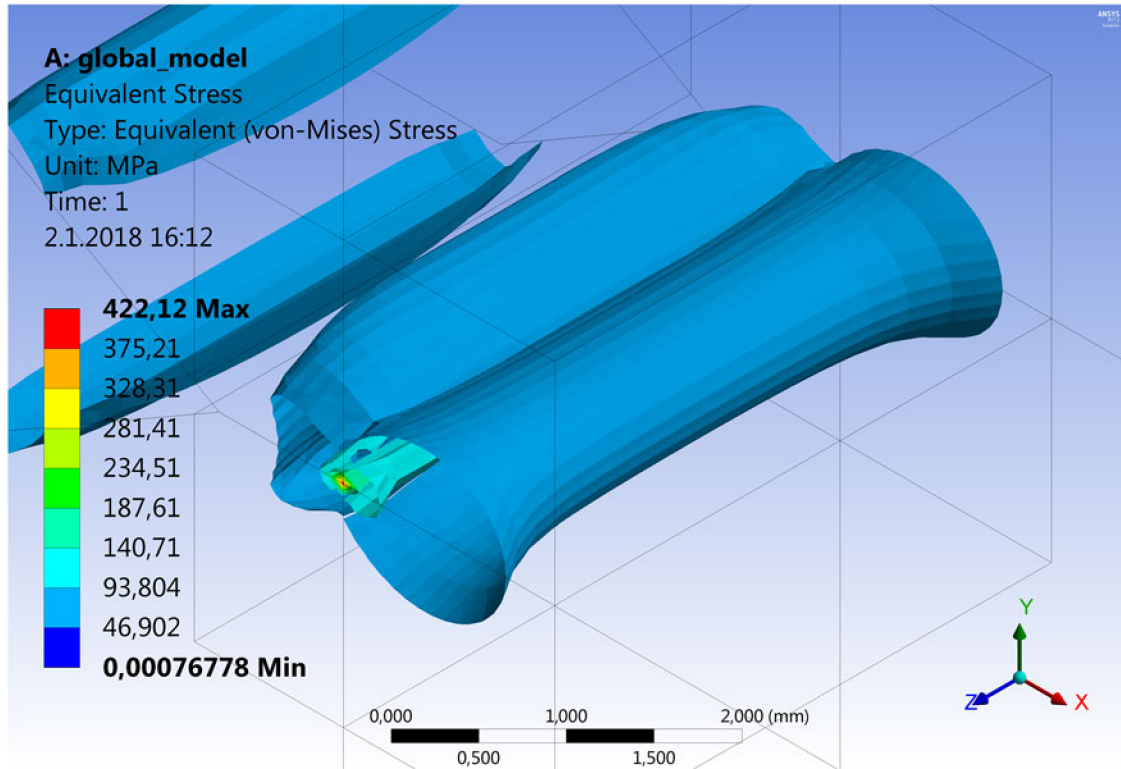
Fig. 57:Equivalent (von-Mises) stress around the crack front, iso-surfaces through-thickness of the specimen

The through-thickness view on the equivalent (von-Mises) stress (Fig. 57) also shows the free-surfaces effect along the sides of the specimen and the difference between plane stress and plane strain conditions. The expected change of the stress field at the sides of the specimen [6, 70] is visible even in the rough global model. However, the free-surfaces effect influences only a small area at the sides of the specimen and it has insignificant effect on the core of the specimen [6].

The inner iso-surfaces (Fig. 57 – light-green to red) show signs of insufficiently fine FE mesh for a detailed description of the crack parameters by their very rough and dissymmetrical shape which is not even close to theoretical one. This proves that a submodelling procedure with much finer FE mesh is needed even to capture the real stresses and strains around the smooth crack front.

Overall, the global model meets the requirements needed for submodelling and it can be used for further modelling. Furthermore, in the case of CTS specimen the overall crack length was the same for all variants and only crack microstructure was alternated

in submodel. This means that for all simulations of each model only one global model (one representing the small specimen and the other one representing the large specimen) could be used which saved the precious computational time.

4.2.1.2 Preparation of submodel

The next part of numerical process was submodelling. As was described above, the global model was not accurate enough to precisely evaluate the stress-strain fields around the crack front and also to include fine structure of the crack front (which is the subject to this research). To solve this problem a new, finer model had to be prepared. This model was smaller in comparison with the global model (volumetrically) and it was formed from a small portion of CTS specimen around the crack. The principle of using this smaller model as a submodel is the same as was for the cylindrical specimen (see chapter 4.1) but the process of creation of the submodel was slightly different.
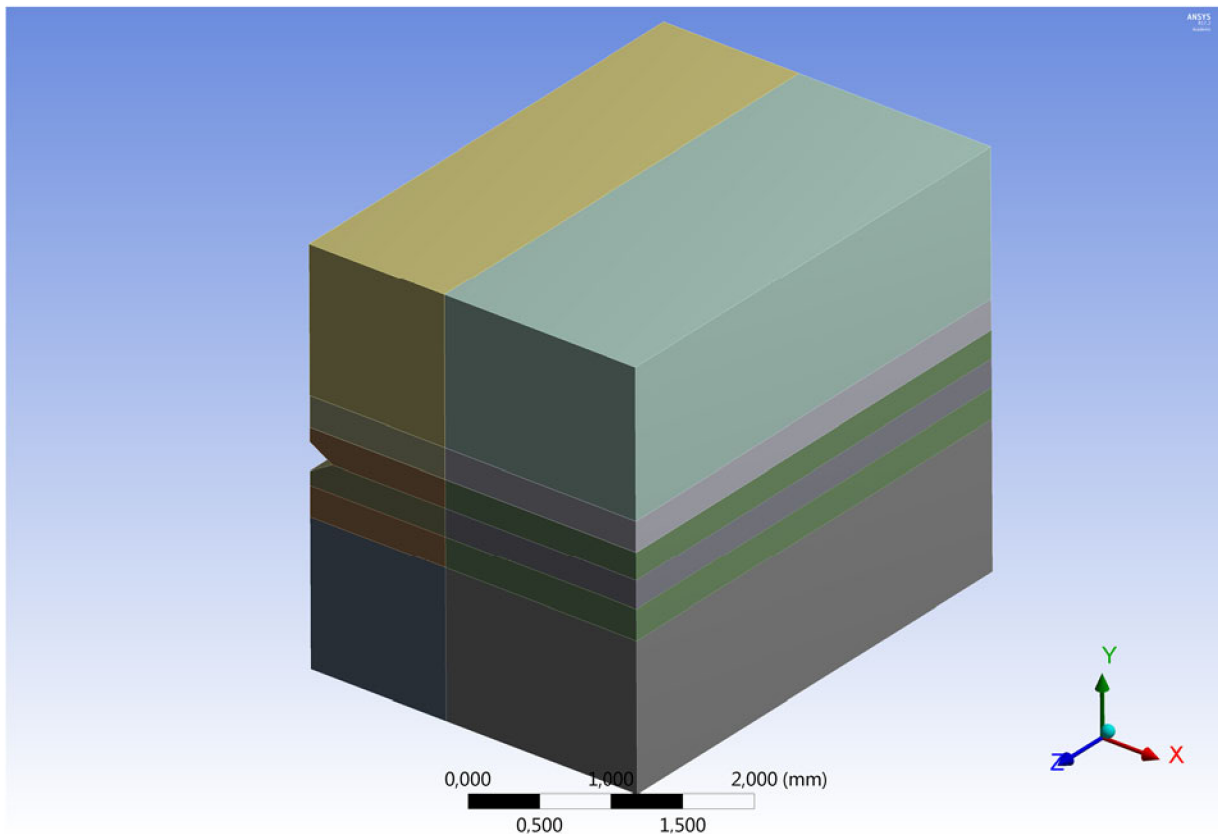
Fig. 58: "Prototype" of submodel

For the CTS specimen models a fully modifiable crack front and flanks were planed so the creation and parametrization of it could not be done as easily as for cylindrical specimen.

At first a so-called prototype of submodel was created simply by extracting a piece of geometrical model around the crack from the global model. This geometry was furthermore prepared for finer FE mesh at the vicinity of the crack by dividing its volume to several parts (Fig. 58).
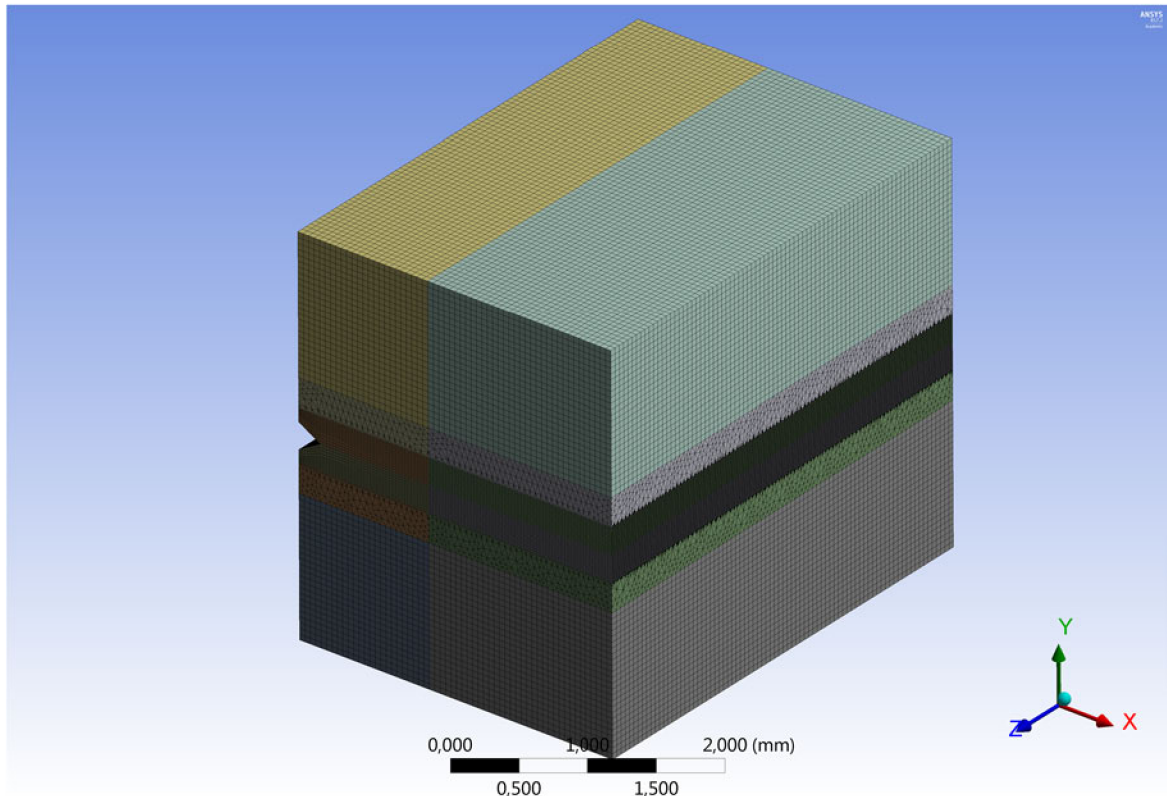
Fig. 59: Example of meshed "prototype" of submodel

As one can see in Fig. 59 the plates directly connected to central plane (which formed the crack flanks) were meshed with a very fine FE mesh. At the top and bottom of that volume a transition area was created and meshed with free 3D volume mesh. This transition area and then the outermost volumes with much rougher FE mesh had only one purpose – to reduce the overall mesh elements count to minimize the calculation time and hardware demands.

Mesh elements size in the submodel was connected to the parametrization block (see simulation flow-chart in Fig. 50) to always achieve the same number of mesh elements along any crack front asperity.
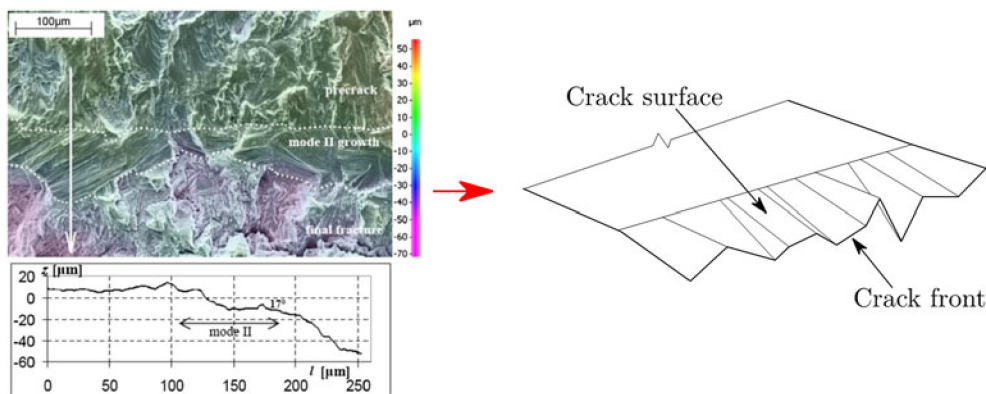
Fig. 60: Transition of real crack surface (3D stereophotogrammetry in SEM on the left by Vojtek et al. [56]) to simplified model (on the right)

The prototype of submodel contained still only straight and flat crack which was changed in the next step via Ansys APDL commands to move nodes on the crack flanks to change the shape of modeled crack front and flanks to represent the real-like crack shape as much as possible (see Fig. 60). The whole APDL commands block was created to be able to model the most complicated variant of the crack front and flanks with asperities in all directions created in a pseudo-random manner. Each complication of the crack front and flanks could be than disabled to change the model complexity.
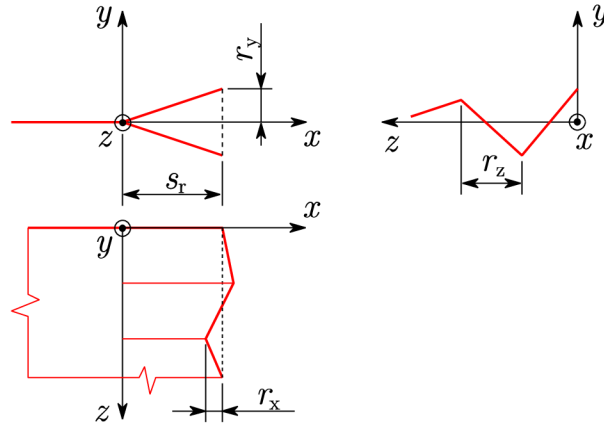
Fig. 61: Schema of fully rough crack front

For the most complicated variant the tortuous crack front and flanks were created with several constraining factors (Fig. 61) governed by general parametrization. The dimensions of length of the rough portion of the crack s_r and distance between roughness peaks r_z were set as constants defined in the parametrization block (the distance r_z was in meshing process divided into four mesh elements). Other two roughness parameters r_x and r_y were set by a maximum value (amplitude) and for each crack flank kinking (segment) it was multiplied by a random number from -1 to 1 which was controlled by a key randomizing parameter. This randomization part could be disabled and changed to create alternating crack front peaks with r_x or r_y alternating from 1-times their amplitude to -1-times their amplitude. In that way a uniform zig-zag crack front shape could be formed. Moreover, by setting one of used amplitudes (either in x or y direction) to 0 μm the tortuosity in the respective direction could be disabled.

The actual shifting of used mesh nodes was done by combination of numerical matrix edits and actual APDL commands. At first, to create a procedure for changing the node positions, the pivotal vectors of r_x and r_y for all roughness peaks were created (with use of rows of random numbers or alternating amplitudes as was described in a paragraph above) and then they were mapped (by linear interpolation) to all node positions on the facets between crack roughness peaks. Resulting two matrices were composed of values representing the new positions of nodes in respective axis directions and they were applied as a shift of all nodes of crack front and flanks. This action provided desired tortuous shape of crack which could have inherently random character defined at maximum by five parameters (s_r, r_x, r_y, r_z and the randomizing parameter).

58
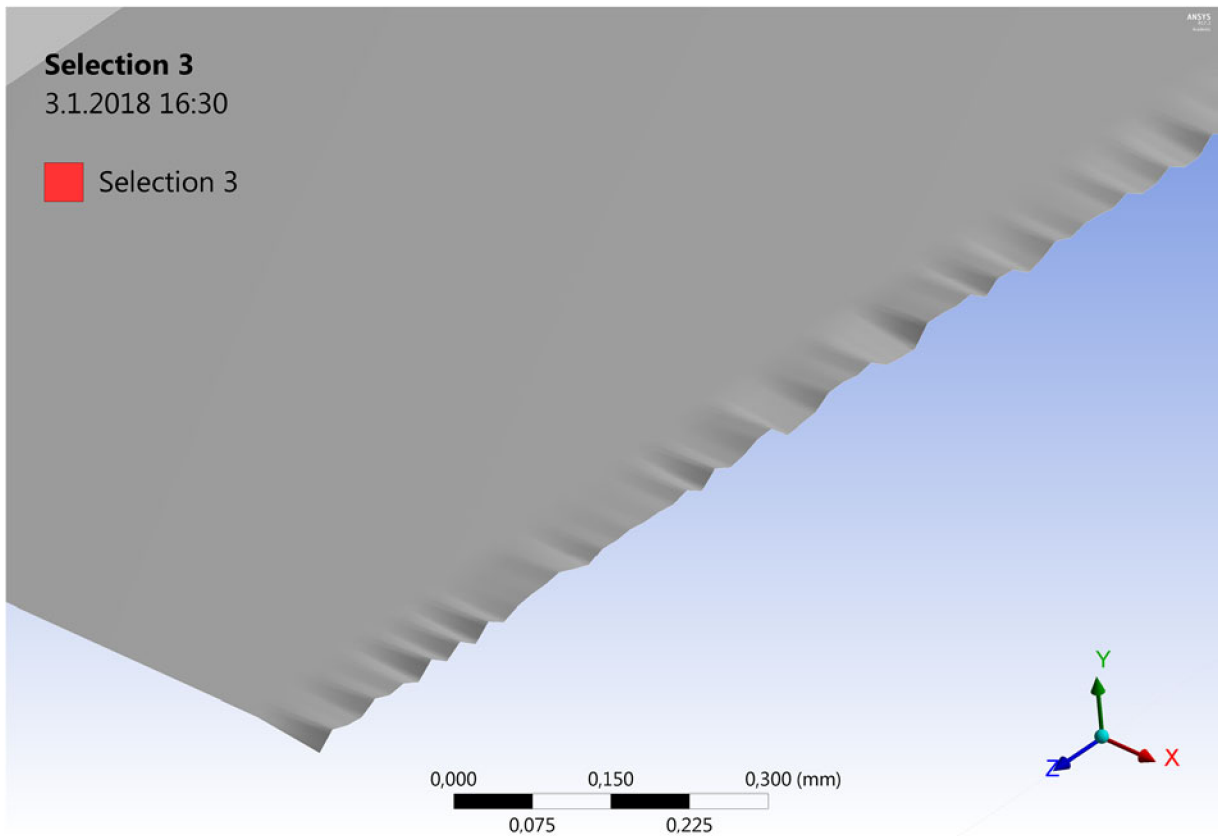
Fig. 62: Example of randomly generated crack front and flanks

Resulting FE model with shifted mesh nodes had to be converted back to volumetric model via Ansys built-in converter (finite element modeler, see Fig. 50). After conversion from the simple mesh to complete model the submodel was finally created with user-specified tortuous crack front and flanks (Fig. 62). The actual randomness and complexity of tortuosity could be modified (as was described above) to suit the actual research purpose.

4.2.1.3 Submodel

After creation of fully parametric procedure to create any type of crack tortuosity (within the boundaries described in chapter 4.2.1.2) the actual submodel could be prepared and used to calculate desired results.
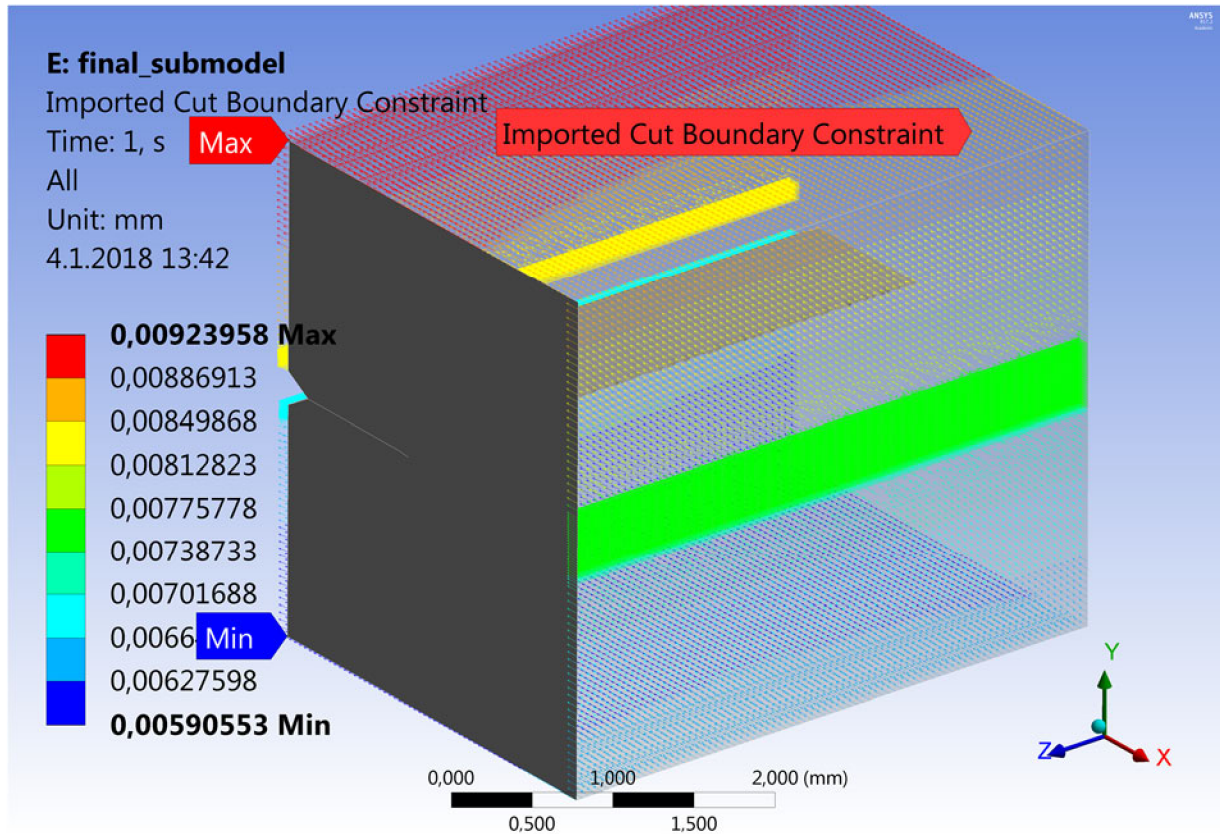
Fig. 63: Example of cut boundary constraints on submodel of CTS specimen

The loading of the submodel was applied in conjunction with standard submodelling procedure [18]. Resulting displacements from global model were interpolated to boundary mesh nodes of the submodel (example in **Fig. 63**). The boundary nodes were actually all mesh nodes on boundaries (cut-out faces) of the submodel, where it was cut from the global model geometry.

The material model properties had to be the same as for global model to carry out correctly the submodelling.

As a result from submodel, the stress and strain fields (much more precise than from global model) could be extracted and moreover, the submodel was fine enough to obtain resulting SIFs along the crack front.
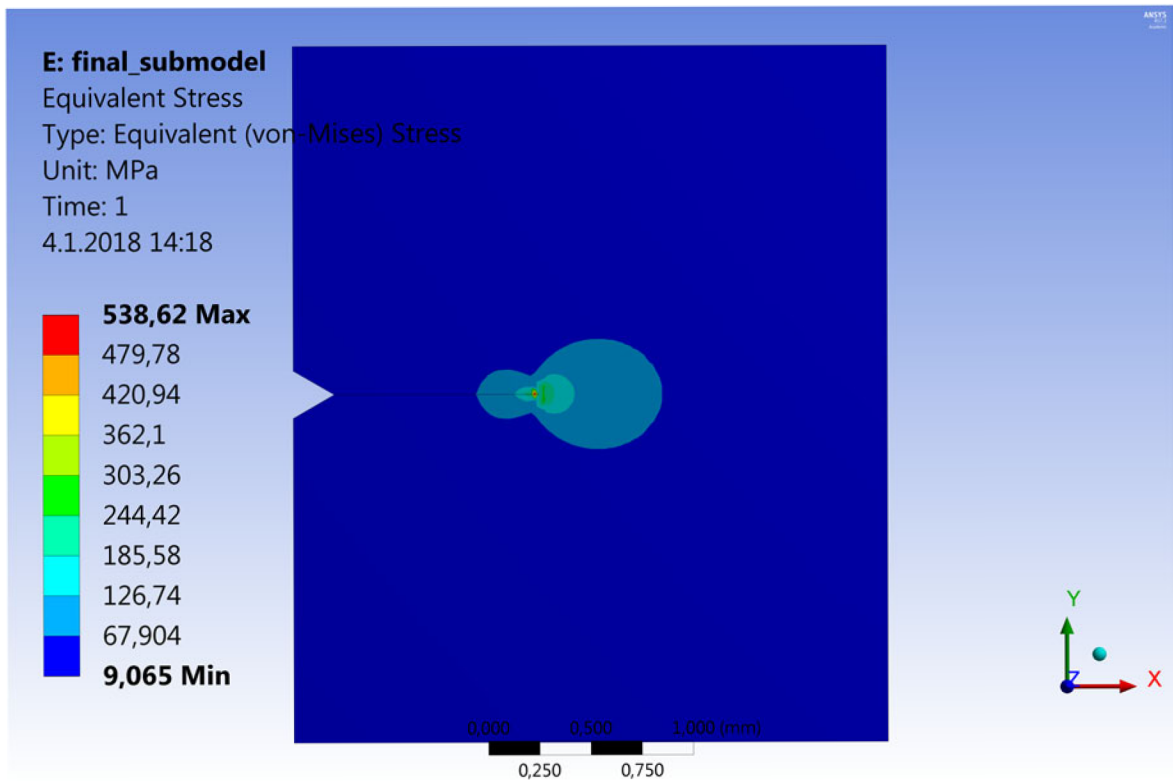
Fig. 64: Equivalent (von-Mises) stress, CTS specimen, submodel with straight crack, side of the specimen (plane stress conditions)
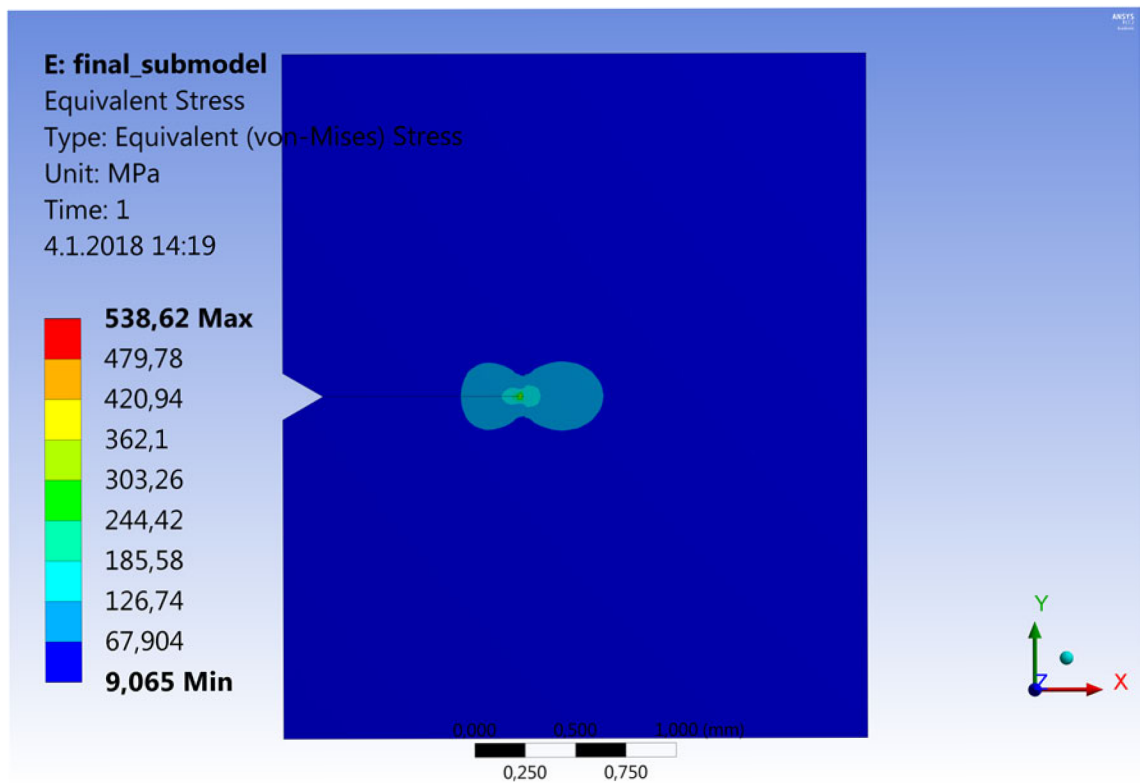
Fig. 65: Equivalent (von-Mises) stress, CTS specimen, submodel with straight crack, center of the specimen (plane strain conditions)

The equivalent (von-Mises) stress field around the crack front is qualitatively consistent with the analytical theory (e.g. [17]) and the shape of isolines close to the crack front is similar to infinity sign (see Fig. 64 and Fig. 65) as predicted from LEFM theory (e.g. [6, 17]). These results prove that the used model is valid for the mode II crack modelling. The difference between plane stress and plane strain condition on free surfaces of specimen (Fig. 64) and in the bulk of specimen (Fig. 65) respectively are also clearly visible. This shows that current model is able to comprehend this phenomenon too.
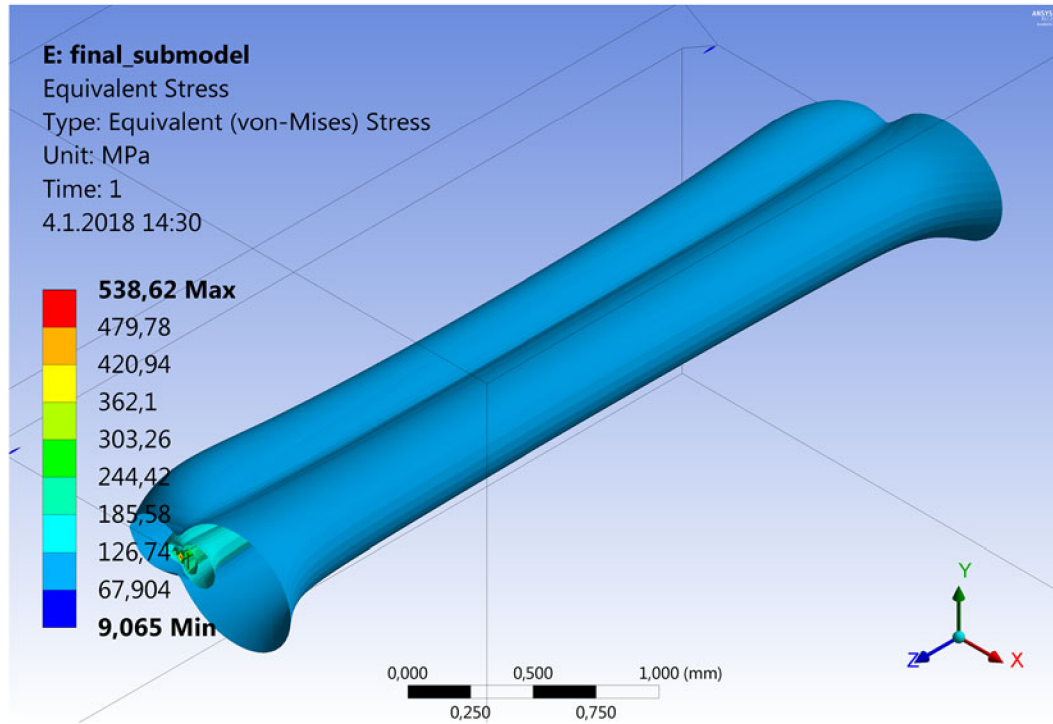
Fig. 66: Equivalent (von-Mises) stress along the crack front (iso-surfaces)

Actual transition between the plane stress and the plane strain conditions is clearly visible on visualization of iso-surfaces of the equivalent (von-Mises) stress along the straight crack front (Fig. 66).

Besides the stress and strain fields the SIFs could be also evaluated. As was mentioned above, the raw SIFs are linearly dependent on loading force and also on overall geometry of the specimen. To get comparable results the raw data were normalized according to following formula:

$$K_{i,n} = \frac{K_i}{\frac{F}{w \cdot t} \cdot \sqrt{\pi \cdot a}}, \quad \text{where} \quad i = \text{I, II, III,} \tag{29}$$

where F is the loading force and w, t and a are the geometrical dimensions of the specimen (see Table 1). For all depictions of SIFs results for CTS specimen along the crack front also the position at the crack front was normalized to unit length – the sides of the specimens are ±0.5 and the center of the specimen have 0 coordinate.
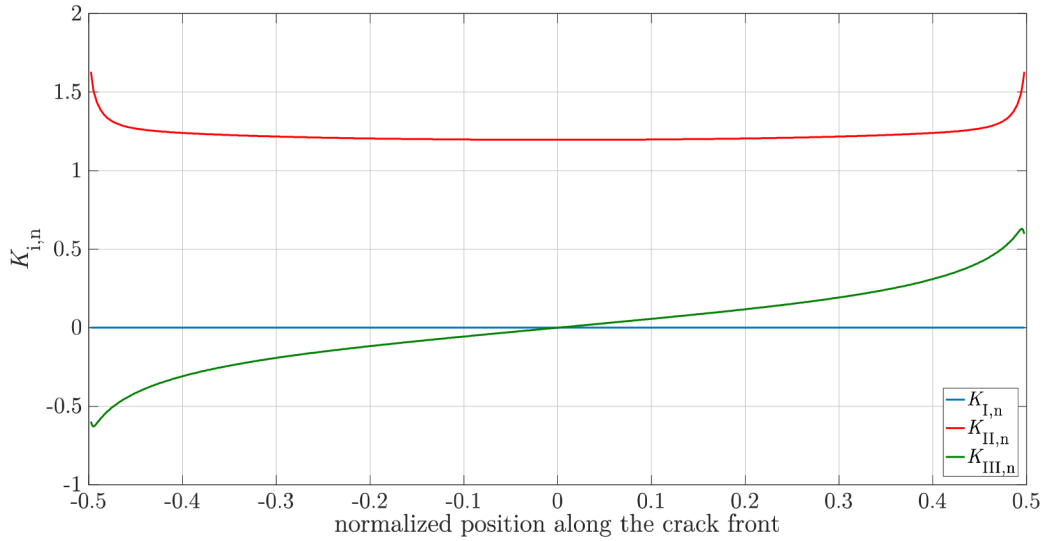
Fig. 67: Normalized SIFs for CTS specimen (small) with straight crack front

Normalized results for the small specimen with straight crack front confirm validity of used model. The resulting SIFs are as were expected for remote mode II loading. Mode I SIF is virtually 0 (the maximal value of normalized $K_{I,n}$ is $8.8 \cdot 10^{-4}$ which is deeply below the other two SIFs). Mode II SIF is on the other hand the dominant one and the mode III SIF exhibit slight increase (in absolute values) towards the sides of the specimen but overall it is still much lower than mode II SIF. The local changes in $K_{II,n}$ and $K_{III,n}$ towards the free surfaces of the specimen were also expected and described by e.g. Pook [6] as a free surface effect caused by lateral contraction of material. In the end, the results for the straight crack from used model are in a very good agreement with results obtained by Li et al. [33].
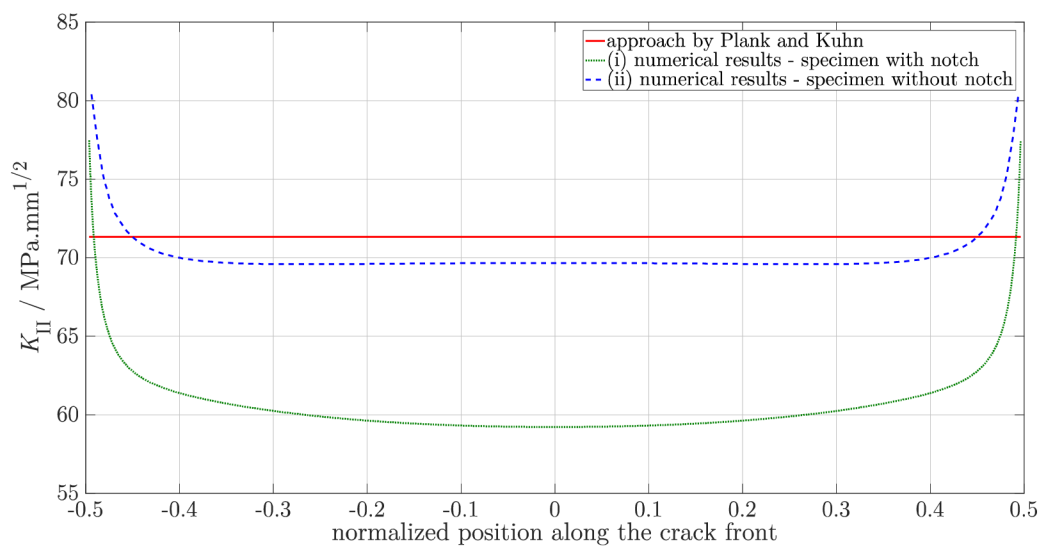
Fig. 68: Comparison of numerical and analytical approach for CTS specimen

63

Numerical results for the CTS specimen with straight crack were also compared to analytical approach introduced by Plank and Kuhn [41]. Absolute value of K_{II} for CTS specimen can be obtained by analytical formula (19) (in chapter 2.5.1). Evaluated value of K_{II} corresponds to 2D model of the CTS specimen and for geometry of the small specimen and loading used in numerical simulation the actual result can be seen in Fig. 68 as a red straight line. This value was compared at first with raw results from numerical model of standard notched specimen - the K_{II} progression along the crack front is visible in Fig. 68 as a green line (i). It is clear that there is a significant difference between analytical model and numerical model of real 3D notched specimen. Because of this the second model of CTS specimen with straight crack front was created in Ansys software. New model did not include notch, but it had the crack of a full-length a instead (see Fig. 51). Results of this model are depicted in Fig. 68 as a blue dashed line (ii). One can see that these new results are very close to the analytical model. This fact points out to a conclusion that analytical model assumes none or insignificant influence of the notch in the specimen, but the full 3D numerical model of the notched specimen shows small but noticeable influence of the notch on SIFs for this type of the specimen geometry. When no notch is introduced to the numerical model the results of analytical and numerical approach are almost similar.

The other difference between analytical and numerical models is the sudden increase in K_{II} at the sides of the specimen. This is because of lateral contraction of the specimen and because of the influence of the free surface of the specimen [6] which cannot be accounted for in the 2D analytical model.

Nevertheless, the notch influence and side effect have no impact on evaluated results from numerical models – all results from models with geometrically modified crack front and flanks were always compared with the numerical model with straight crack which was notched too which eliminates its influence on results used as ratios.
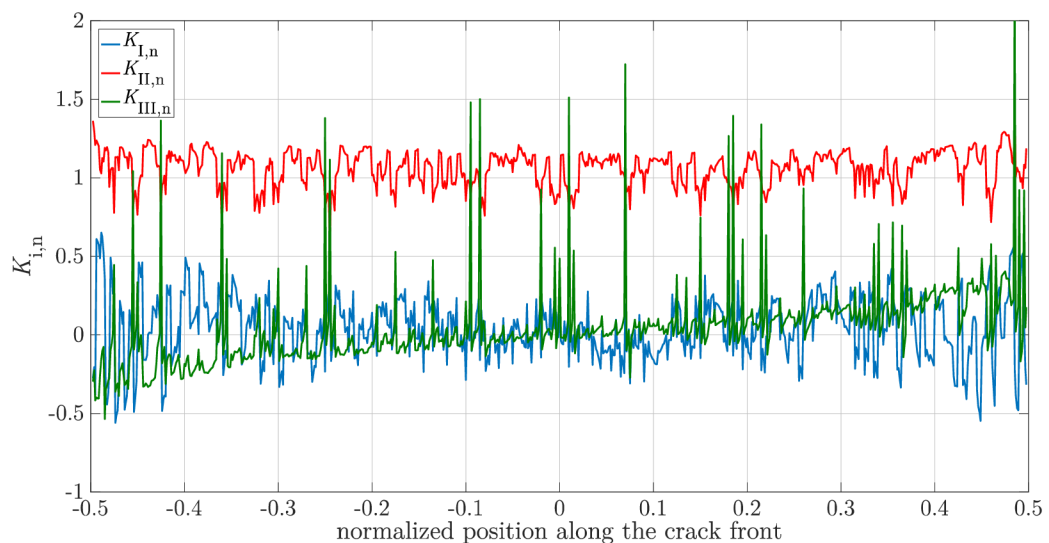
Fig. 69: Example of normalized SIFs for CTS specimen (small) with rough crack front

If some crack front roughness is introduced to the model, observed SIFs changes on the local level. As can be seen in Fig. 69, the global (or mean) progression of SIFs along the tortuous crack front (in this case with random crack front asperities distribution) follows the same rules as for the straight crack in similar specimen. $K_{I,n}$ is very close to 0, $K_{II,n}$ is still dominant and $K_{III,n}$ follows the trend with increase close to sides of the specimen. On the other hand, all three SIFs exhibit oscillations and local peaks related to each geometrical asperity. Even mode I SIF in some places (especially on the sides of the specimen) reaches the local value comparable to mode II SIF.

Also from the global view, mode II and III SIFs exhibit decrease of their mean progressions in comparison with results from the straight crack (for example in Fig. 67 the function of $K_{II,n}$ for the straight crack front is around the 1.25 value but the same SIF for rough crack front on Fig. 69 oscillates around value 1).

4.2.1.4 Methods for results processing

Unlike the cylindrical specimen, for the CTS specimen there were more researched variants and the results processing was for almost all of them the same. In general, two methods were used – local view on local k_1, k_2 and k_3 along one distinct crack front asperity and a description of influence of the crack roughness on mean progression of the SIFs along the crack front.

The results evaluation along one particular crack front asperity is based on the same principle as was used in chapter 4.1, thus the evaluation of ratios of significant local SIFs $k_{i,n}$ (where i = 1, 2 or 3) at a point on crack front to applied SIF $K_{j,n}$ (where j = I, II or III, obviously for CTS specimen under remote mode II loading in subsequent chapters j = II) was used. The evaluation points for this ratio should always be along one particular asperity but their exact location will be described in respective chapter below, where the actual results are processed.

The second method for results processing is rather more complicated. If results from the standard planar model of the crack are compared with results from the model with any kind of tortuous crack front (e.g. comparison of results in Fig. 67 and Fig. 69) one can see that mean value of function of the local SIFs $k_{i,n}$ (where i = 1, 2 or 3) along the tortuous crack front is different than the same results function for the standard crack front. It seems that the mean value of results from rough crack front are a kind of shifted. For the quantification of this shift of results a method based on function interpolation was devised.
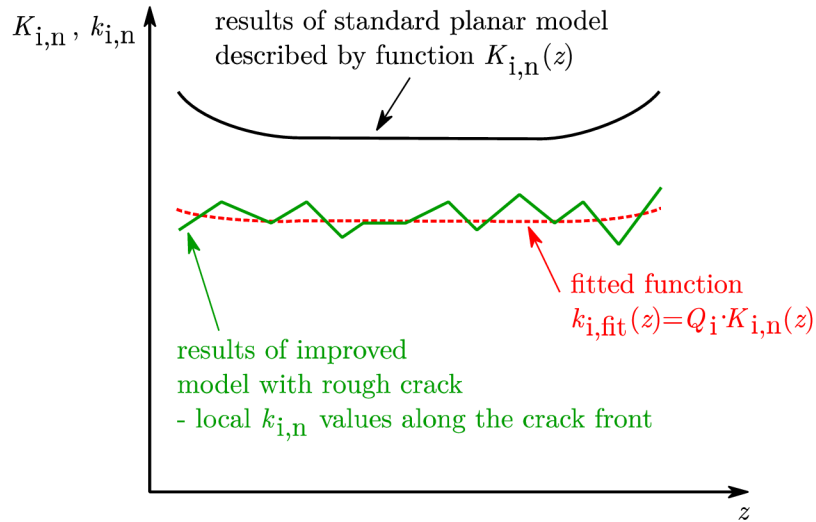
Fig. 70: Schematic explanation of method for obtaining the quotient Q_i

The described shift of results is schematically depicted in Fig. 70. Results obtained from standard, planar model can be described by a function $K_{i,n}(z)$ which can be easily analytically formulated (black line in Fig. 70). This function corresponds to global loading of the specimen with simple, planar crack. On the other hand, results from model with tortuous crack front are a set of local values $k_{i,n}$ along the whole crack front (schematically described by green jagged line in Fig. 70). If this set of result points is interpolated by a function which is a Q_i-multiple of function $K_{i,n}(z)$, the coefficient Q_i actually quantifies the ratio between (a sort of) mean value of results from the rough crack and results from planar model of crack and thus it describes the decrease of global SIF value. To obtain the quotient Q_i for any needed crack loading mode only a linear least square method interpolation [71] was performed on respective datasets and function $K_{i,n}(z)$ with use of the Matlab code.

4.2.2 Researched variants (CTS specimen)

To describe the crack front and flanks roughness influence on the crack behavior and propagation, several things have to be accounted for. In the case of the remote mode II loading a complex approach was employed by looking at the crack geometry from several points of view.

At first the in-plane (similar to one described for remote mode III loading, see chapter 4.1.2.2) and out-of-plane crack roughnesses were researched separately to see their individual contribution to changes in crack parameters. Then these two types of the crack micro-geometries were combined and investigated together.

The next stage involved a real-like model of crack front and flanks involving portion of the crack which was planar and small part with rough surface introducing both crack tilt and twist. This (or similar) type of the crack front and flanks geometry was observed during the SEM fractography on mode II crack after fatigue tests [56].

Also, some initial attempts to describe the decrease of mode II SIF caused by tilted and twisted crack with roughness in the direction of crack path (sort of in-plane crack roughness) were done using the ratio of remote $K_{II,n}$ and local values of $k_{2,n}$ for microstructurally rough crack front.

4.2.2.1 Uniform crack roughness (decrease of global SIFs)

As was described in previous chapters, the crack front and flanks geometry is planar in minimum of real-life cases. In fact, the observations of cracks and pre-cracks morphology showed significant in-plane and out-of-plane roughness of the crack geometry [7, 72]. As was mentioned in chapter 4.1, small changes in crack front and flanks micro-geometry affects overall SIFs progressions along the crack front. In this case a uniform distribution of crack front asperities along the fracture in small CTS specimen (see Table 1 in chapter 4.2.1.1) loaded in pure remote mode II were investigated.
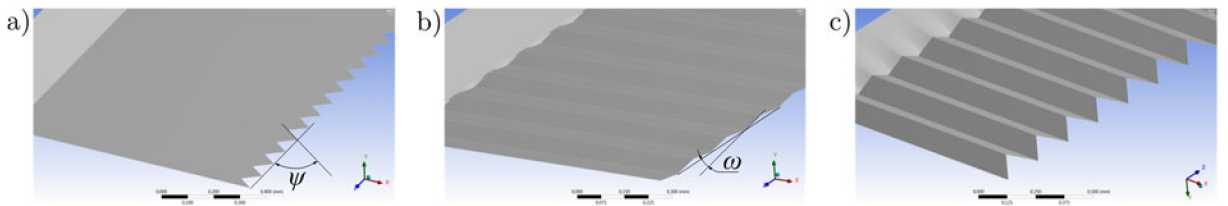
Fig. 71: Examples of modeled crack tortuosity: a) in-plane; b) out-of-plane; c) combined

The crack micro-geometry was modeled in three different types. The parametric model described in chapter 4.2.1 was adapted to create uniform distribution of asperities according to the following conditions (where for better description a coordinate system with x-axis parallel to the crack-length direction, the y-axis perpendicular to crack faces and the z-axis parallel to the crack front tangent was established). At first the in-plane tortuosity was modeled (Fig. 71 a)) where the crack front followed the zig-zag shaped path but the crack itself with crack front stayed in x-z plane. Each crack tooth was

described by angle ψ, which was the same for all teeth along the crack front and varied from 11.2° to 43.6°. The second investigated type of crack front tortuosity was out-of-plane roughness (Fig. 71 b)) characterized by the zig-zag morphology only in the y-z plane (factory-roof-like morphology) with all asperities characterized by angle ω which varied from 14.0° to 26.6°. The third configuration of modeled crack geometry was the combination of two previous cases (Fig. 71 c)) characterized by both asperity angles. The range of angles ψ and ω was chosen to correspond with the naturally occurring range of crack front and flanks roughnesses.
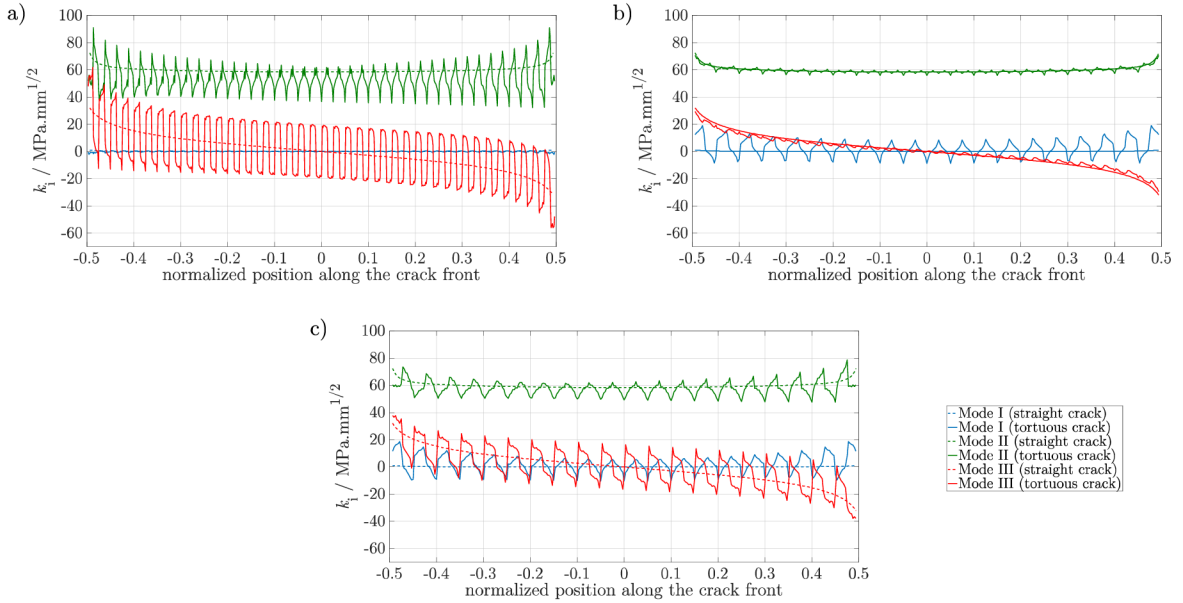
Fig. 72: Examples of difference between SIFs for straight and rough crack: a) in-plane tortuosity ($\psi = 11.2°$); b) out-of-plane tortuosity ($\omega = 14.0°$); c) combination of two previous cases

Local changes of SIFs along the crack front caused by different types of modeled crack micro-geometries are clearly visible in Fig. 72. Fig. 72 a) shows that, in the case of in-plane tortuosity, the component k_1 exhibits only very small local oscillations with zero mean value along the whole crack front, i.e. it practically does not differ from that for the straight crack front. The components k_2 and k_3 oscillate with much higher amplitudes and their mean values also change along the crack front which represents a rather significant difference comparing to the results for the straight crack front. In the case of the out-of-plane roughness (Fig. 72 b)), the local k_1-values are more pronounced particularly at crack-front points adjacent to free surfaces (specimen sides). On the contrary, the values of k_2 and k_3 components are almost unaffected and coincide with those for the straight front. The combination of both types of roughness (Fig. 72 c)) shows differences of all three local SIFs from those of the plane (straight) crack, but slightly less significant when compared to previous types [73].

The change of mean functional values of SIFs from rough cracks is visible for all investigated cases. This change can be described by quotient Q_i (for description

of Q_i see chapter 4.2.1.4). Only mode I SIF was omitted from evaluation of Q_i, because in all cases k_1 oscillates around the $0\,\mathrm{MPa \cdot mm^{1/2}}$, hence the quotient Q_I would be nonsensical.
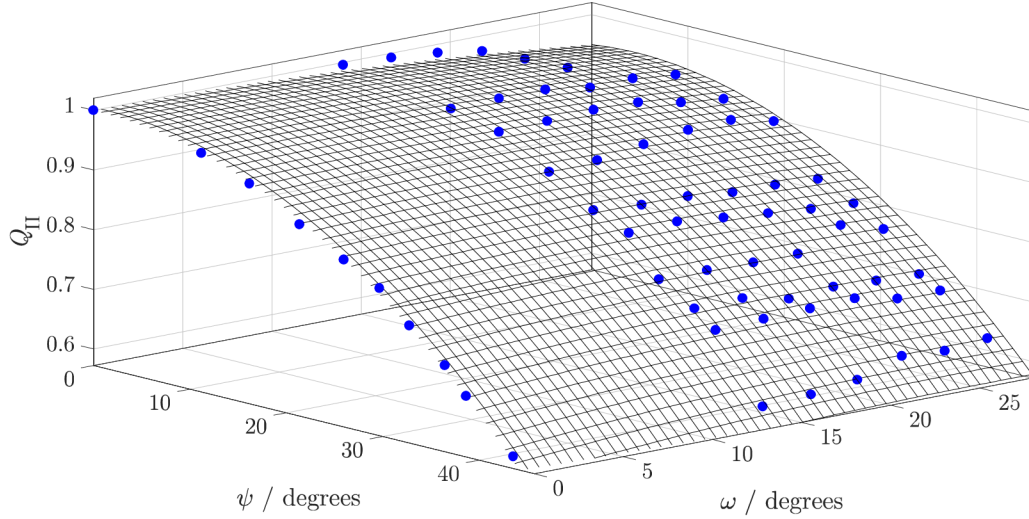
Fig. 73: Quotient Q_{II} as a function of both asperity angles ψ and ω
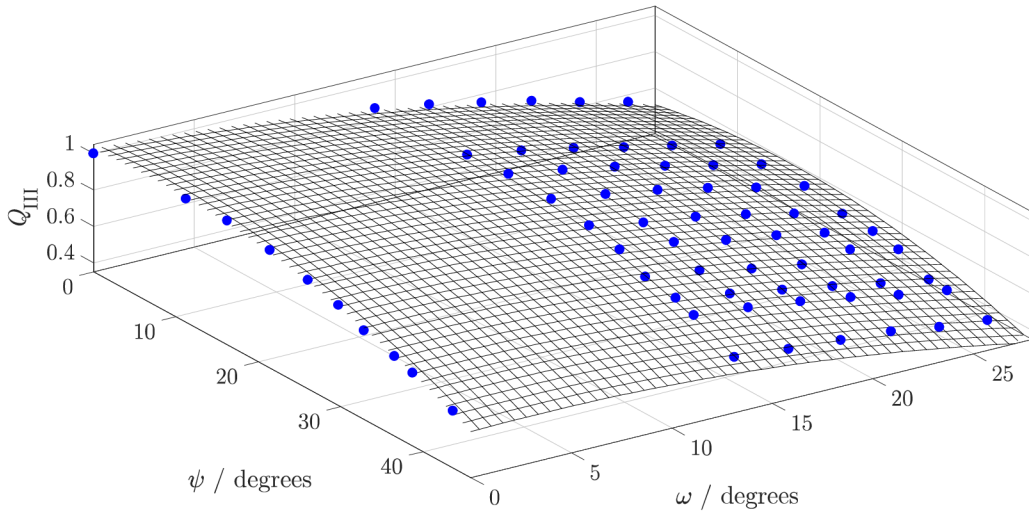
Fig. 74: Quotient Q_{III} as a function of both asperity angles ψ and ω

The change in global (mean) values of SIFs was quantified by quotients Q_{II} (Fig. 73) and Q_{III} (Fig. 74) as functions of angles ψ and ω. Obviously, both mode II and III SIFs at the rough crack front are decreasing with increasing angles ψ and ω (increasing roughness) due to the geometrical shielding effect. The decrease of the mode II SIF values is much more influenced by the in-plane tortuosity than by the out-of-plane roughness, while the mode III SIF values decrease more rapidly and in a similar rate for both ψ and ω angles. As shown in Fig. 73 and Fig. 74, the results for both Q_{II} and

Q_{III} could be approximated by a quadratic surface function of angles ψ and ω, as a very good fits quantified by the R-square value higher than 0.98. Obviously, the point $[0; 0; 1]$ corresponding to the straight crack front and the smooth crack flanks, belongs to this surface function. The results obtained for global SIFs can be utilized to correct experimental values of mode II effective fatigue thresholds in metallic materials obtained under the assumption of smooth precracks. According to Fig. 73, for example, the reduction of the measured threshold values in ARMCO iron and niobium should be around 15% since the in-plane mean angles of pre-crack fronts measured in these materials were $\psi = 25°$. However, this correction is just a rough prediction since the out-of-plane roughness characteristic angle was not determined for mentioned pre-cracks by the time of completion of this thesis.

4.2.2.2 Uniform crack roughness (one particular asperity)

A more detailed view of the results (Fig. 72) reveals that, in the case of the CTS specimen, a true pure mode II loading state at the straight crack front occurs only in the middle part of the specimen (see also [34] or [6]). The rest of the crack front has to be considered to be loaded by mixed mode II+III. Due to this fact, the crack front asperity at the exact center of the specimen was picked for the evaluation of detailed local loading modes along one elementary tooth (asperity).
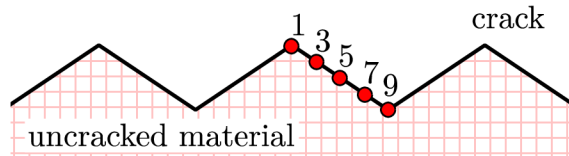
Fig. 75: Example of node numbering along one crack front asperity (in-plane serrated crack, top view, only odd-numbered nodes are showed)

The portion of model around the crack front was uniformly discretized by a fine FE mesh. Each crack asperity along the crack front (in all modeled crack configurations) was modeled with nine nodes from which the first and the last one was shared by the previous or the next asperity, respectively – see Fig. 75. This means that for each elementary crack front serration nine evaluation points for obtaining local SIFs were available but the first and last one had to be omitted, since the crack front direction could not be well defined there. The omitted nodes at the sharp edges of the elementary crack front tooth are denoted by numbers 1 and 9. The node No. 1 lies at the top of the jagged line and the node No. 9 is in the outermost groove of the material. In the further description of the numerical results only the nodes No. $2-8$ will be utilized for evaluation of the local SIFs.

In the above-mentioned evaluation nodes along an asperity in the center portion of the specimen the ratios of k_3/K_{II} and k_1/K_{II} were evaluated for in-plane and out-of-plane roughness, respectively, and for all selected values of the angles ψ and ω.

70
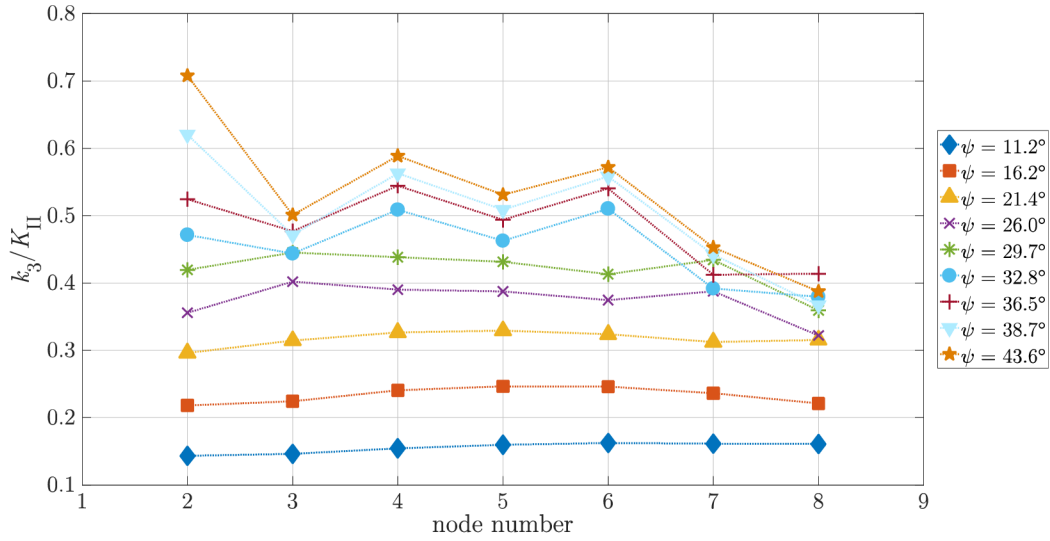
Fig. 76: Normalized values of local k₃ along one crack asperity (in-plane roughness)
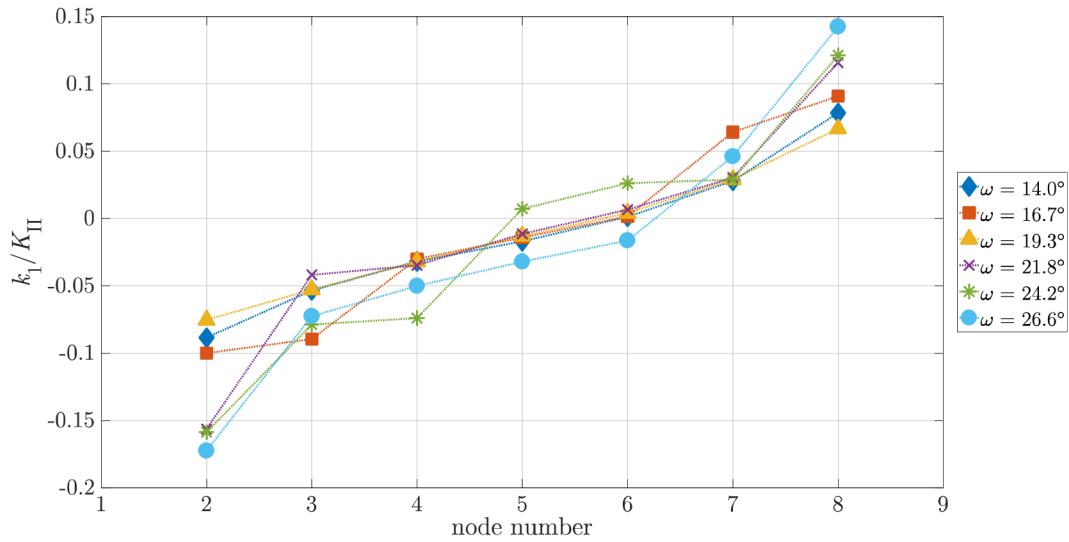
Fig. 77: Normalized values of local k₁ along one crack asperity (out-of-plane roughness)

Local values of the ratio k_3/K_{II} along the half-tooth show an expected increase with an increasing angle ψ for the in-plane roughness (Fig. 76). In addition, the ratios k_3/K_{II} for ψ higher than 26.0° tend to exhibit an increase towards the evaluation node No. 2, which is more pronounced for the highest asperity angle 43.6°. This node lies, according to Fig. 75, at the innermost part of the crack tooth where the crack length is the smallest, but the stress concentration is the highest due to the effect of the asperity. The increase of local mode III SIF towards the node No. 2 is in a qualitative agreement with the results for local k_2 obtained for a serrated crack front loaded by remote mode III, which were described similarly in terms of the ratio k_2/K_{III} in chapter 4.1.2.2 where the cylindrical specimen was examined [73].

On the other hand, the ratio k_1/K_{II} for cracks with out-of-plane roughness (Fig. 77) is very small. This ratio should be even zero along the entire out-of-plane tooth according to a simple stress tensor transformation method (for more information on stress tensor transformation method please see following chapter 4.2.2.3). It means that the small tensile and compressive stresses are just local perturbations resulting from a more accurate numerical analysis describing the full complexity of 3D model.

4.2.2.3 Tilted and twisted crack segments

The other type of the crack front and flanks tortuosity is the complex 3D crack front tilt and twist. In this case almost whole crack from the notch tip is considered planar, but in the area close to the crack front the crack starts to deviate from its planar shape to both upper and bottom directions.

Two approaches, which are presented in this chapter, were already published by the author of this thesis in [74].
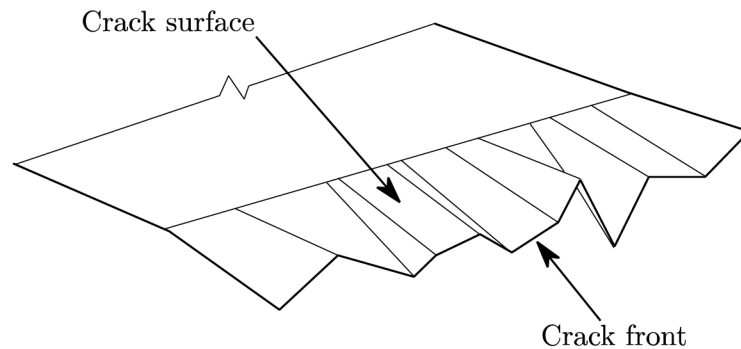
Fig. 78: Schema of tilt and twist of crack front and flanks

Modeled shape (Fig. 78) was created using almost all CTS model parametric functions. Two crack teeth parameters r_y and r_z were used as well as the tilt length s_r (see chapter 4.2.1.2, Fig. 61). The tilt length was set constant to length of 80 µm through all simulations of this type and the crack teeth amplitudes varied to create cracks with different roughnesses. Actual heights of the crack front teeth were then created randomly by multiplication of the amplitude r_y by a random number between +1 and -1 and the distance between each crack front tooth r_z was set to 20 µm. These values correspond to the crack front and flanks microstructure on real cracked specimens. The overall geometry used for this research variant was the small specimen.
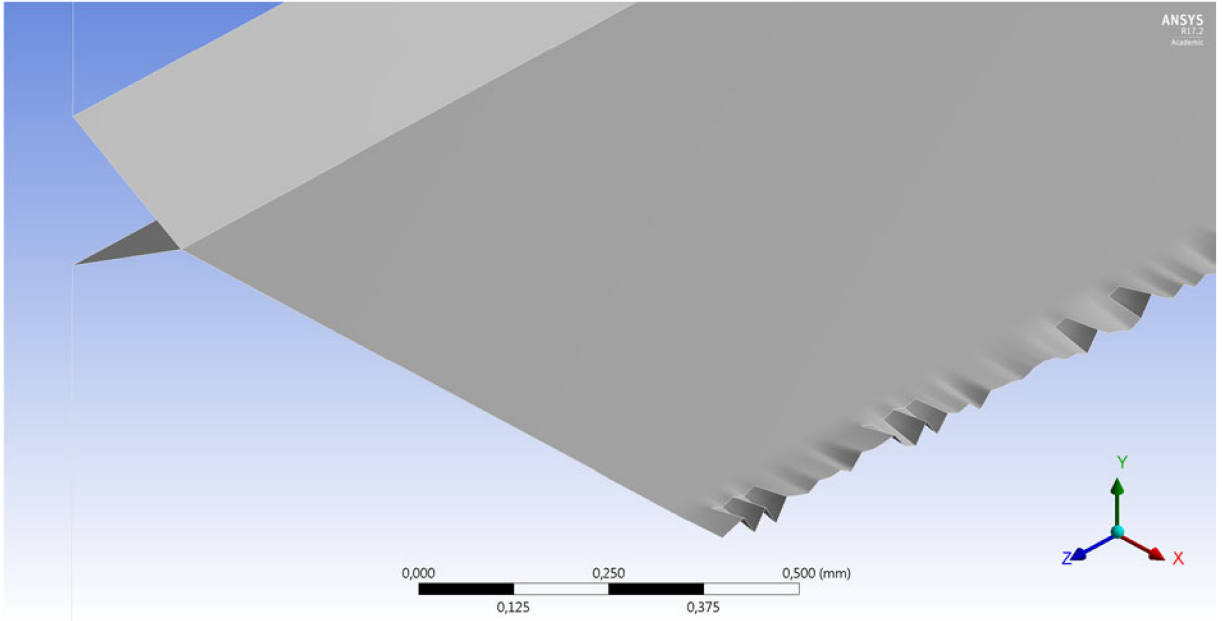
Fig. 79: Detail of tortuous crack front in FE model

The numerical model of the crack with random distribution of crack front asperities is almost the most complex model which was used in this particular research. However, a simplified analytical-based model could be used for the same purpose. To evaluate the influence of different crack front tortuosity on the fracture roughness (for very high-strength steels) under remote mode I loading an analytical solution based on stress tensor transformations was used by Pokluda et al. [10]. Hereafter, this simplified approach was adopted for the remote mode II loading.
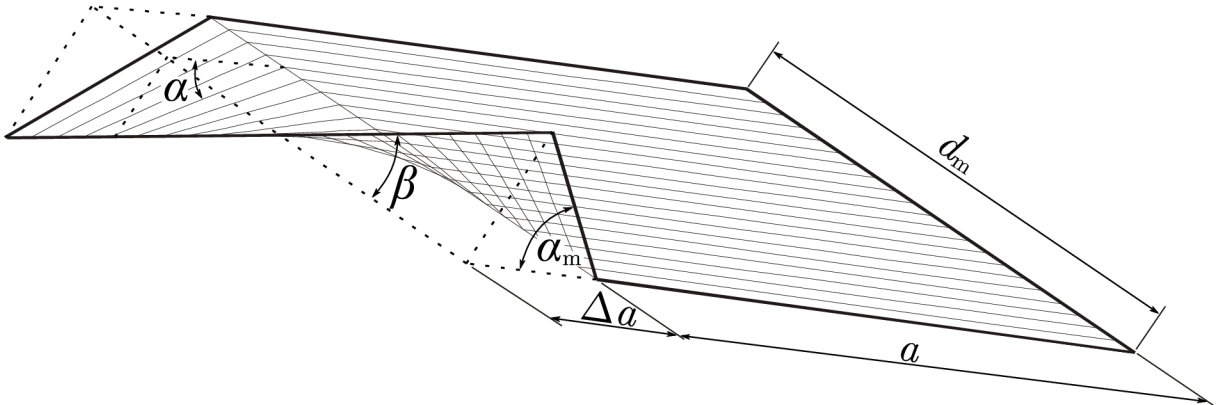
Fig. 80: Simplified model of tortuous crack geometry

Analytical model uses simplified geometry (Fig. 80) where only area between adjacent teeth peaks is considered. This model uses periodicity thus the teeth are considered the same along the whole crack front instead of statistical distribution of crack teeth geometry in FE model. The model geometry is defined by the facet (asperity) width d_m and the crack length which is divided into two parts – smooth portion of the crack with length of a and portion with crack front which is tilted and twisted at the same time and is defined by length Δa. To compare this model with the numerical

73

one these dimensions were set to match. The crack facet width d_m was 20 µm, length of the tortuous part of the crack Δa was 80 µm and the overall crack length $a + \Delta a$ was set to 22 mm. The symmetrical kink and twist of the crack front are defined by angles α and β respectively. The twist angle β can be calculated from linear roughness R_L of the crack front evaluated either from numerical model or from the real crack front subjected to stereophotogrammetrical fractography in the SEM:

$$\beta = \cos^{-1}\left(\frac{1}{R_L}\right). \tag{30}$$

From the Fig. 80 it is clearly visible that the kink angle α is a function of the position along the crack front. However, the maximal kink angle α_m can be evaluated from the twist angle and model characteristic dimensions:

$$\alpha_m = \tan^{-1}\left[\frac{d_m \cdot \tan(\beta)}{2\Delta a}\right]. \tag{31}$$

If one assumes the stress tensor $\mathbf{T}_\sigma$ components around the crack front [17] for the remote mode II loading for the plane strain conditions, smooth and long crack, normalized to external loading and overall crack and specimen geometry and with Poisson's ratio μ:

$$\sigma_{xx} = -\sin\left(\frac{\alpha}{2}\right) \cdot \left[2 + \cos\left(\frac{\alpha}{2}\right) \cdot \cos\left(\frac{3\alpha}{2}\right)\right],$$

$$\sigma_{yy} = \sin\left(\frac{\alpha}{2}\right) \cdot \cos\left(\frac{\alpha}{2}\right) \cdot \cos\left(\frac{3\alpha}{2}\right),$$

$$\sigma_{zz} = -2\mu \cdot \sin\left(\frac{\alpha}{2}\right), \tag{32}$$

$$\sigma_{xy} = \cos\left(\frac{\alpha}{2}\right) \cdot \left[1 - \sin\left(\frac{\alpha}{2}\right) \cdot \sin\left(\frac{3\alpha}{2}\right)\right],$$

$$\sigma_{xz} = \sigma_{yz} = 0,$$

the former stress tensor $\mathbf{T}_\sigma$ can be transformed to a new coordinate system related to elements of the inclined crack facet. This transformation leads to new stress tensor $\mathbf{T}_\sigma^*$:

$$\mathbf{T}_\sigma^* = \mathbf{L}^T \cdot \mathbf{T}_\sigma \cdot \mathbf{L}, \tag{33}$$

where $\mathbf{L}$ is the matrix of direction cosines for double rotation of tensor coordinate system (rotated according to kink and twist angles α and β respectively):

$$\mathbf{L} = \mathbf{L}_X \cdot \mathbf{L}_Z = \begin{vmatrix} 1 & 0 & 0 \\ 0 & \cos(\beta) & -\sin(\beta) \\ 0 & \sin(\beta) & \cos(\beta) \end{vmatrix} \cdot \begin{vmatrix} \cos(\alpha) & -\sin(\alpha) & 0 \\ \sin(\alpha) & \cos(\alpha) & 0 \\ 0 & 0 & 1 \end{vmatrix}. \tag{34}$$

From equations (32) - (34) the SIFs normalized to global loading K_{II} can be derived as components of transformed tensor $\mathbf{T}_\sigma^*$:

$$k_1 / K_{\mathrm{II}} \approx \mathbf{T}_{\sigma\,2,2}^*,$$

$$k_2 / K_{\mathrm{II}} \approx \mathbf{T}_{\sigma\,1,2}^*, \tag{35}$$

$$k_3 / K_{\mathrm{II}} \approx \mathbf{T}_{\sigma\,2,3}^*.$$

For the evaluation of global influence of crack front roughness on the mode II SIF a ratio of k_2/K_{II} as a function of angles α and β can be expressed as:

$$k_2 / K_{\mathrm{II}} (\alpha, \beta) = \left[1 - \sin\left(\frac{\alpha}{2}\right) \cdot \sin\left(\frac{3\alpha}{2}\right) \right] \cdot \cos\left(\frac{\alpha}{2}\right) \cdot \cos(2\alpha) \cdot \cos(\beta) +$$

$$+ \frac{1 + \cos^2(\beta)}{4} \cdot \sin(\alpha) \cdot \sin(2\alpha) \cdot \cos\left(\frac{3\alpha}{2}\right) + \sin\left(\frac{\alpha}{2}\right) \cdot \sin(2\alpha) \cdot \left[1 - \mu \sin^2(\beta) \right]. \tag{36}$$

Equation (36) mathematically describes the local mode II SIF component along the serrated crack front (or its one asperity) and it can be easily used to assess it with known values of R_{L}, d_{m} and Δa. For the global point of view averaged value of the ratio k_2/K_{II} along the crack front can be evaluated by following formula:

$$k_2 / K_{\mathrm{II}} = \frac{1}{2\alpha_{\mathrm{m}}} \cdot \int_{-\alpha_{\mathrm{m}}}^{\alpha_{\mathrm{m}}} k_2 / K_{\mathrm{II}} (\alpha, \beta) \, \mathrm{d}\alpha. \tag{37}$$

Similarly to this approach, Zhang and Wang [75] tried to describe the local SIFs along the crack with asymmetric kink combined with crack twist:

$$k_1^{\text{Zhang, Wang}} = k_1^{\text{Cotterell, Rice}} \cdot \cos^2(\beta),$$

$$k_2^{\text{Zhang, Wang}} = k_2^{\text{Cotterell, Rice}} \cdot \cos(\beta), \tag{38}$$

$$k_3^{\text{Zhang, Wang}} = k_1^{\text{Cotterell, Rice}} \cdot \cos(\beta) \cdot \sin(\beta),$$

where they intended to improve basic equations for the kinked crack obtained by Cotterell and Rice [76]:

$$k_1^{\text{Cotterell, Rice}} = \frac{1}{4}\left[3\cos\left(\frac{\alpha}{2}\right) + \cos\left(\frac{3\alpha}{2}\right) \right] \cdot K_{\mathrm{I}} - \frac{3}{4}\left[\sin\left(\frac{\alpha}{2}\right) + \sin\left(\frac{3\alpha}{2}\right) \right] \cdot K_{\mathrm{II}},$$

$$k_2^{\text{Cotterell, Rice}} = \frac{1}{4}\left[\sin\left(\frac{\alpha}{2}\right) + \sin\left(\frac{3\alpha}{2}\right) \right] \cdot K_{\mathrm{I}} + \frac{1}{4}\left[\cos\left(\frac{\alpha}{2}\right) + 3\cos\left(\frac{3\alpha}{2}\right) \right] \cdot K_{\mathrm{II}}, \tag{39}$$

where K_{I} and K_{II} stand for general remote mixed-mode I+II loading SIFs. If only pure remote mode II loading is assumed, the $K_{\mathrm{I}} = 0\ \mathrm{MPa \cdot m^{1/2}}$ and thus the first part of both expressions in (39) disappears. With that in mind the $k_1^{\text{Cotterell, Rice}}$ and $k_2^{\text{Cotterell, Rice}}$ can be normalized to K_{II} loading and used for evaluation of normalized local SIFs for kinked

and twisted crack by formula (38). However, comparison of approaches (38) and (37) shows that both ways of evaluation of local SIFs give slightly different results. The difference may be caused by slightly different type of kink and twist used by Zhang and Wang [75] and also due to some (in quoted paper not sufficiently described) simplifications in [75]. Because of these ambiguities and better resemblance of used model (Fig. 80) only the approach based on simple stress tensor transformations (equations (30) - (37)) will be used in this research.

Above mentioned approaches (analytical and numerical) can be compared with each another and also, they can be used to evaluate the decrease of mode II SIF caused by the crack front tortuosity. The decrease of relevant SIF can be described by the ratio k_2/K_{II} from analytical model (see formula (37)) or by the quotient Q_{II} obtained from numerous numerical simulations of similar crack configuration (coefficient Q_{II} describes the ratio of local values of k_{II} along the tortuous crack front and function $K_{II}(z)$ along the straight crack front, actual method of obtaining of Q_i for any crack mode SIF was described in chapter 4.2.1.4). For this type of loading the coefficient Q_{II} and ratio k_2/K_{II} describe the same ratio so they can be directly compared.

In the numerical model a statistical distribution of the crack front asperities was employed with fixed values of crack geometry dimensions (according to Fig. 80) $d_m = 20$ μm, $\Delta a = 80$ μm and $a + \Delta a = 22$ mm. These fixed values were also used for analytical model. The only difference in used geometries of the crack front and flanks is that for numerical model a different height of each crack front tooth was used along the crack front and for each statistical pass of calculations. The only restriction was to keep the geometry with desired mean linear crack front roughness R_L. Two variants of such a statistical set of numerical models were evaluated with final mean R_L at 1.078 and 1.261. The analytical model was than adjusted to match values of d_m, Δa and overall crack length and the angles α_m and β were consecutively evaluated from mentioned R_L values with use of equations (31) and (30) respectively.

Table 2: Evaluated ratios of mode II SIF and comparison of used models

	$R_{L,1} = 1.078$	$R_{L,2} = 1.261$
k_2/K_{II} (analytical model)	0.9270	0.7912
Q_{II} (numerical model)	0.8981	0.7588
Relative deviation between models	3.12 %	4.10 %

There is a good agreement between analytical and numerical models. Despite the difference in terms of uniform contra statistical distribution of the crack front asperities the relative deviation between the two averaged ratios is for both crack front roughnesses under 5 %.

If we consider the results in Table 2, the experimentally measured effective fatigue threshold SIFs can be corrected if the real linear roughness of pre-crack front is estimated. Previously measured fatigue threshold of mode II crack propagation was evaluated by Vojtek et al. for the polycrystalline ARMCO iron and cyclic ratio $R = 0.1$ and it was

quantified as $\Delta K_{\text{IIth, eff}} = 1.5\,\text{MPa} \cdot \text{m}^{1/2}$ [77]. The linear roughness of pre-cracks in broken specimens was evaluated by stereophotogrammetrical analysis of SEM data and it was calculated to be $R_{\text{L, Fe}} \approx 1.2$ (by averaging several typical crack topologies). If both numerical and analytical models are taken into account, the geometrical shielding can be calculated by linear interpolation from k_2/K_{II} (analytical model):

$$k_2 / K_{\text{II}}\left(R_{\text{L, Fe}}\right) = k_2 / K_{\text{II}}\left(R_{\text{L, 1}}\right) + \left(R_{\text{L, Fe}} - R_{\text{L, 1}}\right) \frac{k_2 / K_{\text{II}}\left(R_{\text{L, 2}}\right) - k_2 / K_{\text{II}}\left(R_{\text{L, 1}}\right)}{R_{\text{L, 2}} - R_{\text{L, 1}}} =$$

$$= 0.9270 + \left(1.2 - 1.078\right) \frac{0.7912 - 0.927}{1.261 - 1.078} = 0.8365,$$

(40)

and from Q_{II} (numerical model):

$$Q_{\text{II}}\left(R_{\text{L, Fe}}\right) = Q_{\text{II}}\left(R_{\text{L, 1}}\right) + \left(R_{\text{L, Fe}} - R_{\text{L, 1}}\right) \frac{Q_{\text{II}}\left(R_{\text{L, 2}}\right) - Q_{\text{II}}\left(R_{\text{L, 1}}\right)}{R_{\text{L, 2}} - R_{\text{L, 1}}} =$$

$$= 0.8981 + \left(1.2 - 1.078\right) \frac{0.7588 - 0.8981}{1.261 - 1.078} = 0.8052,$$

(41)

where $R_{\text{L, 1}}$ is the lower and $R_{\text{L, 2}}$ is the higher calculated fracture roughness (see Table 2). With use of evaluated correction factors (formulas (40) and (41)) the experimentally measured value of $\Delta K_{\text{IIth, eff}}$ decreases to $1.25\,\text{MPa} \cdot \text{m}^{1/2}$ with use of analytical model and even to value of $1.21\,\text{MPa} \cdot \text{m}^{1/2}$ with use of more precise, numerical model.

The corrected value of $\Delta K_{\text{IIth, eff}}$ can be compared with theoretical value $K_{\text{IIe}} = 0.7\,\text{MPa} \cdot \text{m}^{1/2}$, related to the emission of dislocations in the cracked iron single crystal, obtained from multiscale quasi-continuum models [78], but with respect to research of dislocation models of fatigue crack propagation by Riemelmoser et al. [79] it must be kept in mind that dislocation models give results 1.3 times lower than the experimental measurement. With use of the 1.3 factor and geometrical correction by the results of numerical model of tortuous crack the measured mode II threshold value is decreased to $\Delta K_{\text{IIth, eff, e}} = 0.93\,\text{MPa} \cdot \text{m}^{1/2}$, which is closely approaching the theoretical threshold. This evaluated correction of experimental threshold value (by the geometry of crack front) can connect the experiments with theoretically predicted numbers by multiscale models.

4.2.2.4 Fully random crack front

The last investigated type of the crack front tortuosity was combination of kinked/twisted crack (see chapter 4.2.2.3) with in-plane tortuosity. This particular type of simulation was created to look into the influence of fully random crack front shape. Moreover, two types of material models were used here to check the influence of material parameters (mainly Poisson's ratio μ and respective lateral contraction of material). Presented results are the summarization of gradual research on this topic which was progressively published by the author of this thesis in several journal papers (see e.g. [38, 39, 80, 81]).

This crack shape was achieved by use of all parameters in the simulation according to Fig. 61 in chapter 4.2.1.2. For this type the large specimen was used. The tilt length s_r was set to be constant to 1 mm and the crack tortuosity parameter r_z was constant for each simulation along the crack front too. The other two parameters r_x and r_y were again randomly distributed along the crack front and thus they formed different crack front shapes for each simulation.

Used two material models were both linear-elastic with the same Young's modulus E but with different Poisson's ratio μ which was set to 0.3 (as for iron and other metallic materials) in standard material model and to 0 (to diminish the lateral contraction of material) in so-called artificial material model.

Evaluated results from the large specimen with above described geometry were again all three SIFs along the crack front which were normalized to loading and specimen geometry (according to equation (29) in chapter 4.2.1.3). At first, the difference between two used material models was quantified by comparison of the results from model with standard planar crack.
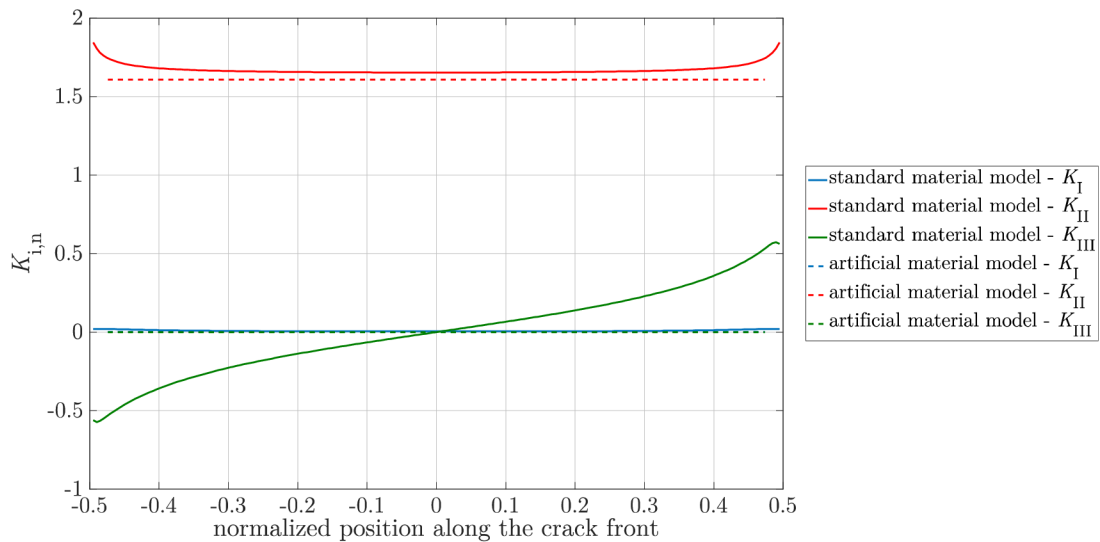
Fig. 81: Comparison of resulting normalized SIFs for standard and artificial material model (straight, planar crack)

From the comparison of two material models for simulation with planar crack (Fig. 81) one can see some differences between results, despite the fact that generally the material model should not affect resulting SIFs. Obviously for both cases mode I SIF is negligible, for artificial material model it is 0 along the whole crack front and for standard material model the $K_{\mathrm{I,n}}$ exhibits small increase towards the sides of the specimen but the increase is still insignificant in comparison with other SIFs. On the other hand, the mode II SIF is for both cases dominant (as expected). Standard material model exhibits a slight increase of $K_{\mathrm{II,n}}$ at the sides of specimen which is consistent with results obtained from small specimen (see Fig. 67 in chapter 4.2.1.3) and free surface effect reported by Pook [6], where the artificial material model, lacking the lateral contraction of material, shows completely constant value of mode II SIF. A small difference between mean values of mode II SIFs progressions of standard and artificial model can be explained by overall change in specimen deformations due to use of force loading combined with differences in material models. Nevertheless, the difference between mean values of $K_{\mathrm{II,n}}$ for both models is negligible - less than 4%. The greatest difference between the two models is in the mode III SIF. One can see that while standard material model shows increase of $K_{\mathrm{III,n}}$ towards the sides of the specimen up to value of approximately one third of $K_{\mathrm{II,n}}$ (again consistently with findings summarized by Pook [6]), the simulation with artificial material model excludes the mode III at all. This shows that with CTS specimen only center portion of the crack front is under pure mode II loading (even with remote mode II loading) for real-like materials (depending on Poisson's ratio).
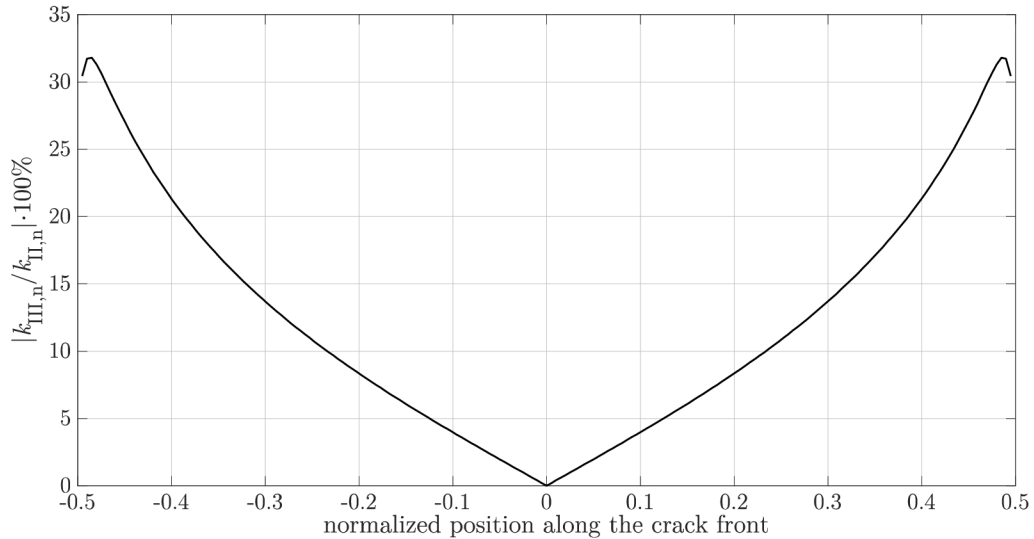
Fig. 82: Relative difference between mode II and III SIFs (straight crack, standard material model)

The percentual representation of the ratio $k_{\mathrm{III,n}}$ to $k_{\mathrm{II,n}}$ (Fig. 82) for used model configuration (large CTS specimen geometry and $\mu = 0.3$) the mode III SIF indeed exhibits increase more than 30% of mode II SIF at the sides of the specimen. But at one fourth of the specimen thickness (normalized position ± 0.25) the relative difference is decreased to 10% and decreasing towards 0 difference in the middle of the specimen. Moreover, the $K_{\mathrm{II,n}}$ for standard model is almost along the whole crack front constant and thus it can be used for purposes of this research.

Each result set of actual statistically rough crack fronts was characterized by surface roughness R_{S}:

$$R_{\mathrm{S}} = \frac{S_{\mathrm{R}}}{S}, \tag{42}$$

where S_{R} is the surface area of crack flanks of rough crack and S is the surface area of the projection of rough crack flanks to x-z plane. The surface roughness according to equation (42) was used instead of previously used linear roughness R_{L} because this crack front type is tortuous in all directions and surface roughness better describes the tortuosity of the crack.

With known values of SIFs for standard planar model the results from modified model with tortuous crack geometry can be compared with them. The results comparison was made with use of quotient Q_{i} (where i = II and III for respective modes, for detailed description of coefficient Q_{i} see chapter 4.2.1.4) The significant values were for mode II SIF (Q_{II}), because the value of $K_{\mathrm{I,n}}$ was oscillating around 0 value for both used material models thus the coefficient Q_{I} equaled for all cases 1. The other evaluated quotient was Q_{III} for mode III SIF, but only for simulations with standard material model because with use of artificial material model with $\mu = 0$ the $K_{\mathrm{III,n}}$ oscillated around 0 value and no reasonable values of Q_{III} could be evaluated with use of artificial material model.
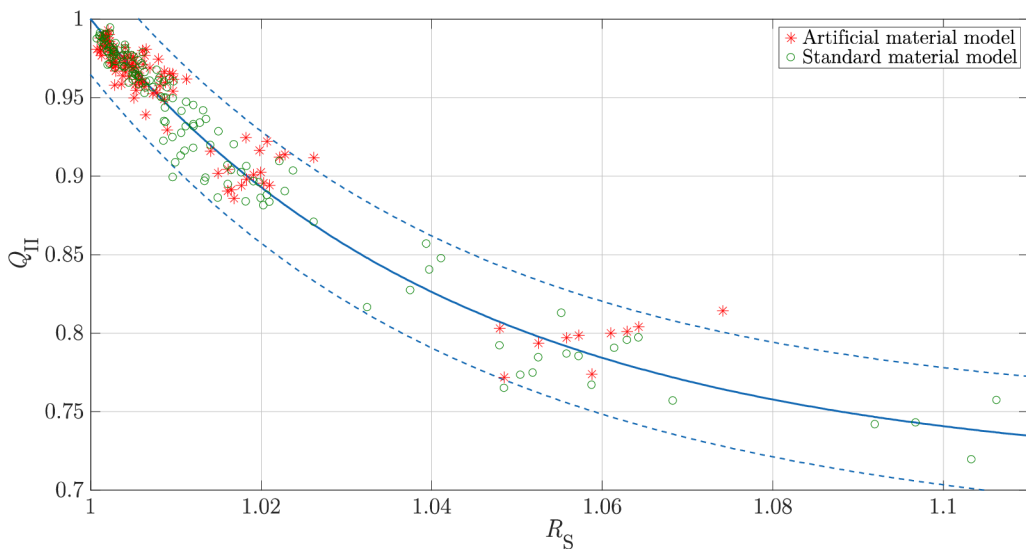
Fig. 83: Coefficient Q_{II} as a function of crack flanks roughness R_S
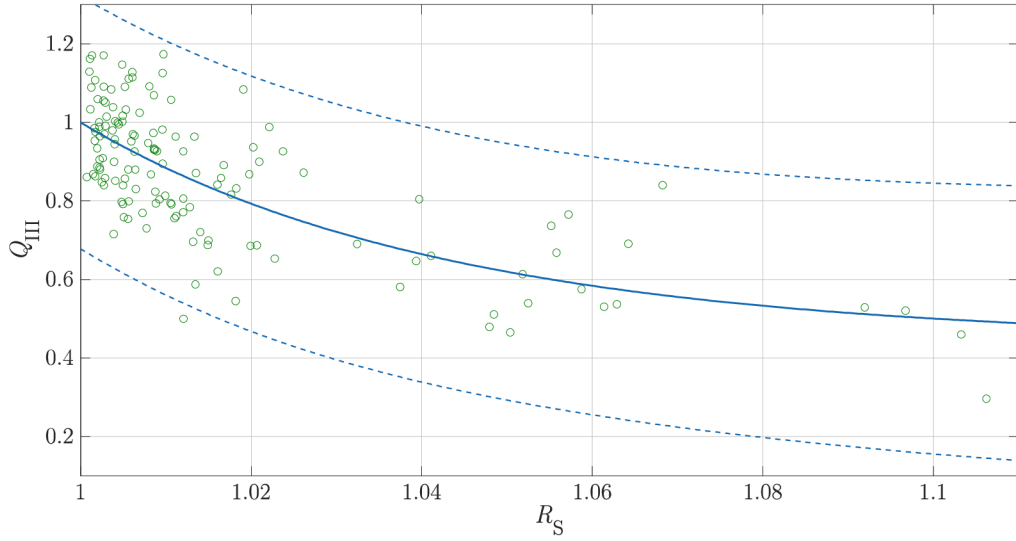
Fig. 84: Coefficient Q_{III} as a function of crack flanks roughness R_S

Obtained coefficients Q_{II} and Q_{III} as functions of crack roughness R_S are depicted in Fig. 83 and Fig. 84 respectively, whereas the results from artificial and standard material models for Q_{II} are differentiated by red star signs and green circles respectively, but as can be seen in Fig. 83 both models give similar results so in the next processing the results from both models are treated collectively. The full blue line in each chart represents the interpolation of data-points $Q_{II}(R_S)$ or $Q_{III}(R_S)$ by a power-law function:

$$Q_i\left(R_S\right) = A_i \cdot R_S^{-B_i} + C_i; \quad \text{where i = II or III.} \tag{43}$$

The coefficients of simple interpolation function (43) had to be constrained to let the actual interpolation function satisfy the condition $Q_i(R_S = 1) = 1$, which leads to used function:

$$Q_i\left(R_S\right) = A_i \cdot R_S^{-B_i} + 1 - A_i; \quad \text{where i = II or III,} \tag{44}$$

where only two independent fitting coefficients A_i and B_i are present.

The constrained function (44) was used for interpolation of results for the mode II (both standard and artificial model combined) and mode III loading with use of least square method built in the Matlab code [71]. The blue dashed lines limit the 99% confidence interval obtained by used interpolation method. Interpolation coefficients alongside with R-square parameter of each interpolation are shown in a table below.

Table 3: Interpolation coefficients

	A_i	B_i	R^2
mode II	0.2914	23.13	0.9533
mode III	0.5606	23.26	0.5272

As was mentioned before, resulting coefficients Q_{II} for standard and artificial models are very close to each other which shows that lateral contraction and the side effect on the CTS specimen have very small, almost insignificant impact on observed changes of the mode II SIF. After such observation, both result sets from simulations with standard and artificial material model were joined together.

Resulting coefficients Q_{II} and Q_{III} show significant decrease of averaged mode II and mode III SIFs along the tortuous crack fronts with increase of the crack flanks roughness. This result is in good agreement with theory describing roughness-induced shielding which was observed and investigated for mode I loading (e.g. [9, 10, 49–52]). Moreover, this phenomenon is in consistence with previous findings from models with simpler crack front and flanks geometries described in chapters above. These results for completely randomized crack front shape show that the decrease corresponds to power-law function of crack flanks roughness R_S (44). The power-law function fit for $Q_{II}(R_S)$ is very good (as is quantified by its R-square in Table 3) and also the 99% confidence bounds in Fig. 83 are quite narrow. This points out to a very small scattering even if used input parameters are randomly distributed. The $Q_{III}(R_S)$ on the other hand shows large scattering (wide 99% confidence bounds) and a mediocre quality of function fit. Large variance of the Q_{III} results can be caused by higher sensitivity of mode III on small changes in the crack front and flanks geometry and also by higher oscillation of local $k_{3,n}$ components around their mean functional value.

It is interesting that both interpolation functions (mode II and III) have almost the same B_i coefficient. This points out that the rate of decrease of both mean K_{II} and K_{III} is the same. Also constructed function for mode II shows signs of some convergence to critical value of $Q_{II,c}$ where the mean value of K_{II} is not dependent on crack flanks roughness R_S. The same observation can be seen for mode III. The critical values can be theoretically obtained as a horizontal asymptotes of used interpolation functions. The function (43) can be rewritten to a rational form:

$$Q_i\left(R_S\right) = \frac{C_i \cdot A_i \cdot R_S^{B_i} + 1}{A_i \cdot R_S^{B_i}}; \quad \text{where i = II or III,} \tag{45}$$

in which obviously the degrees of numerator and denominator are the same. For such a type of function (exactly as in (45) and with the same degrees of numerator and denominator) the horizontal asymptote equals coefficient C_i [82]. According to equation (44) the coefficient C_i equals to $1 - A_i$ thus the horizontal asymptotes of used functions are dependent only on coefficient A_i which is different for each mode. If one assumes that used interpolations are correct, then the critical values $Q_{II,c}$ and $Q_{III,c}$ should be 0.7083 and 0.4394 respectively, whereas the critical value of $Q_{II,c}$ is more important due to the fact that the mode II loading is applied and evaluated. This means that in case of similar crack front and flanks geometry (as in Fig. 79) even for very high values of R_S the mean value of mode II SIF should not decrease below 70% of applied $K_{II,app}$.

5 Conclusions

During Ph.D. research presented in this dissertation thesis new modelling approaches were used for a description of fracture behavior of cracks with rough crack flanks and tortuous crack fronts. Several phenomena related to geometrically induced shielding for shear modes loading were described and some of them were applied in relation to experimental measurement of fatigue threshold values for metallic materials. The research results were gradually published in scientific journals and presented on national and international conferences. For a better comprehension of research outputs, the conclusions discussed in this chapter will be referenced to each respective publication (or presentation) listed in chapter 8 (indicated by a roman numeral in square brackets), where actual findings were published.

Research described in this dissertation thesis confirmed the influence of crack front microstructure and it extended the knowledge about geometrical shielding on shear modes where it was not investigated as much as for loading mode I. For this purpose, two types of specimens were investigated – cylindrical specimen and CTS specimen. Modeled loading regimes were only shear modes (both II and III) and a new aspect was introduced to specimens' models – crack front and flanks tortuosity.

For the cylindrical specimen two distinct phenomena were investigated. The first one was related to simplifications of complicated numerical models of fractures with complex shapes. Performed calculations revealed that it is not necessary to model the whole specimen with tortuous crack front, but one can model in detail a very small part of the crack around the place of interest, but in the rest of the model the crack front and flanks can be modeled as a simplified plane without influencing desired results. In fact, for sufficient accuracy of resulting SIFs along any asperity on crack front only one or two additional asperities have to be modeled on each side of the region of interest [V, XVIII]. This finding can help in acceleration of calculations of future models of cracks with tortuous front where only a small portion of actual fracture is investigated.

The second thing related to the cylindrical specimen in this research was actual quantification of local k_2 influence on crack propagation under remote mode III loading. It was shown that for in-plane zig-zag shaped crack fronts the induced local k_2 along each asperity is strongly dependent on actual asperity angle – mode II inducement increases with higher asperity angles and for angles larger than 15° the induced k_2 is not constant along the whole crack tooth but it increases towards the crack tooth peak. Comparison of numerically modeled ratios of k_2/K_{III} with experimentally measured ratios of fatigue threshold values for modes II and III (when related to correct mean asperity angles measured by SEM on real pre-cracks) showed that modeled ratios of k_2/K_{III} corelates with threshold values well and thus the local mode II crack advances under remote mode III loading could be quantified [VI, X, XVI] for ARMCO iron and Niobium.

For the CTS specimen under remote mode II loading the influence of several crack front and flanks roughnesses were investigated. Using only numerical FE models

a decrease of mean $k_2(z)$ value in comparison with applied $K_{II, app}$ was quantified by quotient Q_{II} for in-plane and out-of-plane crack roughness and also for their combination. This quantification revealed that the in-plane crack front tortuosity has much larger influence on the mode II SIF decrease than the out-of-plane tortuosity [VIII, XX]. Overall decrease of mode II SIF can be used to correct experimentally measured values of SIFs if the real crack asperity mean angles are known. The same simulations were used to investigate local modes inducement along one particular asperity. For in-plane crack front tortuosity qualitatively the same result as for cylindrical specimen was observed, but with locally induced k_3 in relation to global K_{II} [VIII, XX]. On the other hand, for the out-of-plane tortuosity, despite no obvious reason, mode I SIF was induced along each particular crack front asperity. Closer observation of this phenomenon showed that the small amount of induced k_1 can be clarified – small tensile and compressive stresses were just a local perturbation resulting from accurate numerical model and they have no direct connection to crack front rotation [VIII, XX].

The last step in modelling of complex crack front shape was to create model where only a small portion of crack length is rough, and the rest is planar. This corresponds to experimentally observed crack morphologies where part of a crack was created ultra-fine and planar on purpose but the rest, after some shear crack propagation, exhibited some roughness. For the investigation of this type of shear cracks both numerical and analytical models with combination of crack front kink and twist were introduced. Analytical model included several simplifications, but the numerical model included random crack front shape (governed by mean R_L-value). Comparison of both approaches led to the conclusion that both approaches can describe the decrease of mean k_2 value very well. In fact, the resulting coefficients Q_{II} were used to correct experimentally measured fatigue threshold value for ARMCO iron (measured under the assumption of straight crack front) and to corelate the threshold value with theoretical multiscale quasi-continuum models [VII]. Moreover, overall decrease of mean values of SIFs for this type of crack front and flanks geometry was quantified and related to crack geometrical shielding effect [III-V, XIII, XIV, XV, XVII]. One particular part of presented research showed that the decrease of mean value of $k_2(z)$ with increasing crack front and flanks roughness is independent on all linear material properties (despite the fact that the Poisson's ratio influences overall progression of K_{II} and K_{III}).

In conclusion, advances in presented research helped mainly in the path for correction of experimentally measured SIFs to the real crack front microstructure for remote shear loading. Newly used coefficient Q_i can be used for such correction when the actual crack front and flanks roughness is known. In addition, new models of shear cracks (statistical approach in FE models and one new analytical model) enable new possibilities in this branch of research. These new models can be used in further research in correlation with more experimental results. Furthermore, the same approach as was used here in FE modelling can be extended for different, more complicated crack flanks geometries and even create models as exact copies of SEM observed crack morphologies.

6 References

[1]   Vojtek, T., Pokluda, J.: Experimental Investigation of Modes II and III Fatigue
        Crack Growth in Unalloyed Titanium. Key Eng. Mater. 592–593, 797–800 (2013).
        doi: 10.4028/www.scientific.net/KEM.592-593.797

[2]   Roylance, D.: Introduction to Fracture Mechanics. 32, 1–17 (2001).
        doi:10.2472/jsms.32.935

[3]   Irwin, G.R., Kies, J.A.: Fracturing and Fracture Dynamics. Weld. J. Res. Suppl.
        (1952)

[4]   Irwin, G.R., Kies, J.A.: Critical Energy Rate Analysis of Fracture Strength
        of Large Welded Structures. Weld. J. Res. Suppl. (1954)

[5]   Rice, J.R.: A Path Independent Integral and the Approximate Analysis of Strain
        Concentration by Notches and Cracks. J. Appl. Mech. 35, 379 (1968).
        doi: 10.1115/1.3601206

[6]   Pook, L.P.: A 50-year retrospective review of three-dimensional effects at cracks
        and sharp notches. Fatigue Fract. Eng. Mater. Struct. 36, 699–723 (2013).
        doi: 10.1111/ffe.12074

[7]   Vojtek, T., Pokluda, J., Hohenwarter, A., Pippan, R.: Three-dimensional
        morphology of fracture surfaces generated by modes II and III fatigue loading
        in ferrite and austenite. Eng. Fract. Mech. 108, 285–293 (2013).
        doi: 10.1016/j.engfracmech.2013.02.022

[8]   Vojtek, T., Žák, S., Pokluda, J.: On the connection between mode II and mode
        III effective thresholds in metals. Fract. Struct. Integr. 41, 245–251 (2017).
        doi: 10.3221/IGF-ESIS.41.33

[9]   Pokluda, J., Šandera, P., Horníková, J.: Statistical model of roughness-induced
        crack closure. In: Fuentes, M., Martin-Meizoso, A., and Martinez-Esnaola, M.
        (eds.) Fracture Mechanics: Applications and Challenges. Elsevier, Amsterdam
        (2000)

[10]   Pokluda, J., Šandera, P., Horníková, J.: Statistical approach to roughness-
        induced shielding effects. Fatigue Fract. Eng. Mater. Struct. 27, 141–157 (2004).
        doi: 10.1111/j.1460-2695.2004.00734.x

[11]   Bechtle, S., Fett, T., Rizzi, G., Habelitz, S., Schneider, G. a.: Mixed-mode stress
        intensity factors for kink cracks with finite kink length loaded in tension and
        bending: Application to dentin and enamel. J. Mech. Behav. Biomed. Mater. 3,
        303–312 (2010). doi: 10.1016/j.jmbbm.2009.12.004

[12]   Benedetti, M., Fontanari, V., Monelli, B.D., Beghini, M.: A Fully Parametric
        Weight Function for Inclined Kinked Edge Cracks. Procedia Mater. Sci. 3,
        1371-1376 (2014). doi: 10.1016/j.mspro.2014.06.221

[13] Pant, M., Singh, I. V., Mishra, B.K.: A novel enrichment criterion for modeling kinked cracks using element free Galerkin method. Int. J. Mech. Sci. 68, 140–149 (2013). doi: 10.1016/j.ijmecsci.2013.01.008

[14] Pokluda, J., Kroupa, F., Obdržálek, L.: Mechanické vlastnosti a struktura pevných látek: kovy – keramika – plasty. 1ˢᵗ edition. PC-DIR spol. s.r.o. - Nakladatelství, Brno (1994). ISBN: 80-214-0575-9

[15] Irwin, G.R.: Analysis of Stresses and Strains Near the End of a Crack Traversing a Plate. J. Appl. Mech. 24, 361–364 (1957)

[16] Tada, H., Paris, P.C., Irwin, G.R.: The Stress Analysis Handbook of Cracks Handbook. American Society of Mechanical Engineers,U.S., Farfield (2000)

[17] Anderson, T.L.: Fracture mechanics: Fundamentals and applications. CRC Press, Boca Raton (Florida) (1995). ISBN: 9781420058215

[18] Ansys Inc.: Ansys R17.2 help (user's manual), (2016)

[19] Henshell, R.D., Shaw, K.G.: Crack tip finite elements are unnecessary. Int. J. Numer. Methods Eng. 9, 495–507 (1975). doi: 10.1002/nme.1620090302

[20] Barsoum, R.S.: On the use of isoparametric finite elements in linear fracture mechanics. Int. J. Numer. Methods Eng. 10, 25–37 (1976). doi: 10.1002/nme.1620100103

[21] Barsoum, R.S.: Triangular quarter-point elements as elastic and perfectly-plastic crack tip elements. Int. J. Numer. Methods Eng. 11, 85–98 (1977). doi: 10.1002/nme.1620110109

[22] Shih, C.F., Moran, B., Nakamura, T.: Energy release rate along a three-dimensional crack front in a thermally stressed body. Int. J. Fract. 30, 79–102 (1986). doi: 10.1007/BF00034019

[23] Valvo, P.S.: A revised virtual crack closure technique for physically consistent fracture mode partitioning. Int. J. Fract. 173, 1–20 (2012). doi: 10.1007/s10704-011-9658-y

[24] Fawaz, S.A.: Application of the virtual crack closure technique to calculate stress intensity factors for through cracks with an elliptical crack front. Eng. Fract. Mech. 59, 327–342 (1998). doi: 10.1016/S0013-7944(97)00126-4

[25] Tschegg, E.K.: The influence of the static I load mode and R ratio on mode III fatigue crack growth behaviour in mild steel. Mater. Sci. Eng. 59, 127–137 (1983). doi: 10.1016/0025-5416(83)90094-0

[26] Pook, L.P.: The fatigue crack direction and threshold behaviour of mild steel under mixed mode I and III loading. Int. J. Fatigue. 7, 21–30 (1985). doi: 10.1016/0142-1123(85)90004-0

[27] Brown, M.W., Hay, E., Miller, K.J.: Fatigue at Notches Subjected to Reversed Torsion and Static Axial Loads. Fatigue Fract. Eng. Mater. Struct. 8, 243–258 (1985). doi: 10.1111/j.1460-2695.1985.tb00425.x

[28] Hellier, A., Corderoy, D., McGirr, M.: A practical mixed Mode II/III fatigue test rig. Int. J. Fatigue. 9, 95–101 (1987). doi: 10.1016/0142-1123(87)90050-8

[29] Doquet, V., Bui, Q.H., Bertolino, G., Merhy, E., Alves, L.: 3D shear-mode fatigue crack growth in maraging steel and Ti-6Al-4V. Int. J. Fract. 165, 61–76 (2010). doi: 10.1007/s10704-010-9504-7

[30] Beretta, S., Foletti, S., Valiullin, K.: Fatigue strength for small shallow defects/cracks in torsion. Int. J. Fatigue. 33, 287–299 (2011). doi: 10.1016/j.ijfatigue.2010.08.014

[31] Richard, H.A., Benitz, K.: A loading device for the creation of mixed mode in fracture mechanics. Int. J. Fract. 22, R55–R58 (1983). doi: 10.1007/BF00942726

[32] Richard, H.A.: A new compact shear specimen. Int. J. Fract. 17, R105–R107 (1981). doi: 10.1007/BF00033347

[33] Li, Q.F., Qi, G.Y., Yan, S.Y., Buchholz, F.G.: Computational Fracture Analyses of a Compact Tension Shear (CTS) Specimen with an Inclined Crack Plane. Key Eng. Mater. 385–387, 741–744 (2008). doi: 10.4028/www.scientific.net/KEM.385 387.741

[34] Li, Q.F., Qi, G.Y., Buchholz, F.G., Yan, S.Y.: Computational Fracture Analyses of a Compact Tension Shear (CTS) Specimen with an Inclined Crack Front, (2008). doi: 10.4028/www.scientific.net/KEM.385-387.741

[35] Pokluda, J., Trattnig, G., Martinschitz, C., Pippan, R.: Straightforward comparison of fatigue crack growth under modes II and III. Int. J. Fatigue. 30, 1498–1506 (2008). doi: 10.1016/J.IJFATIGUE.2007.09.009

[36] Vojtek, T., Pippan, R., Hohenwarter, A., Holáň, L., Pokluda, J.: Near-threshold propagation of mode II and mode III fatigue cracks in ferrite and austenite. Acta Mater. 61, 4625–4635 (2013). doi: 10.1016/j.actamat.2013.04.033

[37] Horníková, J., Žák, S., Šandera, P.: K-calibration of special specimens for mode II, III and II+III crack growth. Eng. Fract. Mech. 110, 430–437 (2013). doi: 10.1016/j.engfracmech.2013.08.013

[38] Horníková, J., Šandera, P., Žák, S., Pokluda, J.: Specimens for Simultaneous Mode II, III and II+III Fatigue Crack Propagation: Elasto-Plastic Solution of Crack Tip Stress-Strain Field. Adv. Mater. Res. 891–892, 1585–1590 (2014). doi: 10.4028/www.scientific.net/AMR.891-892.1585

[39]   Horníková, J., Žák, S., Šandera, P.: Numerical Fracture Analysis of Compact Tension Shear (CTS) Specimens with Tortuous Crack Fronts. Key Eng. Mater. 665, 77–80 (2015). doi: 10.4028/www.scientific.net/KEM.665.77

[40]   Žák, S., Horníková, J., Šandera, P., Pokluda, J.: Verification of Linear Dependence of Plastic Zone Size on J-Integral for Mixed-Mode Loading. Appl. Mech. Mater. 751, 15–20 (2015). doi: 10.4028/www.scientific.net/AMM.751.15

[41]   Plank, R., Kuhn, G.: Fatigue crack propagation under non-proportional mixed mode loading. Eng. Fract. Mech. 62, 203–229 (1999).
doi: 10.1016/S0013-7944(98)00097-6

[42]   Vojtek, T.: Propagation of Fatigue Cracks under Shear Loading Modes II, III and II+III in the Near-threshold Region. Brno: Vysoké učení technické v Brně, Fakulta strojního inženýrství, 2014. 72 p. Supervisor of the dissertation thesis prof. RNDr. Jaroslav Pokluda, CSc.

[43]   Benthem, J.P., Koiter, W.T.: Asymptotic approximations to crack problems in mechanics of fracture. Methods Anal. Solut. Crack Probl. 131–178 (1973).
doi: 10.1007/978-94-017-2260-5_3

[44]   Noda, N.A., Takase, Y.: Generalized stress intensity factors of V-shaped notch in a round bar under torsion, tension, and bending. Eng. Fract. Mech. 70, 1447–1466 (2003). doi: 10.1016/S0013-7944(02)00115-7

[45]   Suresh, S.: Crack deflection: Implications for the growth of long and short fatigue cracks. Metall. Trans. A. 14, 2375–2385 (1983). doi: 10.1007/BF02663313

[46]   Ritchie, R.O.: Mechanisms of fatigue crack propagation in metals, ceramics and composites: Role of crack tip shielding. Mater. Sci. Eng. 103, 15–28 (1988).
doi: 10.1016/0025-5416(88)90547-2

[47]   Kobayashi, A.S., Wade, B.G., Bradley, W.B., Chiu, S.T.: Crack branching in Homalite-100 sheets. Eng. Fract. Mech. 6, 81–92 (1974).
doi: 10.1016/0013-7944(74)90048-4

[48]   Kitagawa, H., Yuuki, R., Ohira, T.: Crack-morphological aspects in fracture mechanics. Eng. Fract. Mech. 7, 515–529 (1975).
doi: 10.1016/0013-7944(75)90052-1

[49]   Suresh, S., Ritchie, R.O.: A geometric model for fatigue crack closure induced by fracture surface roughness. Metall. Trans. A. 13, 1627–1631 (1982).
doi: 10.1007/BF02644803

[50]   Suresh, S.: Fatigue of Materials. 2nd edition. Cambridge University Press (1998).
doi: 10.1017/CBO9780511806575

[51]   Llorca, J.: Roughness-induced fatigue crack closure: A numerical study. Fatigue Fract. Engng. Mater. Struct. 655–669 (1992).
doi: 10.1111/j.1460-2695.1992.tb01304.x

[52]   Wang, S.H., Muller, C.: Analytical evaluation and experimental study of roughness-induced crack closure. In: Wu, X.R. and Wang, Z.G. (eds.) Fatigue 99. pp. 539–544. , Beijing (1999)

[53]   Gross, T.S., Mendelsohn, D.A.: Mode I Stress Intensity Factors Induced by Fracture Surface Roughness under Pure Mode III Loading : Application to the Effect of Loading Modes on Stress Corrosion Crack Growth. Metall. Trans. A. 20, (1989)

[54]   Vaziri, A., Nayeb-Hashemi, H.: The effect of crack surface interaction on the stress intensity factor in Mode III crack growth in round shafts. 72, 617–629 (2005). doi: 10.1016/j.engfracmech.2004.03.014

[55]   Gates, N., Fatemi, A.: Friction and roughness induced closure effects on shear-mode crack growth and branching mechanisms. Int. J. Fatigue. 92, 442–458 (2016). doi: 10.1016/j.ijfatigue.2016.01.023

[56]   Vojtek, T., Pokluda, J., Hohenwarter, A., Pippan, R.: Progress in understanding of intrinsic resistance to shear-mode fatigue crack growth in metallic materials. Int. J. Fatigue. (2016). doi: 10.1016/j.ijfatigue.2016.01.009

[57]   Janíček, P., Ondráček, E., Vrbka, J.: Mechanika těles: Pružnost a pevnost I. SNTL - Nakladatelství technické literatury, Praha (1987)

[58]   Bhaskar, K., Varadan, T.K.: Theory of isotropic/orthotropic elasticity: an introductory primer. Ane Books India (2009). ISBN: 9789380156200

[59]   Hwu, C.: Anisotropic elastic plates. Springer (2010). ISBN: 978-1-4419-5915-7

[60]   Schoenborn, K.: Fatigue Analysis of a Welded Assembly Using ANSYS Workbench Environment. October. (2006)

[61]   Krasovskyy, A., Sönnichsen, S., Bachmann, D.: On the residual stresses in multi-pass welds: coupling of welding simulation and fatigue analysis. Procedia Eng. 10, 506–511 (2011). doi: 10.1016/J.PROENG.2011.04.085

[62]   Chakraborty, P., Sabharwall, P., Sener, K., Varma, A.H., Spears, R.E., Coleman, J.: Modeling and Simulation of Used Nuclear Fuel During Transportation with Consideration of Hydride Effects and Cyclic Fatigue. 1–47 (2015). FCRD-UFD-2015-000273 INL/EXT-15-36697

[63]   Žák, S.: Elastická analýza stability trhliny ve smykových zátěžných módech. Brno: Vysoké učení technické v Brně, Fakulta strojního inženýrství, 2012. 42 p. Supervisor of the bachelor's thesis doc. Ing. Jana Horníková, Ph.D.

[64] Žák, S.: Popis napjatosti a deformace na čele trhlin zatížených ve smykových zátěžných módech. Brno: Vysoké učení technické v Brně, Fakulta strojního inženýrství, 2014. 67 p. Supervisor of the master's thesis doc. Ing. Jana Horníková, Ph.D.

[65] Žák, S., Horníková, J., Šandera, P.: Shear mode stress intensity factors for serrated crack fronts. (2017). doi: 10.4028/www.scientific.net/KEM.754.214

[66] Vojtek, T., Žák, S., Pokluda, J.: Quantitative analysis of intrinsic mode III fatigue thresholds in bcc metals. Int. J. Fatigue. (2018). doi:10.1016/j.ijfatigue.2018.04.022

[67] Pokluda, J., Pippan, R., Vojtek, T., Hohenwarter, A.: Near-threshold behaviour of shear-mode fatigue cracks in metallic materials. Fatigue Fract. Eng. Mater. Struct. 37, 232–254 (2014). doi: 10.1111/ffe.12131

[68] Vojtek, T., Pippan, R., Hohenwarter, A., Pokluda, J.: Prediction of effective mode II fatigue crack growth threshold for metallic materials. Eng. Fract. Mech. 174, 117–126 (2017). doi: 10.1016/j.engfracmech.2016.11.024

[69] Vojtek, T., Hohenwarter, A., Pippan, R., Pokluda, J.: Experimental evidence of a common local mode II growth mechanism of fatigue cracks loaded in modes II, III and II+III in niobium and titanium. Int. J. Fatigue. 92, 470–477 (2016). doi: 10.1016/j.ijfatigue.2016.02.042

[70] Ondráček, E., Vrbka, J., Janíček, P.: Mechanika těles: Pružnost a pevnost II. VUT, Brno (1991). ISBN: 80-214-3260-8

[71] Mathworks Inc.: Matlab Help (R2014b), (2014)

[72] Milella, P.P.: Fatigue and corrosion in metals. (2013). ISBN: 978-88-470-2336-9

[73] Žák, S., Horníková, J., Šandera, P., Vojtek, T., Pokluda, J.: Stress Intensity Factors at In-plane and Out-of-plane Tortuous Crack Fronts under Remote Mode II Loading. Frat. ed Integrità Strutt. accepted (in print), (2018)

[74] Žák, S., Horníková, J., Šandera, P., Vojtek, T., Pokluda, J.: Determination of Local Stress Intensity Factors at Microstructurally Tortuous Crack Fronts under Remote Mode II Loading. Procedia Struct. Integr. 5, (2017). doi: 10.1016/j.prostr.2017.11.086

[75] Zhang, G.P., Wang, Z.G.: Short fatigue crack growth under mixed mode loading in Ni3A1 alloy single crystals. Mater. Sci. Eng. 229, 129–136 (1997). ISBN: 3843531552

[76] Cotterell, B., Rice, J.R.: Slightly curved or kinked cracks. Int. J. Fract. 16, 155-169 (1980). doi: 10.1007/BF00012619

[77]   Vojtek, T., Pokluda, J., Šandera, P., Horníková, J., Hohenwarter, A., Pippan, R.: Analysis of fatigue crack propagation under mixed mode II+III in ARMCO iron. Int. J. Fatigue. 76, 47–52 (2015). doi: 10.1016/j.ijfatigue.2014.09.018

[78]   Vatne, I.R., Stukowski, A., Thaulow, C., Ostby, E., Marian, J.: Three-dimensional crack initiation mechanisms in bcc-Fe under loading modes I, II and III. Mater. Sci. Eng. A. 560, 306–314 (2013). doi: 10.1016/j.msea.2012.09.071

[79]   Riemelmoser, F.O., Gumbsch, P., Pippan, R.: Dislocation Modelling of Fatigue Cracks: An Overview. Mater. Trans. 42, 2–13 (2001).
doi: 10.2320/matertrans.42.2

[80]   Žák, S., Horníková, J.: Effects of Crack-Flanks Roughness in the Vicinity of Crack Front. In: Obrusník, A., Fojtů, M., Pejovič, J., Hudcová, K., and Sieberová, M. (eds.) CEITEC PhD Retreat. p. 127. CEITEC, Valtice (2015)

[81]   Žák, S., Horníková, J., Šandera, P.: Stress intensity factors for rough cracks loaded in mode II. (2017). Solid State Phenomena
doi: 10.4028/www.scientific.net/SSP.258.310

[82]   Ault, S.: How do you Find the Horizontal Asymptotes of a Function, available at: https://magoosh.com/hs/ap-calculus/2017/find-horizontal-asymptotes/

7 Nomenclature

APDL   Ansys parametric design language

BCC   body centered cubic

CT   compact tension

CTOD   crack tip opening displacement

CTS   compact tension shear

FE   finite element

FEM   finite element method

LEFM   linear elastic fracture mechanics

RIS   roughness induced shielding

SEM   scanning electron microscope

SIF   stress intensity factor

VCCT   virtual crack closure technique

A surface area of the crack

$A^{+(-)}$ energy needed to close the crack faces

A_i independent fitting coefficient for i-th loading mode (i = I, II, III)

A_{ie} area of the ie-th element

B specimen thickness

B_i independent fitting coefficient for i-th loading mode (i = I, II, III)

C_i independent fitting coefficient for i-th loading mode (i = I, II, III)

D outer diameter of the specimen

E Young's modulus

E' generalized Young's modulus

E_{shear} shear modulus

F external force loading

G_i crack driving force for i-th loading mode (i = I, II, III)

I interaction integral

J J-integral

K_i stress intensity factor for i-th loading mode (i = I, II, III)

K_i^{aux} auxiliary stress intensity factor for i-th loading mode (i = I, II, III)

$K_{i,\,app}$ applied stress intensity factor for i-th loading mode (i = I, II, III)

$K_{i,n}$ normalized stress intensity factors for i-th loading mode (i = I, II, III)

$\mathbf{L}$ matrix of direction cosines

L_i characteristic dimension of cracked body for i-th loading mode (i = I, II, III)

P work of external forces

Q_i quotient describing the change of mean functional value of crack SIFs for i-th loading mode (i = I, II, III)

$Q_{i,c}$ critical value of coefficient Q_i for i-th loading mode (i = I, II, III)

R_i components of reaction forces (i = x, y, z)

R_L	linear roughness
$R_\mathrm{L,\,Fe}$	real crack front roughness for ARMCO iron
R_max	maximal distance of the crack tip from the center of the cylindrical specimen (zig-zag shape)
R_min	minimal distance of the crack tip from the center of the cylindrical specimen (zig-zag shape)
R_S	surface roughness
S	surface area of the projection of rough crack flanks to x-z plane
S_R	surface area of crack flanks (rough crack)
T	loading torque
T_i	components of the vector of surface forces
$\mathbf{T}_\sigma$	stress tensor
$\mathbf{T}_\sigma^{\ *}$	transformed stress tensor
U	strain energy
W_e	elastic energy
W_p	work of external forces
W_c	energy of the system
Y_i	crack geometry factor for i-th loading mode (i = I, II, III)
a	crack length
a_n	depth of the notch
a_{pc}	pre-crack length
b	CTS specimen gripping holes span (horizontal)
c	CTS specimen gripping holes span (vertical)
d	inner diameter of the specimen
d_g	diameter of the CTS specimen gripping hole
d_m	crack front asperity width
f	auxiliary dimension of CTS gripping holes position
f_ij	correction function for stress field around the crack tip (i, j = x, y, z)
h	CTS specimen height
k_cal	K-calibration function
k_i	local stress intensity factors for i-th loading mode (i = 1, 2, 3)
$k_\mathrm{i}^\mathrm{Cotterell,\ Rice}$	local stress intensity factors by Cotterell and Rice [76] for i-th loading mode (i = 1, 2, 3)
$k_\mathrm{i,\,full}$	local stress intensity factors for i-th loading mode (i = 1, 2, 3) for model with fully modelled crack front roughness
$k_\mathrm{i,n}$	normalized local stress intensity factors for i-th loading mode (i = 1, 2, 3)
$k_\mathrm{i,\,simple}$	local stress intensity factors for i-th loading mode (i = 1, 2, 3) for model with simplified crack front roughness
$k_\mathrm{i}^\mathrm{Zhang,\ Wang}$	local stress intensity factors by Zhang and Wang [75] for i-th loading mode (i = 1, 2, 3)

n	number of modeled teeth
ne	number of integrated elements (numerical integration)
q	crack extension vector
r	distance from the crack tip
r_g	radius of the CTS specimen gripping hole
r_i	crack front roughness parameters for i-th direction (i = x, y, z)
s	length of the integration path
s_r	length of rough portion of the crack
t	thickness of modelled specimen
u_i	components of a vector of relative displacements (i = x, y, z)
u_i^aux	auxiliary components of a vector of relative displacements (i = x, y, z)
u_i^j	crack displacement for j-th loading mode (j = I, II, III) in i-th direction (i = x, y, z)
w	characteristic dimension of the specimen
w_e	strain energy density
w_{iw}	weight function
z_n	normalized thickness coordinate
Γ	integration path
Γ_T	path of the crack front
Δ	deformation of the cracked body
ΔA	crack extension area
Δa	length of tilted part of crack
$\Delta K_\text{i, eff th}$	i-th mode effective threshold stress intensity factor value (i = I, II, III)
$\Delta k_\text{i, eff th}$	local i-th mode effective threshold stress intensity factor value (i = 1, 2, 3)
$\Delta u \; (v, w)$	relative displacement of the crack face in the x, y and z directions respectively
Π	potential energy of the cracked body
α	crack front kink angle
α_m	maximal crack front kink angle
β	crack front twist angle
δ_i	crack faces displacement for i-th loading mode (i = I, II, III)
δ_ij	Kronecker delta
ε_ij	strain tensor components (i, j = x, y, z)
$\varepsilon_\text{ij}^\text{aux}$	auxiliary strain tensor components (i, j = x, y, z)
ϕ	polar coordinate around the cylindrical specimen
κ	Kolosov's constant
μ	Poisson's ratio
ξ	ratio of specimen diameters
ρ	notch root radius
σ_ij	stress tensor components (i, j = x, y, z)

$\sigma_{ij}{}^{aux}$	auxiliary stress tensor components (i, j = x, y, z)
τ_i	relevant shear stress components for i-th loading mode (i = II, III)
φ	angular coordinate around the crack tip
ψ	crack front asperity angle (in-plane roughness)
ω	crack front asperity angle (out-of-plane roughness)

8 Author's outputs and activities related to doctoral studies

Published papers and conference contributions were aimed at the topic of fracture mechanics, especially at the shear modes loading. All publications and outputs presented in this chapter are closely related to the topic of author's dissertation thesis and were published during his Ph.D. studies (journal papers [I] and [II] and a conference contribution [XII] are related to the initial research of the standard fracture mechanics models and were not mentioned in this thesis, however, models of specimens with complicated fracture geometry originated from this research). Moreover, the conference contribution [XIX] was not related to the description of complicated crack fronts, but the research was done during the doctoral studies and it was related to the similar subject – the notch influence on the SIFs. This research is (by the time of competition of this thesis) being summarized in a paper [XI] which will be send for review.

Some conferences contributions listed in this section were not strictly presented by author of this thesis at respective conference, but all of them were part of his research. Author of this thesis presented the results on conferences [XIII, XV, XVII] by himself. Moreover, the contribution for the conference in Verona, Italy [XX] is in preparation (by the time of completion of this thesis) and it will be presented by the author himself.

Other author's activities were closely related to the Ph.D. studies in terms of getting new and different experiences and of course the fulfillment of the study obligations.

8.1 Papers in scientific journals

[I]   Horníková J., Šandera P., Žák S. and Pokluda J.: Specimens for Simultaneous Mode II, III and II+III Fatigue Crack Propagation: Elasto-Plastic Solution of Crack Tip Stress-Strain Field. Advanced Materials Research 891-892 (2014). pp. 1585 – 1590. ISSN: 1022-6680, WOS: 000337767700245

[II]   Žák S., Horníková J., Šandera P. and Pokluda J.: Verification of Linear Dependence of Plastic Zone Size on J-integral for Mixed-mode Loading. Applied Mechanics and Materials 751 (2015). pp. 15 – 20. ISSN: 1660-9336

[III]   Horníková J., Žák S. and Šandera P.: Numerical Fracture Analysis of Compact Tension Shear (CTS) Specimens with Tortuous Crack Fronts. Key Engineering Materials 665 (2016). pp. 77 – 80. ISSN: 1013-9826

[IV]   Žák S., Horníková J. and Šandera P.: Stress Intensity Factors for Rough Cracks Loaded in Mode II. Solid State Phenomena 258 (2017). pp. 310 – 313. ISSN: 1012-0394

[V]   Žák S., Horníková J. and Šandera P.: Shear Mode Stress Intensity Factors
         for Serrated Crack Fronts. Key Engineering Materials 754 (2017).
         pp. 214 - 217. ISSN: 1662-9795

[VI]   Vojtek T., Žák S. and Pokluda J.: On the Connection between Mode II and
         Mode III Effective Thresholds in Metals. Frattura ed Integrità Strutturale 41
         (2017). pp. 245 – 251. ISSN: 1971-8993

[VII]   Žák S., Horníková J., Šandera P., Vojtek T. and Pokluda J.: Determination of
         Local Stress Intensity Factors at Microstructurally Tortuous Crack Fronts
         under Remote Mode II Loading. Procedia Structural Integrity 7 (2017).
         pp. 254 - 261. ISSN: 2452-3216

[VIII]   Žák S., Horníková J., Šandera P., Vojtek T. and Pokluda J.: Stress Intensity
         Factors at In-plane and Out-of-plane Tortuous Crack Fronts under Remote
         Mode II Loading. Frattura ed Integrità Strutturale (2018). accepted (in print).
         ISSN: 1971-8993

[IX]   Horníková J., Šandera P., Žák S. and Pokluda J.: Stress Intensity Factors
         for Cracks Emanating from a Notch under Shear-mode Loading.
         Key Engineering Materials (2018). accepted (in print). ISSN: 1662-9795

[X]   Vojtek T., Žák S. and Pokluda J.: The Quantitative analysis of intrinsic
         mode III fatigue thresholds in bcc metals. International Journal of Fatigue
         (2018). accepted (in print). DOI: 10.1016/j.ijfatigue.2018.04.022

[XI]   Žák S., Šandera P., Horníková J. and Pokluda J.: The critical depth of mode II
         and III cracks emanating from circumferential U-notches in round bars.
         Engineering Fracture Mechanics (2018). in preparation

8.2 Contributions on national and international conferences

[XII]   Žák S., Horníková J., Šandera P. and Pokluda J.: Verification of Linear
         Dependence of Plastic Zone Size on J-integral for Mixed-mode Loading.
         Presented on: *"Applied Mechanics, Materials and Manufacturing"*.
         Krung Thep 2014

[XIII]   Žák S. and Horníková J.: Effects of Crack-Flanks Roughness in the Vicinity of
         Crack Front. In: Obrusník A., Fojtů M., Pejovič J., Hudcová K., Sieberová M.
         (Eds.) *"CEITEC PhD Retreat"*. CEITEC. Valtice 2015. p. 127.
         ISBN: 978-80-210-7825-3

[XIV]   Horníková J., Žák S. and Šandera P.: Numerical Fracture Analysis of Compact
         Tension Shear (CTS) Specimens with Tortuous Crack Fronts.
         In: M. H. Aliabadi (Ed.) *"Fracture and Damage Mechanics 14"*. Budva 2015

[XV]   Žák S., Horníková J. and Šandera P.: Stress Intensity Factors for Rough
         Cracks Loaded in Mode II. In: P. Šandera (Ed.) *"Materials Structure &*
         Micromechanics of Fracture (MSMF8)". Vutium, Brno 2016. p. 218.
         ISBN: 978-80-214-5357-9

[XVI]   Vojtek T., Žák S. and Pokluda J.: On the Connection between Mode II and
         Mode III Effective Thresholds in Metals. In: *"Characterisation of Crack Tip*
         Fields". Bonifacio 2017

[XVII]   Žák S., Horníková J., Šandera P., Vojtek T. and Pokluda J.: Determination of
         Local Stress Intensity Factors at Microstructurally Tortuous Crack Fronts
         under Remote Mode II Loading. In: S. Beretta, G. Nicoletto (Eds.) *"3rd*
         International Symposium on Fatigue Design and Material Defects". Politecnico
         Milano. Lecco 2017. p. 30

[XVIII] Žák S., Horníková J. and Šandera P.: Shear Mode Stress Intensity Factors for
         Serrated Crack Fronts. In: M. H. Aliabadi (Ed.) *"Fracture and Damage*
         Mechanics 16". Florence 2017

[XIX]   Horníková J., Šandera P., Žák S. and Pokluda J.: Stress Intensity Factors for
         Cracks Emanating from a Notch under Shear-mode Loading. In: M. H.
         Aliabadi (Ed.) *"Fracture and Damage Mechanics 17"*. Sevilla 2018

[XX]   Žák S., Horníková J., Šandera P., Vojtek T. and Pokluda J.: Stress Intensity
         Factors at In-plane and Out-of-plane Tortuous Crack Fronts under Remote
         Mode II Loading. In: *"Crack Paths"*. Verona 2018

8.3 Other

Author of this thesis during his internship at the Fraunhofer Institute in Dresden, Germany (from beginning of October 2015 to the end of November 2015 and from the October 2016 to the end of January 2017) wrote several technical reports about the simulation and research on SRAM cell behavior under thermally induced deformation. Outputs of the research at the Fraunhofer Institute were also author's contribution on the final presentation of results to industrial partners.

Results from research which was done during the internships are also planned to be published in some kind of scientific journal alongside the experimental results obtained by Fraunhofer Institute researchers. However, many of the results of this research are considered "top-secret" (according to legal terms of the Institute) and cannot be further discussed.

Other, similar research at the Fraunhofer Institute was done by the author during his part-time job at the institute (until the end of June 2018) in the frame of project between Fraunhofer IKTS and TESCAN. However, this research was done for the industrial partners of the Fraunhofer Institute and thus there is no chance for any publication (since the research was again deemed to be "top-secret").

Beside the publication and research activities, author of this thesis also got many experiences from the university environment by the means of teaching activities – regular teaching of the course 4PP – Strength of Materials at the Faculty of Mechanical Engineering (Brno University of Technology), by tutoring the students at mentioned faculty and by organizing the international conference Materials Structure & Micromechanics of Fracture (MSMF8) in 2016.